Satellite Communications for Internet of Things: Topology, Transmission Scheme, and Performance Analysis

A thesis submitted in partial fulfilment
of the requirements for the degree of

Doctor of Philosophy
in
Electronics and Communication Engineering

by

Ayush Kumar Dwivedi
2018802002
ayush.dwivedi@research.iiit.ac.in

Advisor: Dr. Sachin Chaudhari

International Institute of Information Technology Hyderabad
500 032, India

July 2024

International Institute of Information Technology Hyderabad
Hyderabad, India

CERTIFICATE

This is to certify that work presented in this thesis proposal titled ***Satellite Communications for Internet of Things: Topology, Transmission Scheme, and Performance Analysis*** by Ayush Kumar Dwivedi has been carried out under my supervision and is not submitted elsewhere for a degree.

_____ _____

Date Advisor: Dr. Sachin Chaudhari

saṃgacchadhwaṃ saṃvadadhwaṃ saṃ vo manāṃsi jānatām |
devā bhāgaṃ yathā pūrve sañjānānā upāsate ||
[Rig Veda 10.191.2]

May we all move together in harmony, speak together in one voice; may our minds be one (in agreement); just as the ancient gods cultivated this conduct and thus are worshipped.

Acknowledgements

My heart is filled with emotions as I pen down this last piece of text in my PhD thesis. I embarked on this journey at a time when all seemed over for me personally. I knew my heart would ache forever when my mother left for the holy abode, showering her choicest of the blessings which brought me to IIIT-H. My life is the epitome of her teachings and a reflection of her blessings. I feel satisfied to have fulfilled her dreams with this PhD thesis. The work leading to this thesis has been carried out under the able guidance of Prof. Sachin Chaudhari at the Signal Processing and Communications Research Center (SPCRC), IIIT Hyderabad. I am indebted to a long list of teachers, friends, and peers from whom I have learned. So, please bear with me if this is a bit long.

I am expressing my sincere gratitude to my advisor, Prof. Sachin Chaudhari, without whom this thesis would not have been possible. I have no words to describe the freedom he provided and the accessibility he maintained for me. I also want to thank him for building an environment of unwavering trust and mutual respect, turning him into my guardian. The knowledge and skills he imparted to me will profoundly impact my professional development as a researcher beyond my PhD journey and shape me as a person. I treasure our discussions, technical and non-technical alike. His role was like a lighthouse guiding a novice sailor.

I also want to express my gratitude to Dr Neeraj Varshney from the National Institute of Standards and Technology, who has immensely helped me with the technical analysis in the manuscripts that I co-authored with him. I am also grateful to Prof. Pramod Varshney from Syracuse University, Prof. Symeon Chatzinotas and Dr. Houcine Chougrani from the University of Luxembourg. They have contributed to this thesis with their insightful feedback and guidance in our co-authored publications.

I am grateful to my advisor and Prof. Kavita Vemuri for involving me in a lot of other ongoing projects, which resulted in multiple publications not directly included in this thesis. I am fortunate to have co-authored papers with so many talented researchers, especially Rajashekhar, Nikhil, Ayu, Souradeep, Spanddhana, Ishan, Ayush Lall, Nilesh, Nitin, Rishikesh, Harsha, and Bhumika. Working on these projects has provided invaluable breadth to my technical knowledge.

I want to acknowledge the National Geospatial Programme (NGP), Department of Science and Technology, Government of India, for their generous fellowship under grant no. 2073 (2020) and the Pernod Ricard India Foundation (PRIF) Social Incubator Program 2019, which financially supported my research work. I would also like to acknowledge the financial support received from the Smart City Research Center, IIIT-H.

Next, I also want to express my immense gratitude to Prof. Jayanthi Sivaswamy, head of SPCRC, for all her support and encouragement throughout my PhD journey. I also acknowledge insightful discussions with other faculty members at SPCRC, especially Prof. Prasad Krishnan, Prof. Lalitha Vadlamani, Prof. Santosh Nannuru, and Prof. Praful Mankar. I am also grateful to Prof. Syed Maqbool Ahmed, from the University of Hyderabad, who sowed the seed of research and motivated me to pursue PhD through his inspiring lectures. Due to my involvement in deployment-related activities, I have been blessed to have interacted with numerous staff members of IIIT-H. I want to thank the entire IIIT-H family, including the general administration team, finance team, IT/engineering team, hostel and mess administration staff, and security personnel, for the priority support you always provided.

My heartfelt thanks to all my SPCRC colleagues and friends, especially my *Chai-pe-charcha* (discussion over tea) partners, Ruchi and Kali. The countless hours of research discussions, joyful meals and eternal ranting together are etched in my memory forever. These memories would become even more priceless as I and Ruchi move forward to tie knots for a lifelong association. Sincere gratitude is extended to all my current and former colleagues, especially Madhuri, Shiva, Zakir, Anish, Praneeth, Minaxi, Ruchi Chauhan, Sudeepini, Ihita, Shreyas, and Viswanadh. I am fortunate to have worked and interacted with all of you. I convey my best wishes to newly joined researchers, including Naganjani, Chandan, Deepthi, Om, Ritik, Shreyas, Nagesh, and Ankit, for having an enriching journey. I also want to thank Mrs Sheeba Chaudhari and the blessed child, Yajat Chaudhari, for all the love and care. The delicious meals that Sheeba maam served and my interactions with Yajat made IIIT-H feel like a second home.

Last and foremost, I want to express my deepest gratitude to my family, especially my father, Mr Praveen Kumar Dwivedi, and my mother, Late Mrs Asha Dwivedi, my elder brother, Mr Piyush Dwivedi and my sister-in-law, Mrs Parul Dwivedi. You are the meaning behind my achievements in life. I derive all my strength and abilities from the enormous love, care, and support you shower on me. I am and will forever remain committed to your happiness and well-being.

I am a staunch believer that people and places become part of us. As I move on to the next phase of my life, I am carrying all the learnings and experiences not only in the form of this thesis but predominantly in the form of the person I have transformed into.

Ayush Kumar Dwivedi

Abstract

The proliferation of the Internet of Things (IoT) has revolutionised numerous aspects of daily life, ranging from personal home automation to the development of smart cities. However, the deployment of IoT devices is often limited to areas with available terrestrial infrastructure, leaving many locations without seamless connectivity. The emergence of mega-low Earth orbit (LEO) satellite constellations presents an opportunity to extend IoT deployments to previously uncovered areas, ensuring ubiquitous coverage. From a communication perspective, IoT networks have specific challenges, such as the availability of limited transmit power and computational resources. These challenges are further exacerbated in satellite scenarios due to higher path loss, constrained link budget and interference from large deployments. The aim of this thesis is to address these challenges by proposing network topology and transmission schemes specifically designed for LEO satellite-based IoT networks.

A star-of-star topology is proposed with a physical (PHY) layer combining that capitalises on the diversity advantages of numerous visible LEO satellites. It results in an improved link budget and enhanced coverage probability. Initially, a simple system model is assumed for analysing the outage probability (OP) without considering orbital dynamics and interference from other users. The OP of two combining schemes, selection combining (SC) and maximal ratio combining (MRC), is derived in closed form. It is also compared with a single satellite scenario to demonstrate the benefits of using multiple satellites. The diversity order analysis proves that the topology achieves a diversity order equal to the number of satellites involved in combining. The MRC scheme achieves higher coding gain and, thus, better OP performance than the SC scheme.

Later, the performance analysis is extended for a more practical system model incorporating non-idealities in terms of interference and imperfect channel state information (CSI). Tools from stochastic geometry are also employed to model the satellite locations for computing the statistics of slant range and number of visible satellites in closed form. Considering interference, the OP is derived for two decoding schemes at the ground station (GS): The capture model (CM) and the successive-interference-cancellation (SIC). Simplified expressions for the OP under a high signal-to-noise ratio (SNR) assumption are also derived, which are further utilized to optimise the system parameters for achieving a target OP. The derived analytical results have been rigorously validated using Monte Carlo simulations. The results demonstrate that for the practical values of the system parameters like transmit power and number of visible satellites, the proposed topology is feasible and attractive for low-powered IoT networks.

Finally, on the medium access control (MAC) layer, a transmission scheme based on change detection is proposed to accommodate more users within the network and improve energy efficiency.

Machine learning (ML) algorithms are also proposed to reduce the payload size by leveraging the correlation among the sensed parameters. Real-world data from an IoT testbed deployed for a smart city application is utilised for the performance analysis of the proposed scheme. The findings reveal that the traffic pattern, post-implementation of the proposed scheme, differs from the commonly assumed Poisson traffic, thus proving the effectiveness of having IoT data from actual deployment. It is demonstrated how the transmission scheme facilitates accommodating more devices while targeting a specific collision probability. Considering the limited visibility of LEO satellites, the effective data received at the server is evaluated for the satellite's link budget and visibility duration. The average battery lifetimes are also demonstrated to increase by many folds using the proposed transmission schemes and ML algorithms.

Contents

List of Figures

List of Tables

Abbreviations

3GPP	3rd generation partnership project
ACRDA	asynchronous contention resolution diversity ALOHA
AF	amplify-and-forward
AQI	air quality index
AWGN	additive white Gaussian noise
BPP	binomial point process
BW	bandwidth
CDF	cumulative distribution function
CM	capture model
CPCB	Central Pollution Control Board
CRDSA	contention resolution diversity ALOHA
CSI	channel state information
CSS	chirp spread spectrum
DF	decode-and-forward
DL	downlink
DPSK	differential binary phase shift keying
DtS-IoT	direct-to-satellite IoT
E-SSA	enhance spread-spectrum ALOHA
EIRP	equivalent isotropically radiated power
eMBB	enhanced mobile broadband
eMTC	enhanced machine type communication
FDMA	frequency division multiple access
G/T	antenna gain-to-noise-temperature
GA	Genetic algorithm
GEO	geostationary Earth orbit
GFSK	Gaussian frequency shift keying
GS	ground station
GSO	geostationary orbit
GW	gateway

HTS	high throughput satellite
IaaS	infrastructure as a service
IoT	Internet of Things
ISRO	Indian Space Research Organization
LEO	low Earth orbit
LoRaWAN	long range wide area network
LoS	line-of-sight
LPWAN	low power wide area networks
LTE	long-term evolution
MAC	medium access control
MEO	medium earth orbit
MGF	moment generating function
ML	machine learning
MRC	maximal ratio combining
NB-IoT	narrowband-IoT
NGSO	non-Geostationary orbit
NOMA	non-orthogonal multiple access
NPRACH	narrowband physical uplink shared channel
NTN	non terrestrial network
OFDMA	orthogonal frequency division multiple access
OP	outage probability
PaaS	platform as a service
PDF	probability density function
PHY	physical
PLR	Packet Loss Ratio
PM	particulate matter
PPP	Poisson point process
PRB	physical resource block
QoS	quality of service
RAO	random access opportunities
RF	random forest
RFTDMA	random frequency and time division multiple access
RMSE	root mean squared error
RTT	rount trip time
SaaS	software as a service
SC	selection combining
SF	spreading factor

SIC	successive interference cancellation
SINR	signal-to-interference-plus-noise ratio
SNR	signal-to-noise ratio
SR	shadowed-Rician
SS	single satellite
TDMA	time division multiple access
UL	uplink
UNB	ultra-narrowband

Symbols

α	path loss exponent
B	available bandwidth
β_{AF}	AF gain factor
d	altitude of satellite
$\mathbb{E}[\cdot]$	expectation measure
$f_X(x)$	PDF of random variable X at point x
$F_X(x)$	CDF of random variable X at point x
$\Gamma(\cdot)$	Gamma function
γ_u	end-to-end SINR of the u^{th} user
γ_{us}	end-to-end SINR between u^{th} user and s^{th} satellite
γ_{th}	SINR threshold
g_s	channel coefficient of s^{th} satellite in downlink
$\mathcal{G}_s$	transmit antenna gain at the satellite
$\mathcal{G}_{\text{GS}(\varphi_s)}$	receive antenna gain at the GS
$\mathcal{G}_s(\varphi_{us})$	receive antenna gain at the satellite
$\mathcal{G}_u$	transmit antenna gain at the user
h_{us}	channel coefficient for $(u-s)$ user-satellite pair in uplink
k_B	Boltzmann's constant
K	number of satellites in constellation
$K_v(\cdot)$	v^{th} order modified Bessel function of second kind
K_{vis}	number of visible satellites
λ	wavelength
$\mathcal{L}\{\cdot\}$	Laplace transform operator
m_{RAO}	number of sub-carriers per RAO
$M_X(t)$	MGF of random variable X at point t
(m, b, Ω)	parameters of shadowed-Rician channel
ω_s	angular velocity of the satellite
ω_e	angular velocity of the Earth's rotation
$\mathbb{P}$	probability measure

$\mathcal{P}$	success probability of binomial random variable K_{vis}
φ_s	angle between s^{th} satellite location and beam center *w.r.t* GS
φ_{us}	angle between u^{th} user location and beam center *w.r.t* satellite
P_{out}	outage probability
P_s	transmit power of the s^{th} satellite
P_u	transmit power of the u^{th} user
$\mathcal{R}$	target rate
r_e	radius of Earth (6371 km)
r_{max}	maximum distance between a user and a satellite
R_g	distance between any satellite and GS
R_{us}	distance between the u^{th} user and s^{th} satellite
$\Re\{\cdot\}$	real part of a complex number
S	number of satellites used for AF
σ_n^2	AWGN power at the satellite for u^{th} user
σ_w^2	AWGN power at he GS for s^{th} satellite
u	number of IoT users
θ_0	minimum elevation angle or mask angle
θ_e	elevation angle
$W_{\mu,v}(\cdot)$	Whittaker function
ξ	power of the residual error in SIC
y_s	received signal at the s^{th} satellite
z_s	received signal at the GS from s^{th} satellite

List of Related Publications

[P1] Ayush Kumar Dwivedi, Sai Praneeth Chokkarapu, Sachin Chaudhari and Neeraj Varshney, **"Performance Analysis of Novel Direct Access Schemes for LEO Satellites Based IoT Network"**, in proceedings of *IEEE International Symposium on Personal, Indoor and Mobile Radio Communications (PIMRC)*, 2020.

[P2] Ayush Kumar Dwivedi, Sachin Chaudhari, Neeraj Varshney and Pramod K. Varshney, **"Performance Analysis of LEO Satellite-Based IoT Networks in the Presence of Interference"**, in *IEEE Internet of Things Journal*, 2023.

[P3] Ayush Kumar Dwivedi, Houcine Chougrani, Sachin Chaudhari, Neeraj Varshney and Symeon Chatzinotas, **"Efficient Access Scheme for LEO Satellite-Based NB-IoT: A Data-Driven Perspective"**, under review at *IEEE Transactions on Aerospace and Electronic Systems*, 2024 (available online: *arXiv:2406.14107*).

Related co-author publications:

[P4] S. Kota, Ayush Kumar Dwivedi, Sachin Chaudhari, Neeraj Varshney, et al., **"Reference Architecture and Use Cases for LEO Satellite-Based IoT Networks in International Network Generations Roadmap: Satellite"**, in proceedings of *IEEE Future Networks World Forum (FNWF)*, 2022.

[P5] Nikhil Lamba, Ayush Kumar Dwivedi and Sachin Chaudhari, **"Performance Analysis of Selective Decode-and-Forward Relaying for Satellite-IoT"**, in proceedings of *IEEE Globecom Workshops*, 2022.

[P6] Ayu Parmar, Spanddhana Sara, Ayush Kumar Dwivedi, et.al., **"Development of End-to-End Low-Cost IoT System for Densely Deployed PM Monitoring Network: An Indian Case Study"**, at Frontiers in the Internet of Things, 2024.

[P7] C. Rajashekar Reddy, T. Mukku, A. Dwivedi, A. Rout, S. Chaudhari, K. Vemuri, K. S. Rajan, A. M. Hussain, **"Improving Spatio-Temporal Understanding of Particulate Matter using Low-Cost IoT Sensors"**, in proceedings of *IEEE International Symposium on Personal, Indoor and Mobile Radio Communications (PIMRC)*, 2020.

Co-authored publications not directly related to this thesis but have contributed immensely to understanding the practical aspects of IoT networks:

- Bhumika Sahu, Ayush Kumar Dwivedi, Sachin Chaudhari, and Kavita Vemuri, **"Assessing the Impact of Air Pollution on Physiology: Implications and Prospects"**, in proceedings of *IEEE INDICON*, 2023.
- Rishikesh Bose, Shreyash Gujar, Ayush Kumar Dwivedi, Kavita Vemuri, and Sachin Chaudhari, **"Comparative Analysis of Construction-Related Air Pollution in Indoor and Outdoor Environment"**, in proceedings of *International Conference on Environment Pollution and Prevention (ICEPP)*, 2023.
- Souradeep Deb, Ayush Dwivedi, Sachin Chaudhari, K.S. Rajan, **"Spatial factor analysis of mobile IoT data: A case study on PM across India"**, in proceedings of *IEEE International Geoscience and Remote Sensing Symposium (IGARSS)*, Malaysia, 2022.
- A. Kumar Lall, A. Khandelwal, R. Bose, N. Bawankar, N. Nilesh, A. Dwivedi, S. Chaudhari, **"Making Analog Water Meter Smart using ML and IoT-based Low-Cost Retrofitting"**, in proceedings of *International Conference on Future Internet of Things and Cloud (FiCloud)*, Rome, 2021.

List of patents applied for the development of IoT devices:

- C. Rajashekar Reddy, Sachin Chaudhari, Ayu Parmar, Ayush Kumar Dwivedi, Niranjan Keesara, Mahesh Murty, "Air quality monitoring device with less energy consumption", India Patent Application Number 202141021963, May 2021.
- Ayush Lall, Nitin Nilesh, Ansh Khandelwal, Rhishi Bose, Nilesh Bawankar, Ayush Dwivedi, Sachin Chaudhri, "System and method for digitizing a reading in an analog water meter using machine learning", India Patent Application Number 202141021341, May 2021.

Chapter 1

Introduction

1.1 Motivation

The **IoT** is a transformative technology that involves *connecting everyday objects, devices, and machines to the internet, allowing them to communicate and share data*. With data-driven insights and automation, IoT is changing how we interact with our surroundings. The emerging IoT networks aim to connect a large number of devices and sensors having diverse quality of service requirements to the internet. It is envisioned that these IoT networks will have any time, anywhere, and any device connectivity, spanning over large application scenarios like smart city, smart grid, industrial automation, e-healthcare, connected vehicles and marine vessel tracking. This vision will provide some of the most significant challenges to the existing state-of-the-art. For example, the expectation to connect billions of things with improved battery life and ubiquitous access is a significant challenge. Although terrestrial wireless systems have seen significant enhancements in capacity, coverage at remote locations is still a challenge. Estimates suggest that terrestrial cell towers connect only 25% of the world's landmass, and when including the oceans, only 10% of the Earth's surface has terrestrial connectivity [1].

Satellites are expected to play a role in overcoming the challenge of limited coverage. The *intrinsic broadcasting capability of satellite systems makes them a viable solution for delivering truly ubiquitous service to IoT networks* often deployed remotely over large areas [2]. This quality positions them as an attractive solution for diverse global applications and services, either as standalone systems or integrated satellite-terrestrial networks. The focus on satellite communications has intensified, especially as network operators incorporate satellites into backhauling infrastructures to connect and integrate 5G systems [3]. Amidst these developments, non-Geostationary orbit (NGSO) satellites emerge as key players. The NGSO systems, including CubeSats and low Earth orbit (LEO) satellites, orbit at lower altitudes than conventional geostationary Earth orbit (GEO) satellites. This characteristic results in lower propagation delays, smaller sizes, and reduced signal losses, presenting advantages over geostationary orbit (GSO) satellites. Moreover, recent advancements in the field of high throughput satellite (HTS) enable narrow steerable beams in NGSO constellations, allowing the use of smaller and cost-effective equipment at user terminals [4], as is the case in IoT. Recently, several dense LEO satellite constellations, like Starlink, Amazon Kuiper, OneWeb, Lynk, and Telesat, have emerged. These constellations

can potentially serve the remotely deployed IoT networks with multiple satellites in the visible range for a large fraction of the Earth's surface [5]. Many CubeSats, a class of nanosatellites with a standard size measured in multiples of 10 centimetres, are also becoming increasingly famous for IoT. For example, Astrocast, Lacuna Space, Myriota, Sateliot, Swarm Technologies, TelNet Space, etc., are building solutions for CubeSat-based IoT networks. A recent 3rd generation partnership project (3GPP) Rel-17 work item has also specified the support required for satellite-based narrowband-IoT (NB-IoT)/enhanced machine type communication (eMTC) networks [6].

A critical aspect to consider while discussing the role of satellites for IoT applications is that these are sensing heavy. Offloading the sensed information to a data centre is a major task. For example, use cases like weather monitoring or air pollution monitoring involve sending status data at regular or random intervals. IoT devices in such applications hardly generate a few kilobytes of data and operate at low power levels with constrained computational resources. Recently, many low power wide area networks (LPWAN) have been developed to cater to the low-data, low-power requirements of IoT, which use terrestrial gateways as a bridge between the end devices and the central data server to offload sensed information. *This thesis is motivated by such architectures where the author envisions using the LEO satellite as a transparent or regenerative bridge between the IoT devices and the central data server. The analytical derivations and system-level simulations presented in this thesis demonstrate that for the practical values of the system parameters like transmit power, battery capacity, number of devices and visible satellites, the contributions are feasible and attractive choices for LEO satellite-based IoT networks.*

1.2 Objective and scope of the thesis

The broad *scope of this thesis is on the physical (PHY) and medium access control (MAC) layer aspects of satellite-based IoT networks* with a particular focus on topology design, transmission schemes and performance analysis. IoT networks benefit from enhanced coverage by using satellites. Still, they suffer from the challenge of large path losses due to long distances between IoT devices and satellites and interference from other devices in case of massive deployments. The previous surveys in [7–9] have identified several architectural challenges and enabling solutions for satellite-IoT networks. It is recommended that perhaps upgrades can be made at the PHY and MAC layers to explore novel topologies and computationally simple access schemes for massive IoT connectivity. The main research questions identified based on a comprehensive literature review are as follows:

- Can IoT networks be supported by LEO satellite-based access networks? What is the suitable architecture/topology and the required link budget?

- What will be the performance in terms of coverage or capacity, and how do the nonidealities like interference and imperfect channel estimates affect it?

- How to increase the capacity within the limited visibility duration provided by LEO satellites for supporting densely populated IoT networks?

The **first objective** of this thesis is to address questions on the PHY layer aspects by *proposing a simple and efficient topology for satellite-IoT networks*. The longer distances between IoT users and satellites lead to higher path losses. Also, enhanced coverage enables multiple IoT users to transmit simultaneously, leading to interference. To address the above factors, the proposed topology should involve multiple satellites for leveraging spatial diversity. This diversity can help improve signal quality and provide resilience to outages at the ground station (GS). In the past, many topologies used in terrestrial LPWAN technologies have been analysed [10, 11]. However, their performance has not been explored for satellite-based IoT networks, as done in this thesis. Another aspect to consider is that IoT devices only require intermittent coverage for data offloading. This is unlike cellular networks, where significant energy is consumed in an idle state as well for listening and synchronising with the base station. The proposed topology should facilitate a burst mode of operation that allows IoT devices to transmit data at specific intervals when the satellites are visible and sleep after that. This ensures minimal computational complexity for IoT users, and all the processing is shifted to the GS.

The Publication [P1] is dedicated to this first objective, proposing a star-of-star topology with the satellites as a transparent repeater and combining at the PHY layer. The co-authored Publications [P4] and [P5] are also aligned towards the same objective where various use case scenarios and satellites with regenerative payloads are explored, respectively. This objective lays the foundation for performance evaluation, implementation considerations, and further optimisations of the proposed topology.

The **second objective** of this thesis on the PHY layer aspects is to *analyse the coverage performance of the proposed topology for a practical scenario considering nonidealities*. Unlike previous studies [12–14], where either uplink or downlink performance is analysed for simple channel models, this thesis aims to investigate the coverage performance using more realistic channel fading models for satellite communication. Another associated objective is to analyse the performance of various combining schemes and decoding schemes in the presence of interference. Additionally, motivation has been drawn from [15, 16] to employ stochastic geometry in modelling the satellites' locations in the proposed topology. This ensures that the explicit orbital simulations and the precise ephemeris of the LEO constellation are not required, and the inferences can be generalised for any constellation.

The Publications [P1] and [P2] are dedicated to this objective. In Publication [P1], the combining schemes are initially analysed in an ideal scenario with no interference. Publication [P2] incorporates practical assumptions on orbital dynamics and nonidealities like interference and imperfect channel knowledge. Multiple decoding schemes at the GS are also analysed in this regard. Incorporating practical assumptions such as orbital dynamics, interference, and imperfect channel knowledge in Publication [P2] enhances the realism of the analysis. These factors are crucial for understanding system performance in real-world deployment scenarios.

The **third objective** of this thesis is to address questions on the MAC layer aspects by *proposing intelligent transmission and scheduling algorithms to enhance capacity and energy efficiency* of the

proposed topology. In this thesis, capacity is referred to in terms of the number of users supported, and the energy efficiency of the devices is referred to in terms of battery life. LEO satellites have limited visibility duration and constrained link budget. The aim of this thesis is to employ change detection and machine learning (ML)-based transmission reduction schemes on a real IoT traffic dataset and demonstrate how these schemes benefit in a LEO satellite scenario.

The Publication [P3] is dedicated towards this objective. A Shewhart-based transmission scheme is employed for intelligence scheduling to enhance capacity, and ML algorithms are proposed for reducing packet size to improve battery life. A system-level analysis of the proposed transmission scheme is performed on a dataset collected as part of Publications [P6] and P[7]. By applying these advanced methods to real IoT traffic datasets, the thesis aims to demonstrate the effectiveness of these algorithms in the context of satellite IoT.

1.3 Contributions

This subsection presents the technical contributions of the author as part of this thesis. The performance of all the proposed schemes is studied using analytical methods and corroborated extensively using MATLAB simulations.

The contributions that align with the first objective of proposing a **topology for satellite-IoT** are listed as follows:

- **Star-of-star topology for IoT networks using multiple LEO satellites** as a gateway is proposed in Publication [P1] and [P2]. The proposed topology enables IoT devices to wake up and broadcast the sensed data to all the visible satellites without any prior coordination and sleep again. The satellites act as transparent or regenerative relays to offload the received signal to the GS. The GS coherently combines the signals from multiple satellites using various combining techniques, thus providing spatial diversity. The proposed topology can effectively leverage the benefits of multiple satellites to achieve the desired performance and enable burst transmissions without coordination among users, making it an attractive choice for satellite-based IoT networks.

The contributions that align with the second objective of **analysing coverage performance** are listed as follows:

- **Outage probability analysis** is done for the proposed topology under various configurations. Initially, in Publication [P1], the performance of selection combining (SC) and maximal ratio combining (MRC) schemes at the GS is analysed for a simpler system model with satellite acting as a transparent repeater and no interference appearing from other users. In this analysis, the MRC achieves lower outage probability (OP) due to its higher combining gain. Later, in Publication [P2], this analysis is extended to scenarios having multiple interfering devices and imperfect knowledge of channel state information (CSI). For this analysis, stochastic geometry is employed to model satellites' locations as random, making the analysis independent of any

specific realisation of the constellation. Furthermore, the performance of successive interference cancellation (SIC) and capture model (CM)-based decoding schemes at the GS are analysed to mitigate interference.

- **Asymptotic analysis and optimization** is performed in Publication [P2] to derive simplified expressions for the OP under high signal-to-noise ratio (SNR) assumption for both CM and SIC-based decoding schems. These expressions provide insights into the topology's diversity order and coding gain. The proposed topology is demonstrated to achieve a diversity order equal to the number of satellites used for relaying in case of no-interference and perfect CSI. However, the OP attains a floor when there is interference and errors due to imperfect CSI. The asymptotic expressions are further utilized to optimize the system parameters like the number of devices, satellites, and mask angle to obtain the optimal region of operation achieving a target OP.

The contributions that align with the third objective of proposing **efficient transmission schemes** are listed as follows:

- **Shewhart and ML-based transmission reduction** is proposed for a LEO satellite scenario in Publication [P3]. Shewhart helps in accommodating more users within the network by reducing the number of simultaneous transmissions. ML algorithms are also proposed to reduce the payload size by leveraging the correlation among the sensed parameters. Real-world data from an IoT testbed developed as part of Publications [P6] and [P7] for air pollution monitoring is utilised for the performance analysis of the proposed scheme. The findings reveal that the traffic pattern, post-implementation of the Shewhart scheme, differs from the commonly assumed Poisson traffic, thus proving the effectiveness of having IoT data from actual deployment. It is demonstrated that the network's capacity increases significantly to handle a larger user base for a target collision probability. Effectively, higher data is offloaded to the server within the limited visibility duration and the constrained link budget of the system. The average battery lifetimes are also shown to increase by many folds using the proposed transmission schemes and ML algorithms.

For this thesis, the author was responsible for developing the ideas, identifying the appropriate tools, carrying out the mathematical derivations, verifying them with rigorous simulations and writing the manuscripts. Prof. Sachin Chaudhari contributed by conceptualizing the ideas of using the star-of-star topology and Shewhart-based transmission scheme for LEO satellites. He has also contributed to all the publications by reviewing the technical results and providing feedback on the manuscripts. The co-authors guided the research by proposing performance metrics and helped write the publications. Their insightful feedback and guidance greatly contributed to articulating the system model and the work's key contributions.

1.4 Structure of the thesis

The thesis is structured into the following chapters to understand the topics comprehensively. The beginning of every chapter is presented with a brief overview of the chapter for easy reference of the reader.

Chapter 2 presents an overview of IoT networks and satellite communication. It introduces IoT, its key components, various technical requirements, and communication technologies. Additionally, it covers the fundamental role of satellites and common architectures used in satellite communication. Further, use cases and various MAC schemes for satellite-IoT are discussed. The chapter concludes by discussing the link budget and a quick glimpse of recent advancements on the research and standardization fronts.

Chapter 3 focuses on the system model with the proposed direct access topology for satellite-IoT. This chapter delves into the details of the topology, providing a thorough description. Towards the end, a preliminary performance analysis is presented based on a simplified system model, and the corresponding results are discussed. This chapter lays the foundation for the more detailed performance analysis presented in subsequent chapters.

In **Chapter 4**, a comprehensive performance analysis is conducted for a generalized system model built upon the previous chapter. Stochastic geometry tools are employed to model satellite locations, and the impact of imperfect knowledge of the channel is considered. Additionally, this chapter includes a literature survey on various performance analyses conducted for relay-based networks, both with and without satellites.

Chapter 5 discusses the idea of a Shewhart-based transmission reduction to optimize scheduling to accommodate more users within the network and improve energy efficiency. Additionally, ML algorithms have been proposed to reduce payload by eliminating the need to transmit parameters with strong correlation.

Finally, **Chapter 6** concludes this thesis by summarizing the results obtained thus far. It provides an overview of the work conducted and presents ideas for the future.

Chapter 2

Overview of IoT networks and Satellite Communication

This chapter comprehensively overviews satellite-based IoT networks. It begins by discussing the fundamentals of IoT, highlighting its key components and communication technologies. Additionally, the chapter examines the diverse requirements of IoT networks, considering factors such as energy efficiency and access techniques. Furthermore, it covers the satellites' essential role in facilitating IoT connectivity. The chapter then delves into the network architectures used in satellite communications, covering the key concepts of transparent and regenerative configurations of satellite payloads and discussing their significance in the context of IoT networks. It also investigates real-world satellite use cases and associated frequency bands for IoT applications, showcasing their potential and benefits. The reference parameters and link budget analysis for direct access satellite-IoT networks are also presented in this chapter. This chapter also presents various reference scenarios, mapping the topologies to specific use cases to demonstrate their practical applicability. To provide a comprehensive understanding of the subject, the chapter concludes with a note on the recent advancements in satellite-based IoT technology, shedding light on emerging trends and innovative solutions. By encompassing these topics, this chapter aims to establish a strong foundation for the subsequent discussions on satellite-based IoT networks and their performance analysis. Readers interested in a deeper understanding of IoT networks and satellite systems can refer to the following standard textbooks and survey papers: IoT from [17–19], satellite communication from [20–24], LPWAN communication from [25, 26] and Satellite-IoT from [2, 7, 8] and [23, Ch. 12].

2.1 Internet of Things (IoT)

In the past few years, IoT has transformed how humans interact with the physical world. The ability to connect day-to-day objects to the internet has resulted in many smart applications. IoT extends the idea of internet connectivity beyond conventional computer systems to physical objects like cars, lights, speakers, fans, shoes, thermostats, etc. IoT refers to the network of physical objects which possess an IP address for communication with the internet. These physical objects can be anything an IoT engineer can think of. But, the concept of IoT raises a fundamental question: why connect everyday objects to the internet? The answer lies in the transformative potential of this connectivity. Consider the case of

a basic speaker with a microphone – a mere audio device. When linked to the internet, it evolves into a smart device akin to *Amazon Echo* or *Google Nest*. Integration with AI assistants like *Amazon Alexa* empowers it to execute diverse tasks, from online shopping and home electronics control to responding to messages. This simple connection sets the stage for the creation of a smart home. The enormous amount of data aggregated from all such objects helps humans make better and more timely decisions.

Although explained with an example of smart home automation, the use cases of IoT are far-reaching, spanning various verticles like smart cities, healthcare, transportation, agriculture, manufacturing, and more. The following are some of the emerging areas of IoT applications, where the list is only representative and not exhaustive.

- **Smart cities - enhancing urban living [27, 28]:** This involves integrating sensors, networks, and data analytics to improve overall livability in a city. IoT can be utilised across different verticals in a smart city like weather, energy, transportation, infrastructure, health, homes, industry, etc. For example, traffic management can utilise intelligent camera systems to optimise traffic flow through real-time monitoring, reducing congestion. Energy management solutions can employ sensors to control lighting, air conditioning, etc, to save energy. IoT-enabled air quality monitoring systems can provide crucial real-time information for source identification and reporting [29–33]. Additionally, smart water management can harness IoT for real-time monitoring and distribution of water resources, leading to efficient and sustainable water usage [34, 35].

- **Healthcare - transforming medical services [36, 37]:** Physiological parameters like body temperature, heart rate, oxygen saturation, blood pressure, etc, can be tracked on a real-time basis for early warning of any disease or health condition. IoT can be employed for medical device monitoring, enabling remote oversight and management of critical devices like ventilators and ECG machines, etc. Remote or robotic surgeries are another use case of IoT where the surgery can be performed by robotic arms controlled by doctors from a control station, often resulting in more precise handling than a human hand. IoT can also be leveraged at smart hospitals to improve operational efficiency, reduce wait times, and elevate patient care with innovations such as smart beds and connected medical devices.

- **Remote labs - revolutionizing education [38, 39]:** IoT can be used to provide researchers and students with the flexibility to conduct experiments and interact with equipment remotely. This is different from the popularly known concept of Virtual Labs since it provides access to actual physical hardware or equipment and not a virtual replica of it. These labs, equipped with sensors, cameras, and other IoT devices, offer users the ability to monitor and control experiments from a distance. For instance, sensors track and control equipment, while cameras capture real-time images and videos, all accessible through a web-based interface. This approach is particularly beneficial for educational institutions facing resource limitations, offering an alternative to traditional lab spaces and expensive equipment.

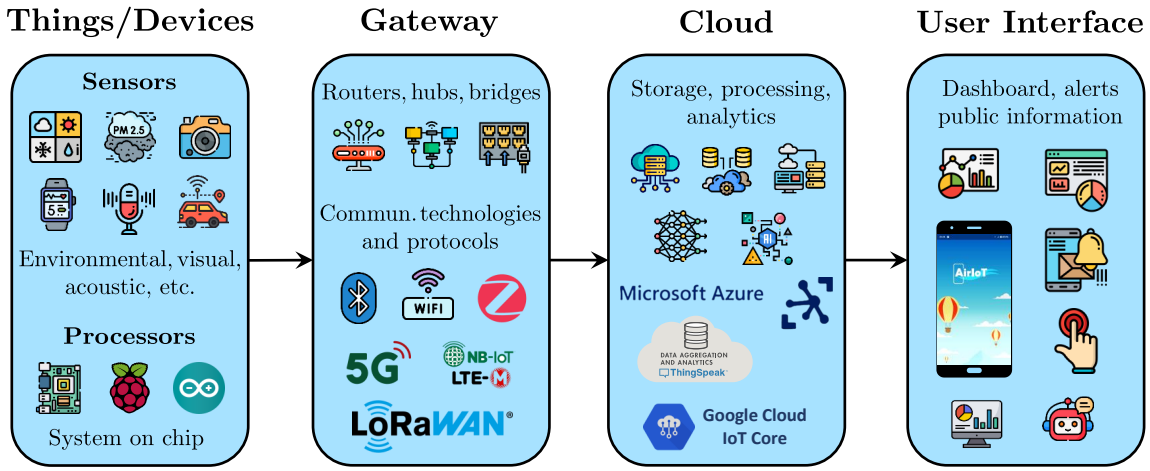

Figure 2.1 Basic components of an IoT system consisting of devices at the edge, gateways connecting them to the cloud, and user interfaces. This thesis focuses on the aspects related to *Things/Devices* and *Gateway* components.

- **Smart agriculture - fostering food security [40, 41]:** IoT can be utilised in various agricultural activities like irrigation, fertilisation, pesticide use, weed management, plant growth monitoring, disease management, and field-level phenotyping. Sensors can be deployed in farms to monitor the concentrations of humidity, minerals and gases in and around the soil. This information can guide watering and fertilisation activities. It can also help detect the health of the plants. Similarly IoT-enabled drones can be used to spray fertilisers, check the growth of weeds and monitor the health of the crop.

2.1.1 *Components of an IoT system*

An IoT system is the interconnection of a device, gateway, cloud and interface as shown in Figure 2.1. These form the basic building block of an IoT system.

- **Thing/Device**: It is simply the object which can exchange data over the internet. It contains a microcontroller, one or more transducers (sensors and/or actuators) and a communication interface to connect to the internet. Based on the application, sensors can sense various parameters or phenomena like temperature, proximity, pressure, motion, light, acceleration, gases, sound, image, infrared radiation, magnetic field, etc. These sensors are interfaced with the microcontrollers to read values, which forms a bridge to the internet through a communication module. Some of the popular micro-controllers used in IoT applications are Arduino, NodeMCU, ESP-32, Raspberry Pi, etc. Although the microcontrollers may not be highly efficient due to low computational demands, the utility remains unhindered. The real potential lies in linking these small-scale objects to higher computing facilities via the Internet. The same is exemplified by connecting a basic speaker and microphone to the *Alexa* smart assistant on the *Amazon cloud*. This transfor-

mative connection, facilitated by the power of IoT, defines its significance in creating a network of interconnected devices.

- **Gateway**: A gateway serves as a communication bridge in the IoT ecosystem, facilitating seamless interaction between diverse devices that may use different protocols. It aggregates and processes data locally, ensuring only relevant information is transmitted to the cloud, reducing latency. The gateway enhances security by implementing protocols, encrypting data, and managing device connectivity. For example, different devices could use different communication technologies like Bluetooth, ZigBee, long range wide area network (LoRaWAN), NB-IoT, long-term evolution (LTE)-M, WiFi, etc. A gateway helps in connecting things with the internet using these communication technologies.

- **Cloud**: Instead of storing all the data locally on the device memory, it can be aggregated at remote servers with large capacity in terms of memory. This is where the cloud comes into the picture. The cloud enables IoT solutions with distributed storage, computational power, and networking capabilities. The cloud can also provide data security by introducing redundancy and recovery capabilities. The cloud also plays an important role in scalability as the storage capacity can be rapidly enhanced to serve a growing network. The could services for IoT can broadly be categorised into infrastructure as a service (IaaS), platform as a service (PaaS) and software as a service (SaaS). Some of the common examples of all the three categories are: IaaS - MathWorks ThingSpeak, Amazon Web Services (AWS), Microsoft Azure, etc., PaaS - Google App Engine, Heroku, Microsoft Azure, etc., SaaS - Google Drive, Salesforce, Office 365, Dropbox, etc.

- **User interface**: It enables the human-device interactions in IoT. It helps the end user control, configure and monitor the device easily and receive processed information from it. Dashboards, mobile apps, Chat-boxes, push notifications and voice commands are the most preferred interfaces of the current generation of users. A well designed user interface can help visualize data for deriving useful and timely insights. User interfaces on platforms like ThingSpeak can also facilitate implementation of software programs for real-time analytics and actuation.

2.1.2 *Technical requirements of an IoT system*

The technical requirements of an IoT system largely depend upon the application. However, some standard requirements are part of almost all the applications. These requirements are explained below with examples from the perspective of an air pollution monitoring application, which is a part of this thesis [P6, P7].

- **Coverage:** Reliable network coverage in IoT deployments is crucial for devices to work well across large geographical areas and at remote places. It's important for the devices to operate smoothly without losing data due to communication outages. To ensure reliable connectivity, one needs to consider the geographical layout, building structures, and environmental conditions. It

is usually believed that only remote locations might have communication issues. However, the experiences from the fieldwork presented in this thesis show that even metro cities like Hyderabad can have dead zones with no or not-so-reliable connectivity. Based on the application, the selected location for deploying an IoT device might be of strategic importance. For example, in air pollution monitoring at a city-wide scale, locations are selected to cover all topographies and potential sources of a city. Encountering a communication dead zone at such locations can compromise the entire planning. When it comes to coverage, there's no one solution that works for every IoT deployment. For indoor home or office environments, short-range networks like WiFi or Bluetooth can be used. However, for ubiquitous coverage in outdoor environments, a heterogeneous ecosystem of both terrestrial and satellite connectivity is required.

- **Energy efficiency:** Most IoT applications are battery-powered and need to conserve energy for long life. Moreover, IoT devices aren't always deployed at easily accessible spots. Consider a city-wide setup of air quality monitors; changing batteries frequently across numerous locations would create a significant burden. Therefore, it is preferable for the devices to be energy-efficient, employing both efficient hardware and firmware. For instance, energy can be conserved by incorporating low-power sensing and communication modules in the hardware. On the software side, adaptive sensing with variable duty cycles can help optimise energy consumption.

  Energy consumption is directly related to the topology and the amount of processing the communication protocol requires. To evaluate the energy consumption, the time the transceiver is active for transmission/reception and idle time should be compared. The time taken for transmission depends upon the MAC protocol and the topology used. The longer the processing and routing time, the larger will be the energy consumed. The topologies and protocols that can facilitate burst transmissions without synchronisation and routing are best suited for IoT applications. Usually, the energy constraint is found at the terminal devices since, in most cases, the receiving station has a virtually infinite energy source (e.g., a base station in a cellular network, a WiFi access point, etc.).

- **Cost and maintenance:** The expense of sensors and other hardware poses a significant challenge in implementing IoT systems. The initial purchase cost can be high, especially when deploying numerous sensors. Variations in cost arise based on factors like sensor type, accuracy, and data collection range. In large-scale deployments like smart cities, low-cost sensors are often chosen. However, these economical sensors demand frequent maintenance and replacements. For example, outdoor air pollution monitoring sensors need regular cleaning and periodic calibration. They also face challenges from harsh environmental conditions that lead to frequent failures. The cumulative maintenance and replacement cost can surpass the initial network setup cost, impacting the overall sustainability of the deployment. Not only cost, frequent maintenance activities lead to long downtime and significant data losses in real-time monitoring systems. Striking a balance between using cost-effective hardware for scalability and investing in high-cost infrastructure for long-term sustainability becomes imperative in addressing this challenge.

- **Scalability:** The network's capability is crucial for accommodating numerous devices and managing the rising data traffic as the IoT deployment expands. It must facilitate horizontal scaling (adding more devices) and vertical scaling (enhancing device capabilities) to meet the growing demands of the deployments. Considering the air pollution monitoring example, the network should effortlessly integrate new devices in the city without extensive technical interventions at the data server and user interfaces. Furthermore, the device's hardware and firmware should embrace a modular approach, allowing the addition of more sensors for diverse pollutants. Implementing multiplexing for various communication protocols to retrieve sensor values and incorporating over-the-air updates for the firmware is beneficial for scalability. This ensures that the network remains flexible and efficient as the deployment expands, seamlessly catering to evolving requirements.

- **Privacy and security:** Modern-day IoT solutions acquire data from various day-to-day activities of the user. Although this data might seem harmless from the security point of view when viewed individually, it can become a potential security and privacy threat when correlated with other sensed information. For example, in the case of a smart speaker or a thermostat, as explained in the previous section, there is a potential threat the device can be used to record private conversations or perhaps the data in the cloud can be used to track the availability of people at home. Hence, IoT solutions need to be secure and privacy-aware.

  Ensuring the security of IoT devices extends beyond safeguarding data privacy; it also encompasses the physical protection of deployed devices, especially in large-scale implementations. Take, for instance, a widespread deployment of air quality monitoring devices across a city. These devices, fitted with sensors and communication modules, are commonly placed on roadsides, electrical poles, and compound walls. The risk arises when these devices are vulnerable to theft, and the communication modules might be exploited to generate fake or harmful data or connect with anti-social elements. Consequently, addressing these devices' physical security becomes paramount in large-scale IoT deployments.

- **Interoperability:** As connected devices increase, interoperability becomes another critical requirement. Seamless data sharing and interaction between different verticals of applications must be enabled with standards that can make the coexistence of different network topologies using different communication protocols possible. Imagine a smart city with diverse IoT deployments for weather monitoring, smart streetlighting, air quality monitoring, and intelligent traffic signalling. These solutions might use different communication technologies and store data on various servers with distinct protocols. For instance, streetlighting or traffic signalling applications could employ a mesh network, while weather or air quality monitoring networks might use a separate topology connecting devices directly to the server. The true potential of a smart city emerges when data from different applications collaborates. For instance, air quality data could inform traffic signalling to alleviate congestion in areas with dense traffic. Conversely, data like traffic den-

sity and visibility can be used to predict air quality [42, 43]. Similarly, weather data could be utilised to predict rain or hailstorms and control street lighting for improved visibility. The seamless coordination of indoor humidifiers and air purifiers based on external weather conditions can also be feasible. Achieving such integration requires a layer of interoperable standards like *oneM2M* [44], which provide architecture, API specifications, and security solutions enabling the effortless exchange of data and derived analytics [45, 46].

- **Quality of service:** Depending on the specific IoT application, the network should prioritise and allocate resources appropriately to meet the required quality of service (QoS) parameters, such as reliability, latency, and throughput. The QoS mechanisms should also prioritise critical or high-priority traffic, ensuring that important data packets receive preferential treatment over non-critical traffic.

2.2 LPWAN communication technologies for IoT

LPWAN, a communication paradigm that gained prominence in the 2010s, emerged as a complementary solution to traditional cellular and short-range wireless technologies, effectively addressing the varied needs of IoT applications [47]. LPWANs enable the long-range connection of numerous objects, intermittently transmitting small data amounts, all while maintaining energy efficiency, often relying on batteries with a lifespan of several years. LPWAN technologies offer distinctive attributes, providing wide-area connectivity for low-power, cost-effective, and low-data-rate devices, characteristics not adequately addressed by legacy wireless technologies. The LPWAN technologies are adaptable, supporting both licensed and unlicensed spectrum. In the licensed spectrum, IoT technologies evolved from existing 3GPP cellular standards, resulting in relatively complex PHY and MAC layers. Some examples of LPWAN technologies in the licensed spectrum are LTE for Machine Type Commutation (LTE-M) and NB-IoT, and in the unlicensed spectrum are Sigfox and LoRaWAN. These technologies are described briefly below.

2.2.1 *Sigfox*

Sigfox emerged as a pioneering company dedicated to IoT communications, introducing the innovative ultra-narrowband (UNB) technology [48]. It was founded in 2009, with its headquarters in Toulouse. Sigfox employs a UNB PHY layer with differential binary phase shift keying (DPSK) modulation in the uplink and Gaussian frequency shift keying (GFSK) in the downlink [49]. To improve reliability and mitigate interference effects, it employs the transmission of the same packet three times in sequence on random carrier frequencies. Sigfox operates in a random frequency and time division multiple access (RFTDMA) protocol, utilising an Aloha-based approach for random access in both time and frequency. Operating in the 868 MHz ISM band in the EU, Sigfox achieves low data rates of 100 bps in uplink and 600 bps in downlink, occupying a band of about 100 Hz around the carrier within

a spectrum of several hundreds of kHz. Sigfox's UNB technology ensures extensive coverage with a single base station, reaching several tens of kilometres in terrestrial communications with low energy consumption. Although, in theory, free space line-of-sight (LoS) communications could span several hundreds of kilometres, real-world observations indicate a practical range of approximately 60 km. For QoS assurance, Sigfox implements spatial diversity, decoding uplink messages at all base stations within range, with duplicates processed in the core network. A downlink transmission is also available after sending a message if needed.

2.2.2 *LoRaWAN*

LoRaWAN, derived from "Long Range" and first standardised in 2015, was developed by the French company Cycleo and later acquired and patented by Semtech [50]. Deployed in a star-of-star topology, LoRa enables communication over several kilometres in urban areas and extends to 15 kilometres or more in rural regions, showcasing its long-range capability [51]. An essential feature of LoRa solutions is their ultra-low power requirements, facilitating the development of battery-operated devices with a lifespan of up to 10 years. The LoRaWAN PHY layer utilises chirp spread spectrum (CSS) modulation, employing sine waves known as chirps [52]. With a constant envelope, the CSS waveform minimises transmitter energy consumption. The binary information flow is divided into subsequences of length spreading factor (SF), forming symbols. Unlike systems with no spreading spectrum, CSS fixes the signal bandwidth based on the chirp's linear frequency evolution over the symbol time. Increasing the SF results in a longer symbol duration, decreasing the data rate. However, this also enhances communication range. The LoRaWAN signals in the same frequency bands with different SFs are orthogonal, but two packets with the same SF in the same slots will collide. LoRaWAN operates in fixed bandwidths of either 125 KHz or 500 KHz while trading off the receiver sensitivity and data rate. Depending upon the SF and the bandwidth, it can offer data rates between 0.3 to 50 kbps.

2.2.3 *Narrowband IoT (NB-IoT)*

Introduced by 3GPP in 2016, NB-IoT is derived from the LTE standard and operates on licensed frequency bands, departing from the conventional cellular network bands. It utilises orthogonal frequency division multiple access (OFDMA) for downlink transmission with a 15 kHz subcarrier spacing (SCS) and single carrier frequency division multiple access (FDMA) for uplink transmission, supporting both single-tone (ST) and multi-tone (MT) transmissions [55]. The transmission modes can be integrated into an LTE carrier as a physical resource block (PRB), either in-band or in the guard band. Additionally, NB-IoT introduces Stand-alone operation, enabling the NB-IoT carrier to replace a GSM carrier with a width of 200 kHz. NB-IoT adopts protocol enhancements such as extended discontinuous reception and power-saving mode to meet stringent energy consumption requirements. For enhanced coverage, many repetitions are employed during initial network access and data transmission [55]. The devices maintain ultra-low complexity by utilising a single receive antenna, operating in half-duplex mode, employing

Table 2.1 Comparison of LPWAN techniques *w.r.t* various technological features/parameters [53, 54].

Technology	**Sigfox**	**LoRaWAN**	**NB-IoT**
Modulation	DBPSK and GFSK (Ultra narrow band)	Chirp Spread Spectrum	DL: OFDMA UL: SCFDMA
Topology	Star	Star-of-star	Star
Frequency	868/915/433 MHz (ISM-Unlicensed)	868/915/433 MHz (ISM-Unlicensed)	400-2200 MHz (Licensed)
Bandwidth	100 Hz	125/250/500 kHz	200 kHz
Max. data rate	100/600 bps	0.3-50 kbps	Upto 250 kbps
Range	Urban: 3-10 km Rural: 30-50 km	Urban: 5 km Rural: 15 km	Urban:1km Rural: 10 km
Channel access	RF-TDMA + Aloha	Aloha	HD-FDD TDMA + FDMA
Max. payload length	DL: 8 bytes UL: 12 bytes	243 bytes	1600 bytes
Max. messages/day	DL: 4 UL: 140	Depends on regional regulation on duty cycle	Unlimited

convolutional coding on the downlink, and limiting peak data rates through the use of quadrature phase-shift keying modulation. The peak data rate for NB-IoT is 250 kbps in downlink and 250 or 20 kbps in uplink for multi-tone and single-tone, respectively. NB-IoT also suffers from some known limitations. It is not backwards compatible with 2G/3G, it does not support mobility, and it is unsuitable for low-latency applications. However, NB-IoT leverages existing LTE infrastructure, making it easier for telecom operators to deploy and manage. This integration provides a significant advantage in coverage and reliability, as cellular networks are widespread and well-established.

Based on the above discussion, a comparison of various technological features and parameters is tabulated in Table 2.1 for easy reference of the reader. A thorough comparison of all the above LPWAN technologies is also presented in [53, 54]. In [53], it is concluded that Sigfox and LoRaWAN excel in network capacity, device lifetime, and cost, while NB-IoT performs well in quality of service and latency. On the other hand, [54] focuses on systematically identifying key characteristics and requirements for LPWAN-based communication applications for IoT. The requirements are further mapped to design considerations, including traffic management, energy efficiency, security, and interworking, with specific attention to proprietary LPWAN technologies.

2.3 Satellite Communication

With 5500+ satellites already launched as of Nov. 2023, SpaceX Starlink has proved that launching satellites is no longer rocket science [56]. The LEO constellations like Starlink, OneWeb, Iridium, Telesat, Amazon Kuiper and many more under development have started a new era of affordable satel-

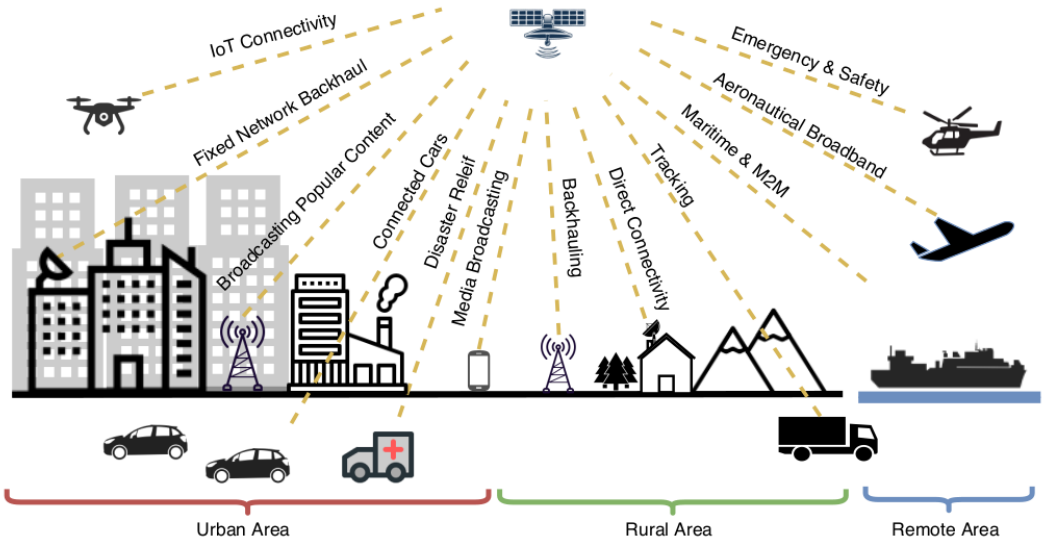

Figure 2.2 The role of satellites in the 5G ecosystem [24].

lite communication. On top of that, nanosatellites called CubeSats with standardised form factors have drastically reduced the turnaround time of building a satellite. All these NGSO systems have found applications across sectors, including aeronautical, maritime, military, and disaster relief, contributing to global telecommunication services, as shown in Figure 2.2. Envisioned as a solution for future non terrestrial network (NTN) meeting 6G system requirements, NGSO satellites align with the goals set by the 3GPP standards group, aiming to integrate satellite communication networks with terrestrial networks [6, 57]. Their ubiquitous coverage and connectivity capabilities ensure resiliency and continuity to mobile platforms beyond the reach of a terrestrial cell site, such as aircraft, high-speed trains, sea vessels, and land-based vehicles [58].

2.3.1 *Role of satellites*

Many roles for satellites with area-wise applications are identified in detail in [59]. Based on the application scenario, the key areas where the satellites can play a role can be categorised as follows:

1. **Coverage**: Satellites can help roll out communication services in remote and un-served areas by cost-effectively enhancing the performance of traditional terrestrial networks. The inherent advantage of satellites in coverage is anticipated to grow with the upcoming mega-LEO constellation, which can offer fine-grained geolocation access without any service discontinuity.

2. **Massive machine-type communication (mMTC)**: Satellites, with their intrinsic broadcasting capabilities, become ideal for dispersed M2M/IoT networks, efficiently reaching many devices with minimal resource consumption. They enable massive data aggregation through geo observation and efficient sharing of uplink connectivity across extensive network areas.

3. **Resilience provisioning**: Satellites can help establish a resilient communication network by mitigating the problem of overload/congestion. Intelligent routing functionality can be implemented to ensure that everyone gets served with a wider range of services.

4. **Caching close to edge and multi-cast**: Network scalability and quality of experience (QoE) can be improved by satellite's broadcast and multi-cast capabilities when used for caching content closer to the network edge. This content delivery can be managed efficiently through software-defined networks/network functions virtualisation (NFV) with a centralised controller optimising satellite links for immediate and on-demand content access.

Based on the above roles and with lower OPEX and CAPEX compared to GSO, the NGSO satellites, particularly in LEO, are most efficiently suited to support wide-area IoT services. Leveraging this, the satellite-IoT connectivity based on LEO constellations is expected to have a compound average growth rate of 25% between 2022–2026 and the global revenue is expected to surpass 1 billion USD by 2026 [60]. For example, IoT for smart operations such as farms, oil/gas installations, electric grid, environment monitoring, etc., can benefit from satellite by extending the coverage to remote locations [61].

2.3.2 *Satellite use-cases*

Future satellite networks are expected to be evolutionary rather than revolutionary. This is because not every application requires all the satellite features, and the existing terrestrial network is still progressing with network capabilities. It is not expected that all the key performance indicators will be met in a single application simultaneously. The same is true for satellite use cases as well, and hence, there is a need to distinguish them based on application scenarios. Similarly, the access spectrum for these applications also depends on their use case and needs to be selected based on the performance requirements.

It is understood that *ubiquity*, *mobility*, *broadcast*, and *security* are the major offerings, but still, it makes more sense to understand the satellite use-cases scenario-wise [24]. Although the focus of this study is on IoT use-cases, other use-cases are also discussed in brief for complete understanding.

2.3.2.1 Satellite use-case for IoT:

The major requirement in massive machine type communication (mMTC) or IoT is that the resource-constrained devices (sensors/actuators) should be able to communicate among themselves and to the internet without any network complexity. Although individual sensors do not generate large amounts of data, collectively, a densely deployed IoT network can impact the network load significantly. The satellite can help offload the terrestrial IoT networks deployed at remote locations by providing service continuity. Based on the deployment scenario, these can again be of two types:

- *Wide area IoT services*: The use-case is related to networks deployed over a large geographical area. This can benefit applications like smart girds, weather monitoring, transport and agriculture.

- *Local area IoT services*: IoT devices in this scenario are expected to share the locally sensed information with a central server. Examples include smart grid sub-systems, services on board moving platforms, etc.

2.3.2.2 Satellite use-case for eMBB:

Use-cases for enhanced mobile broadband (eMBB) are majorly divided into the following categories:

- *Backhauling and tower feed*: Satellite is used for providing backhaul support in transporting traffic load from the network's edge or broadcasting popular content to the edge of the network.
- *Trunking and headend feed*: Satellite provides direct connectivity to areas where terrestrial network deployment is impossible due to difficult terrain geography.
- *Hybrid multiplay*: Hybrid terrestrial broadband communication provides 5G services to home and office premises in unsaved areas.
- *Communication on the move*: Direct or relayed connectivity can be provided to the user on-board a moving platform like an aeroplane, ship or high-speed train.

2.3.2.3 Satellite use-case for uRLLC:

Most of the ultra-reliable low latency communication (uRLLC) use cases are mission-critical. They require extremely low communication link delay (lower than 1 ms) and high reliability (1 packet loss in 10^5 packets). It is understood that because of the large orbital heights, satellites cannot meet the low latency requirements irrespective of orbit. However, it does not necessarily keep satellites out of business in these use cases. Satellites can still play a crucial supportive role. For example, intelligent broadcasting of locally cached data (either at the edge or terminals) can create the perception of low latency. Similarly, they can broadcast software updates or traffic updates in autonomous driving applications.

2.3.3 *Frequency bands for satellite-IoT*

Selecting frequency bands for IoT access through NGSO satellites involves considering factors like cost, complexity, and application requirements. Two primary categories of services emerge: one involving numerous devices for fixed or mobile services, collecting intermittent and small data volumes over an extensive geographical area; the other emphasising high reliability and availability, crucial for monitoring critical infrastructure. In the former, low-cost and low-complexity technologies, frequencies especially below 6 GHz, are preferred, allowing for affordable commercial-off-the-shelf components for both terrestrial and satellite-IoT access. In contrast, the latter category demands more sophisticated antenna and RF subsystems, potentially utilising frequency bands above 6 GHz with increased user equipment antenna directivity and gain.

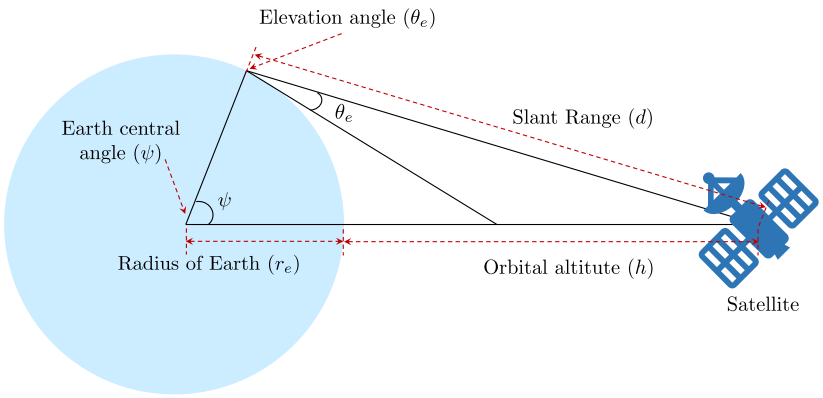

Figure 2.3 Orbital geometry of LEO satellite with altitude h and elevation angle θ_e.

Overlapping frequency bands below 3 GHz for terrestrial and satellite mobile services pose cooperation challenges, requiring coordination among existing operators to address interference concerns. Strategies for frequency sharing among NGSO systems for satellite uplink access involve either imposing transmit power limits without coordination or fostering proactive collaboration among different NGSO satellite systems. The latter, though challenging, aligns with the common interest of NGSO satellite service providers to enhance service quality. Recognising the need for harmonised frequency usage, various administrations have pursued studies and resolutions, leading to Agenda Item 1.18 at the World Radio Communication Conference (WRC) 2019 [62]. This item aims to assess new spectrum allocations for NGSO satellite systems delivering low-data-rate services. The importance of harmonised frequency usage is emphasised in preparations for the WRC in 2027, which may consider a possible global frequency allocation for low-data-rate services in the 1.5–5 GHz band.

2.3.4 *Orbital characteristics of LEO satellites*

The orbital characteristics of satellites are presented in [22, 63, 64] in detail. These books initially consider a simple orbital model derived using Kepler's law of motion. They then incorporate more practical assumptions like perturbations due to the non-sphericity of Earth, pull from the sun, moon and other atmospheric drags. The focus of this thesis does not encompass these perturbations. Hence, a simple orbital model assuming the Earth to be spherical is considered in this thesis. The various orbital parameters that will be useful for performance analysis in future chapters are explained below.

2.3.4.1 Slant distance, angular velocity and period around Earth

Consider a satellite in a circular orbit at an altitude h from the surface of the Earth. Then, based on the orbital geometry as shown in Figure 2.3, the slant distance d between the satellite and the user can be calculated as

$$d = \sqrt{r_e^2 \sin^2 \theta_e + h^2 + 2h\, r_e} - r_e \sin \theta_e \quad \text{km}, \tag{2.1}$$

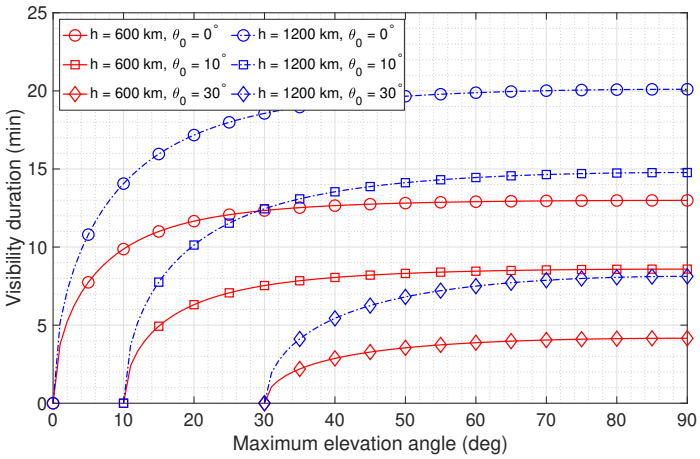

Figure 2.4 Visibility duration t_{vis} of a LEO satellite vs. the observed maximum elevation angle θ_{max} of the pass at 81° inclination for varying altitude, h and mask angle θ_0. It can be observed that in a zenith pass, the satellites spend most of the visibility duration at lower elevation angles.

where r_e is the radius of the Earth (≈ 6378.15 km), θ_e is the elevation angle. The angular velocity of the satellite in the Earth-centered inertial frame is given in [65] as

$$\omega_I = \sqrt{\frac{G\,M_e}{r^3}} \quad \text{rad.sec}^{-1}, \tag{2.2}$$

where G is the gravitational constant ($\approx 6.672 \times 10^{-11}$ $\text{m}^3\text{kg}^{-1}\text{s}^{-2}$), M_e is the mass of the earth ($\approx 5.9736 \times 10^{24}$ kg), and r is the radius of the satellite orbit ($= r_e + h$). Based on the angular velocity, the period of the satellite, i.e. the time taken to complete one revolution around the Earth, is given by

$$T_e = 2\,\pi\sqrt{\frac{r^3}{G\,M_e}} \quad \text{sec.} \tag{2.3}$$

2.3.4.2 Satellite visibility duration

The visibility time of a LEO satellite depends on the orbit, relative user position on the ground, and the elevation angle. A minimum elevation or mask angle is usually defined for communication with the LEO satellites. A satellite's total visibility duration is defined as the time for which the satellite remains visible at an elevation greater than the mask angle. The visibility duration $\tau(\theta_{\text{max}})$ of the satellite at the terminal is given in [66] by

$$\tau(\theta_{\text{max}}) \approx \frac{2}{\omega_s - \omega_e \cos\theta_i} \cos^{-1}\left(\frac{\cos(\cos^{-1}(\frac{r_e}{r}\cos\theta_0) - \theta_0)}{\cos(\cos^{-1}(\frac{r_e}{r}\cos\theta_{\text{max}}) - \theta_{\text{max}})}\right) \quad \text{sec}, \tag{2.4}$$

where ω_s is the angular velocity of the satellite, ω_e is the angular velocity of the Earth's rotation, θ_i is the inclination of the orbit, θ_0 is the angle of elevation to the satellite at a time when the satellite becomes visible to the terminal and θ_{max} is the maximum angle elevation to the satellite. Figure 2.4 shows the vari-

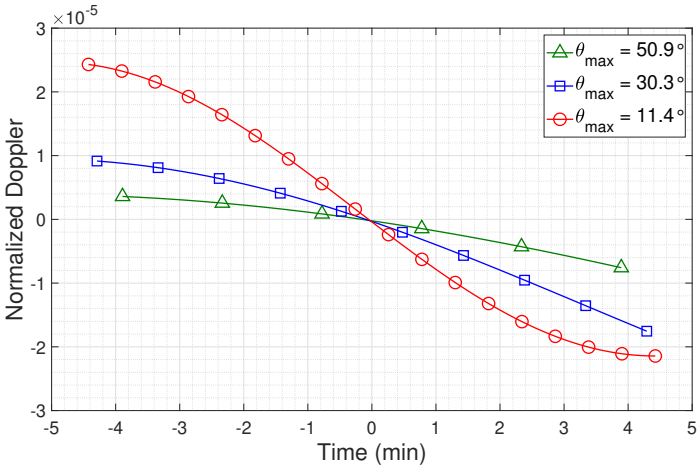

Figure 2.5 Normalised Doppler S-curve for different maximum elevation angles for a representative satellite scenario as shown in [66].

ation in visibility duration w.r.t maximum elevation angle at 81° inclination for different altitudes and mask angles. The visibility duration is greater for the passes with higher maximum elevation angles. It can also be observed that in a zenith pass, the satellites spend most of the visibility duration at lower elevation angles. For example, the visibility duration for a satellite in 600 km orbit with a mask angle of 30° is nearly 4 minutes. In contrast, the visibility duration is 13 minutes if the mask angle is considered 0°. This demonstrates that for a zenith pass, the satellite spends nearly 9 minutes to traverse from 0° to 30°.

2.3.4.3 Doppler characteristics for LEO satellites

LEO satellites are favourable for IoT networks because of their lower rount trip time (RTT) and lower propagation loss in the communication link as compared to the GEO. However, terminals experience significant Doppler shifts due to higher relative motive between the satellite and the terminal. Some of the earliest work characterising Doppler for LEO satellites is presented in [66].

Doppler frequency at terminals in the case of LEO satellites varies with the time that can be parameterised by the maximum elevation angle from the terminal to the satellite during the visibility window. The normalised Doppler is given by [66]

$$\frac{\Delta f}{f} = -\frac{1}{c}\frac{r_e r \sin(\psi(t)-\psi(t_0))\cos(\cos^{-1}(\frac{r_e}{r}\cos\theta_{\max})-\theta_{\max})\omega(t)}{\sqrt{r_e^2+r^2-2r_e r\cos(\psi(t)-\psi(t_0))}\cos(\cos^{-1}(\frac{r_e}{r}\cos\theta_{\max})-\theta_{\max})}, \tag{2.5}$$

where t_0 is the time instant of maximum elevation angle during visibility time, $\omega(t)$ is the angular velocity of the satellite and $\psi(t)-\psi(t_0)$ is the angular distance between the sub-satellite points at the time instant t and instant when the terminal observe the maximum elevation angle. It is clear from (2.5) that the normalised Doppler is a function of maximum elevation angle $\theta_{\max}$ and the angular velocity $\omega(t)$ of the satellite. Figure 2.5 shows the variation of normalised Doppler as a function of maximum elevation angle. As we know that the earth is rotating on its axis, the relative position of the GS changes

with respect to the orbital plane for every satellite pass. This is significant for LEO satellites since they move much faster over the earth. Therefore, it is obvious that the path for the satellite over the ground station is different for different passes, and hence, the communication duration for every pass depends on the maximum elevation angle of that pass. It is seen that normalised Doppler takes an S-curve when plotted w.r.t time. The magnitude of the Doppler shift is maximum at the onset and termination of the visibility duration since both the time and the elevation angle are minimum. The Doppler shift decreases as the time proceeds and the elevation angle increases. The minimum Doppler shift is experienced at the time of maximum elevation angle.

The Doppler characterisation presented in [66] can be used to improve the performance of the phase-locked loop at the terminal. The visibility duration and the instant of maximum elevation can also be estimated at the terminals. This information can help design many other PHY and MAC layer protocols. For example, IoT devices can be made to wake only during the visibility duration and can be under sleep/hibernation for the rest of the time. This will increase the power efficiency many folds. Similarly, Doppler-aware access protocols can be designed such that the terminals communicate their information at the instant of maximum elevation angle. LEO orbits are advantageous for IoT applications because of their low propagation loss, which is crucial for maintaining low complexity and link budget. Usually, it is assumed that the Doppler shift due to fast-moving LEO satellites can be compensated with novel OFDMA-based transmission [67]. But, apart from the Doppler shift, there is also an issue of differential Doppler shift, which arises due to the fact that different users inside a coverage area experience different channels due to their locations and differences in elevation angle. Usually, this differential part of the Doppler would also be expected to be compensated on the user side, but it becomes difficult in IoT where the devices are low-complexity devices. Hence, [68] presents a resource allocation approach to compensate for differential Doppler in the case of IoT while maintaining the same complexity. The coverage area is remodelled into smaller regions such that the differential Doppler inside the new region is below the allowed threshold. Having done the remodelling, the next question to be answered is how to assign the up-link resources in the new regions. Authors in [68] propose two methods for resource allocation in this scenario. The first method uses time division multiple access (TDMA), where the eNB assigns the NB-IoT carrier to a particular sub-region for a certain time. For a system with N sub-regions, this method reduces the throughput of the system by a factor of N. The second method uses FDMA, where different NB-IoT carriers are allocated to different sub-regions. In this method, carrier orthogonality must be maintained between sub-carriers inside one NB-IoT carrier and among NB-IoT carriers. Although satisfactory results have been achieved in [68], it assumes static user devices and considers the peak values of the differential Doppler, even though it can change over time. Hence, a dynamic resource allocation scheme with moving users can be developed for a more practical system.

2.4 Basic architecture of satellite communication

The basic architecture of a satellite communication system consists of a space segment, a ground segment and a user segment. The space segment includes the satellite constellation, and the ground seg-

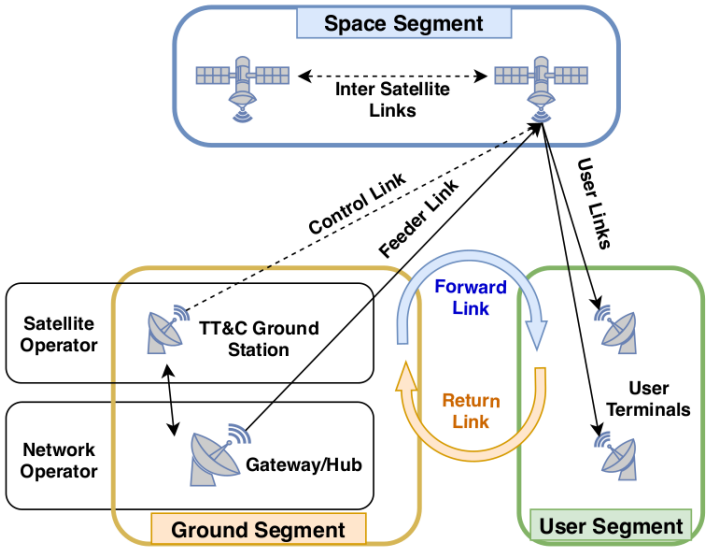

Figure 2.6 Basic architecture of a satellite communication system [24].

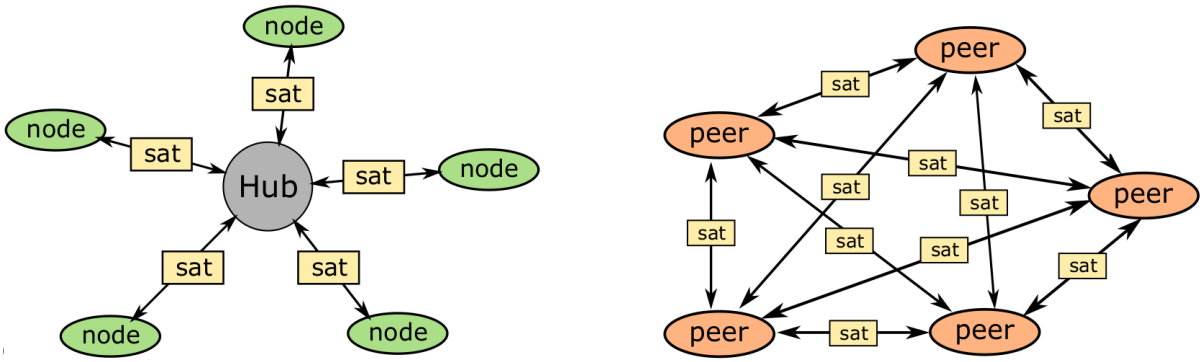

Figure 2.7 Commonly used communication topologies (a) star topology (b) mesh topology [24].

ment includes the gateway (GW) stations and large ground facilities for control and network operations. The user segment includes the user terminals, which can be on fixed or mobile platforms [21]. The link between the satellite and user equipment is called a user link, whereas the link between the satellite and GS is called a control link. The link between the satellite and GW is called a feeder link. A telemetry, tracking and command (TT&C) station runs tests to monitor the status of the satellite sub-systems and updates the configuration if required. On the other hand, the GW is maintained by the network operator to manage network access and backhauling. This basic architecture is shown in Figure 2.6. LEO satellites require a substantially large number of gateways when compared to medium earth orbit (MEO) and GEO as it has a smaller coverage area.

The communication topology to be used primarily depends upon the application. The most common topologies used are star and mesh [24] as shown in Figure 2.7. For point-to-point connectivity, as in

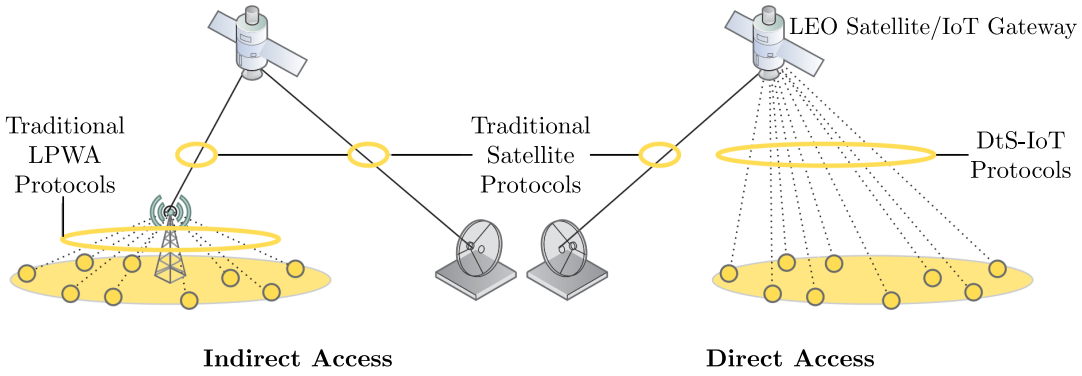

Figure 2.8 Direct and indirect modes of connectivity for satellite-IoT [69].

video conferencing, where the end-to-end packet transmission latency is important, mesh topology is usually preferred. In a mesh topology, each peer device can communicate with another peer device via a satellite relay. However, this topology requires an intelligent routing of data packets by the satellite. The star topology is mostly used in point-to-multipoint connectivity scenarios, like in the case of traditional broadcast services or data offloading from sensors deployed on terrestrial surfaces. Particularly in the case of IoT, as shown in Figure 2.8, star topology can be implemented in two modes [69]: direct access and indirect access. In direct access mode, the IoT devices communicate with the satellite directly, while in indirect mode, the IoT devices connect with the satellite through a terrestrial LPWAN gateway/relay. Such gateways have small aperture satellite terminals and traditional terrestrial LPWAN radio modules. However, the use of indirect access is limited by the coverage of the terrestrial gateway. Investing in gateways is also not profitable in applications deployed at locations hit by disasters or locations requiring deployments for a short duration. In contrast to this, direct access mode is an appealing solution for such scenarios. With technological advancement, low-powered radio communication modules are developed by companies like Lacuna, Kepler, Astrocast and Hiber, which offer direct access to satellite communication from IoT devices [70–73]. However, much more research is required to comprehensively analyse the performance of direct access satellite-based IoT networks.

Another essential aspect of satellite communication within the scope of this thesis is the role played by the communication payload. Regardless of the specific topology employed, the satellite functions as a relay or repeater, facilitating communication between the device and the GW. This scenario can be modelled as a cooperative communication system where the satellite can be modelled as a relay. A typical cooperative communication system operates in two phases: (1) Initially, the source sends the information signal to the relay, and (2) The relay re-transmits the received information to the destination. The relay functionality can, in turn, be of two types: transparent or regenerative [20, Ch. 9].

2.4.1 *Transparent payload (amplify-and-forward)*

In transparent mode, the satellite payload amplifies and re-transmits the received signals without any modifications or processing apart from spatial filtering and frequency conversion. It is essentially

an amplify-and-forward (AF) structure [74]. The primary purpose of the AF mode is to extend the satellite's coverage area. The received signal at the relay and the destination can be written as

$$y_{s,r} = \sqrt{P_s}\, h_{s,r}\, x_s + n_{s,r}, \tag{2.6}$$

$$z_{r,d} = \sqrt{P_r}\, g_{r,d}\, \beta_{\text{AF}} \left(\sqrt{P_s} h_{s,r} x_s + n_{s,r} \right) + w_{r,d}, \tag{2.7}$$

where P_s and P_r are the transmit power of the source and the relay, respectively. Similarly, $h_{s,r}$ and $g_{r,d}$ are the coefficient of the source-relay and relay-destination channels, x_s is the unit energy information signal, and $n_{s,r}$ and $w_{r,d}$ are the additive white Gaussian noise (AWGN) noise at the relay and destination receiver, respectively. Here, β_{AF} is the AF gain factor and is defined as

$$\beta_{\text{AF}} \triangleq \frac{\sqrt{P_s}}{\sqrt{P_u\, |h_{s,r}|^2 + \sigma^2}}. \tag{2.8}$$

Thus, the end-to-end instantaneous SNR between the source and the destination can be written as

$$\gamma_{\text{AF}} = \frac{G_{r,d}\, H_{s,r}}{G_{r,d} + \frac{1}{\beta_{\text{AF}}\, \sigma^2}}, \tag{2.9}$$

where $H_{s,r} = P_s\, |h_{s,r}|^2/\sigma^2$, and $G_{r,d} = P_r\, |g_{r,d}|^2/\sigma^2$. Depending upon the way the gain factor is defined, the above relaying scheme can be of two types: fixed or variable gain relaying.

2.4.2 *Regenerative payload (decode-and-forward)*

In a regenerative mode, the satellite performs additional signal processing like decoding, interference cancellation and signal regeneration. This is much like the traditional decode-and-forward (DF) structure, where the signal received at the relay is decoded and then re-encoded by the relay before re-transmission to the destination. Contrary to the AF relaying, the received signal at the destination in DF relaying can be written as

$$z_{r,d} = \sqrt{P_r}\, g_{r,d}\, \hat{x}_s + w_{r,d}, \tag{2.10}$$

where $\hat{x}_s$ is the re-encoded information signal generated at the relay. The end-to-end instantaneous SNR between the source and the destination in DF relaying can be written as

$$\gamma_{\text{DF}} = \min\left(H_{s,r}, G_{r,d}\right), \tag{2.11}$$

Based on how decoding is performed at the relay, the above relaying scheme can be fixed or selective DF relaying. A thorough performance comparison between AF and DF is presented in [74]. Although AF amplifies both the signal and noise, it achieves spatial diversity by transmitting over two spatially independent channels. On the other hand, DF relaying can offer significantly higher gains than AF schemes, as it removes noise at the relay prior to transmission, contingent on decoding performance. But, the complexity of the AF protocol with a fixed gain is less than the DF protocol. Moreover, the

performance gain varies with modulation types, with larger signal constellation sizes yielding lower gains. Consequently, for high data-rate cooperative communications, especially those employing large signal constellation sizes, adopting the AF cooperation protocol may be preferable to reduce system complexity while maintaining comparable performance. The network-controlled repeaters introduced in Release 18 [75] and the integrated access backhaul nodes introduced in Release 16 [76] are examples of AF and DF relays [77], respectively.

2.5 Link budget and reference parameters for satellite-IoT

This section presents the link budget for both downlink (DL) and uplink (UL) of direct access satellite-based IoT network using the reference parameters standardized in [6]. The SNR at the receiver is calculated as a function of the equivalent isotropically radiated power (EIRP), the receiver antenna gain-to-noise-temperature (G/T) ratio, the Boltzmann's constant $k_{\mathrm{B}} = -228.6$ dBW/K/Hz, the free-space propagation loss $\mathrm{L_{FS}}$, the atmospheric losses $\mathrm{L_A}$, the shadowing margin $\mathrm{L_{SF}}$, the scintillation loss $\mathrm{L_{SL}}$, and the signal bandwidth (BW). The calculation of each of these parameters is explained below.

2.5.1 *Antenna gain and EIRP*

The Antenna-gain-to-noise-temperature G/T can be derived using

$$G/T\ [\mathrm{dB}] = G_R\ [\mathrm{dBi}] - N_f\ [\mathrm{dB}] - 10\log_{10}\left(T_0\ [\mathrm{K}] + (T_a[\mathrm{K}] - T_0\ [\mathrm{K}])\, 10^{-0.1 N_f\ [\mathrm{dB}]}\right), \quad (2.12)$$

where G_R is the antenna gain of the receiver, N_f is the noise figure, T_0 is the ambient temperature and T_a is the temperature of the antenna. The antenna gain of the receiver G_R is given by

$$G_R\ [\mathrm{dBi}] = \begin{cases} G_{R,e}[\mathrm{dBi}] + 10\log_{10}\left(N_{R,a}\right) - L_p[\mathrm{dB}], & \text{array antenna} \\ 10\log_{10}\left(\eta \cdot \pi^2 \cdot \dfrac{D\ [m]^2}{\lambda\ [m]^2}\right), & \text{parabolic antenna} \end{cases} \quad (2.13)$$

where $G_{R,e}$ is the element gain of the receiver antenna, $N_{R,a}$ is the number of receiver antenna elements, L_p is the polarization loss, η is the antenna aperture efficiency, D is the equivalent diameter of the antenna, and λ is the wavelength. The efficiency of the antenna aperture is typically considered to be between 0.55 and 0.70 for parabolic antennas. The EIRP can be calculated using

$$\mathrm{EIRP}\ [\mathrm{dBW}] = P_T\ [\mathrm{dBW}] - L_C\ [\mathrm{dB}] + G_T\ [\mathrm{dBi}], \quad (2.14)$$

where P_T is the transmit power of the antenna, L_c is the cable loss, and G_T is the antenna gain of the transmitter. The transmit antenna gain G_T can be calculated as

$$G_T\ [\mathrm{dBi}] = \begin{cases} G_{T,e}\ [\mathrm{dBi}] + 10\log_{10}\left(N_{T,a}\right), & \text{array antenna} \\ 10\log_{10}\left(\eta \cdot \pi^2 \cdot \dfrac{D\ [m]^2}{\lambda\ [m]^2}\right), & \text{parabolic antenna} \end{cases} \quad (2.15)$$

where $G_{T,e}$ is the element gain of the transmit antenna and $N_{T,a}$ is the number of transmit antenna elements.

2.5.2 *Path loss and shadow fading*

The signal undergoes several stages of propagation and attenuation while traversing its path from the satellite to an NTN terminal. The total path loss, PL, can be calculated as

$$PL\ [\text{dB}] = PL_b\ [\text{dB}] + PL_g\ [\text{dB}] + PL_s\ [\text{dB}], \tag{2.16}$$

where PL_b is the basic path loss, PL_g is the loss due to atmospheric gases, and PL_s is the loss due to ionospheric or tropospheric scintillations. The basic path loss is composed of the free space path loss and the loss due to shadow fading, as given below

$$PL_b = FSPL\,(d, f_c) + SF. \tag{2.17}$$

The free space path loss is a function of slant distance d between the satellite and the user and the frequency of operation f_c in GHz. It can be calculated as

$$FSPL\,(d, f_c) = 32 - 45 + 20\log_{10}(f_c) + 20\log_{10}(d). \tag{2.18}$$

The shadow fading loss is modelled using Normal distribution i.e., $SF \sim \mathcal{N}(0, \sigma^2_{SF})$, where σ^2_{SF} depends upon the elevation angle and the probability of line-of-sight.

2.5.3 *Atmospheric and scintillation loss*

Attenuation induced by atmospheric gases, primarily resulting from absorption, is influenced by frequency, elevation angle, altitude above sea level, and water vapour density (absolute humidity). Generally, at frequencies below 10 GHz, this attenuation is often negligible. Nevertheless, for elevation angles less than 10 degrees, it is advisable to conduct calculations for frequencies exceeding 1 GHz.

Ionospheric scintillation, characterized by rapid fluctuations in both amplitude and phase of the received signal, is a phenomenon considered for frequencies below 6 GHz. These phenomena pose significant challenges for signals below 3 GHz along a trans-ionospheric propagation path, with occasional observations extending up to 10 GHz [78]. The occurrence of scintillations is contingent upon factors such as location, time of day, season, and solar and geomagnetic activity. Strong scintillation levels are infrequently noted in mid-latitudes under normal conditions, but they tend to be a daily occurrence post-sunset in low-latitude regions. Higher latitudes, including auroral and polar regions, may experience moderate to strong scintillations. However, tropospheric scintillation, another phenomenon causing rapid amplitude and phase fluctuations in signals, arises from sudden changes in the refractive index due to variations in temperature, water vapour content, and barometric pressure. Its impact intensifies with higher carrier frequencies, notably above 10 GHz. Additionally, the effects of tropospheric scintillation

Table 2.2 Reference parameters for satellite-IoT [6].

Parameter	Reference value
Frequency band	S-band (i.e. 2 GHz)
Orbit	Low Earth circular orbit
Altitude	600 km
Payload type	Transparent (AF) and regenerative (DF)
Minimum elevation	10°
Maximum beam footprint size	1000km
Max Round Trip Delay (propagation delay only)	25.77 ms (service and feeder links)
Max Doppler shift	24 ppm
User maximum Tx power	20 dBm or 23 dBm
Device channel Bandwidth	DL: 180 kHz, UL: up to 180 kHz
User density	400/km2
Central beam center elevation angle	Set-1: 30°, Set-4: 90°
Central beam edge elevation angle	Set-1: 27°, Set-4: 30°
3 dB beam width	Set-1: 4.4127°, Set-4: 104.7°
Satellite EIRP density (dBW/MHz)	Set-1: 34, Set-4: 21.45
Satellite G/T (dB/K)	Set-1: 1.1, Set-4: -18.6

amplify with increasing carrier frequency and lower elevation angles, owing to the extended signal path and wider beam width of receiving antennas.

Finally, the link budget i.e., the SNR, can be calculated using

$$\begin{aligned}\mathrm{SNR}\,[\mathrm{dB}] =& \mathrm{EIRP}\,[\mathrm{dB}] + G/T\,[\mathrm{dB}] - k_{\mathrm{B}}\,[\mathrm{dB/K/Hz}] - \mathrm{L_{FS}}\,[\mathrm{dB}] - \mathrm{L_{A}}\,[\mathrm{dB}] - \mathrm{L_{SF}}\,[\mathrm{dB}] \\ & - \mathrm{L_{SL}}\,[\mathrm{dB}] - 10\log_{10}(\mathrm{BW}\,[\mathrm{Hz}]) - 3\,[\mathrm{dB}]. \end{aligned} \tag{2.19}$$

A 3 dB additional loss is added to the link budget at the edge due to the assumption that the DL/UL EIRP is the one at the beam centre and not at the edge of the beam. 3GPP has defined four sets of beam layout and radio frequency parameters for the payload: Set-1, Set-2, Set-3, and Set-4. Set 1 represents the best-case scenario with small spot beams. On the contrary, the Set-4 configuration represents the general and worst cases with one large beam. Table 2.2 provides the various configuration parameters for LEO satellites at 600 km altitude. All the reference parameters have been selected based on the 3GPP report TR-38.811 [79], TR-38.821 [80], and TR-36.763 [6]. Based on these parameters, the link budget with the estimated SNR has been calculated as presented in Table 2.3.

2.6 MAC protocols for satellite-IoT

MAC protocols distribute the resources for the devices to use the communication channel efficiently. Communication in IoT needs efficient MAC protocols, which can be implemented with low complexity

Table 2.3 Link budget for direct access satellite-IoT.

Parameters	**LEO - 600 km**							
Transmission mode	Downlink (Set-1)		Downlink (Set-4)		Uplink (Set-1)		Uplink (Set-4)	
Elevation angle	27	30	30	90	27°	30°	30°	90°
TX EIRP [dBW]	26.55		14		-7		-7	
RX G/T [dB/K]	-31.62		-31.62		1.1		- 18.6	
$BW_{NB\text{-}IoT}$ [kHz]	180		180		3.75/180		3.75/180	
Free space PL [dB]	159.7	159.1	159.10	154.03	159.7	159. 1	159.1	154.03
Atmospheric loss [dB]	0.1							
Shadow margin [dB]	3							
Scintillation loss [dB]	2.2							
Polarization loss [dB]	3							
Additional losses [dB]	3	0	3	0	3	0	3	0
SNR [dB]	**-0.02**	**3.58**	**-11.97**	**-3.9**	**15.96/-0.85**	**19.56/2.75**	**-3.14/-19.95**	**4.93/-11.88**

and can support many devices. Every protocol is designed considering application requirements; it could be the performance in terms of transmission rate, delay, hardware complexity or energy consumption. Following are some of the standard metrics used for analyzing the performance of a MAC protocol.

- *Normalized Offered Load*: It is the ratio of all the data transmitted into the network to the maximum data that could be sent at the transmission rate of the link.
- *Normalized Throughput:* It is the ratio between data received by satellite in a given time to all the data that could be sent continuously at the transmission rate of the link.
- *Packet Loss Ratio (PLR):* It is the ratio between data lost or received with errors to the total amount of data sent.
- *Energy Consumption:* It is directly related to the time duration in which the data is being sent or received and the amount of processing required by the protocol. It is usually evaluated by comparing the time for which the device is involved in transmission, reception or ideal state. SigFox has around 11 mA and 125 mA of current consumption in reception and transmission. In LoRaWAN, the peak current consumption is about 32 mA, whereas NB-IoT uses around 120 mA to 300 mA during its peak transmission [81].

In the literature [81, 82], two kinds of MAC protocols, fixed assignment-based protocols and random access-based protocols, are discussed for satellite IoT applications.

2.6.1 *Fixed assignment based MAC protocols*

In these protocols, separate resources in time, frequency or both are allotted to every user for data transmission, avoiding collision. NB-IoT is one of the most famous technologies that use fixed assign-

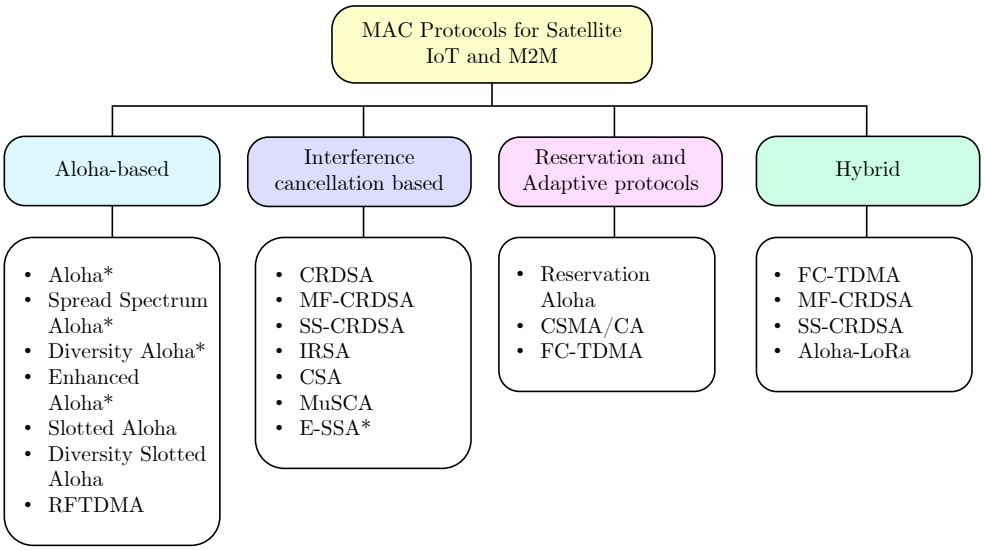

Figure 2.9 Taxonomy of random access protocols for satellite-IoT networks [81].

ment MAC protocol by assigning a dedicated sub-carrier for every device. It uses single carrier-FDMA for uplink and OFDMA for downlink. It requires strict synchronisation to maintain the orthogonality in time and frequency; otherwise, the system would suffer from inter-channel interference. They are easy to implement and make efficient link usage if the application can occupy all or most of the resources. However, protocols following a fixed assignment are not flexible enough to change data rates. Also, a higher round trip delay and Doppler shift in satellite links need to be managed for efficient implementation.

2.6.2 *Random access based MAC protocols*

In an IoT network, all the devices are not always active. It is done for saving energy and extending battery life. In many applications, devices wake up to offload bulk data and then sleep again. Hence, the demand or traffic in large IoT networks remains dynamic. Random access-based MAC protocols are preferred for such IoT applications. In the random access protocol, the devices transmit the data without any prior coordination. Since multiple devices could be transmitting on the same resource, packet collisions can take place. Figure 2.9 presents the taxonomy of random access protocols evaluated for satellite-IoT networks. Protocols with * are the ones which require no time synchronisation. Aloha is the most famous random access protocol, a version of which is indeed used by LoRa and SigFox. Although it satisfies the complexity constraint of IoT devices very well, it faces stability issues when the number of devices is enormous due to increased propagation delay in satellite channels. Some of the other attractive ones in terms of spectral and energy efficiency are enhance spread-spectrum ALOHA (E-SSA), contention resolution diversity ALOHA (CRDSA) and asynchronous contention resolution

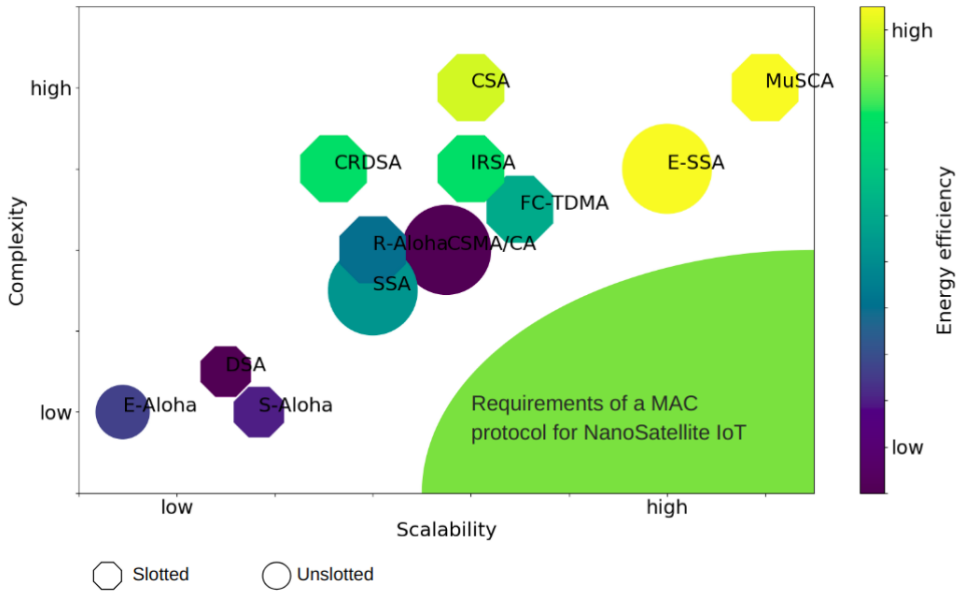

Figure 2.10 A comparison of existing MAC protocols in the context of satellite-IoT networks [81].

diversity ALOHA (ACRDA). In [83], the following key metrics for comparison and selection of various random access techniques are presented:

- **Power limitations of IoT devices:** As IoT networks target low-cost terminals, power constraints become critical. Effective random access solutions must navigate packet collisions and ensure a PLR with minimal energy per symbol. Notably, random access protocols like E-SSA, CRDSA with MARSALA, and ACRDA exhibit robust performance, requiring lower SNR levels compared to the alternatives.
- **Low data rates:** In the context of IoT, where low-power consumption is pivotal, terminals often transmit signals at very low data rates. Consequently, random access solutions designed for low rates, such as E-SSA and MF-CRDSA, are particularly relevant. Using higher data rate access schemes could introduce significant delays in packet transmission due to the frame structure.
- **Large number of devices:** To handle the challenges posed by dense networks, an effective random access scheme should deliver low PLR in high-load scenarios. Schemes like CRDSA combined with MARSALA, ACRDA, and E-SSA showcase average throughput performance exceeding 1 bit/symbol, even with a low PLR of 10^{-3}.
- **Signalling overhead:** The IoT networks often have sporadic traffic traffic profiles with low duty cycles per terminal. Consequently, minimising the transmission of signalling packets, particularly for synchronisation purposes, is crucial. The use of asynchronous random access is favoured over synchronous random access due to its potential to reduce interference and achieve a lower PLR.

Figure 2.10 visually compares the existing MAC access protocols in the context of satellite-IoT networks. Much work has been done in the field of random access protocols. However, there is still scope for much more to be done in the context of satellite-IoT. In environments where low data rates and low power consumption are desired, phase noise can cause the loss of packets at low signal-to-interference-plus-noise ratio (SINR) levels. Many interesting questions remain unanswered, like whether to use packet redundancy or spectrum spreading or whether to achieve low data rates with high phase noise or high data rates with less sensitivity to phase noise. The answer to all these questions would also depend on the topology being used. Hence, it is of great importance to comprehensively analyse random access schemes for topologies like a star, which suits satellite-IoT networks.

2.7 Recent advancements

The proliferation of new constellation types with advances in onboard processing has played a major role towards building the motivation for satellite-IoT networks. The craze for NTN (unmanned air vehicles and high altitude platforms) has catalysed the whole process. The ongoing projects and supportive standardisation activities are helping maintain the momentum.

2.7.1 *Standardization activities*

In the current 3GPP landscape, the standardisation for NTN including satellite-IoT in Release 17 has been announced [6], and now the primary focus is on finalising specifications for Release 18 alongside exploring potential technologies and network enhancements for inclusion in Release 19. The study in [6] explores the feasibility of utilising NB-IoT and eMTC technologies in non-terrestrial environments. It examines the technical aspects, performance characteristics, and potential enhancements required to enable efficient communication for IoT devices in NTN scenarios. It also identifies the requirements and enhancements needed to adapt NB-IoT and eMTC technologies for non-terrestrial deployments. This includes considerations for mobility management, synchronisation, interference management, power control, and overall system optimisation to ensure reliable and efficient communication over NTN. The report also evaluated the performance of NB-IoT and eMTC in NTN scenarios through simulations, analysis, and measurements. It assessed parameters like coverage, capacity, latency, and power consumption to understand the capabilities and limitations of these technologies in non-terrestrial environments.

Another important effort towards building a roadmap for technological advancement and use cases for satellites is being made at the IEEE Future Networks forum. The latest report presents various reference scenarios mapped to diverse applications and use cases for IoT [9]. Various challenges associated with satellite-IoT are also stated under near, mid and long-term categories, along with potential solutions. Based on the latest report, the following reference scenarios are formulated:

1. *Reference scenario A*: This scenario considers LEO satellite-based constellations with multiple fixed beam satellites in the visible range for direct access from IoT users. As shown in Figure

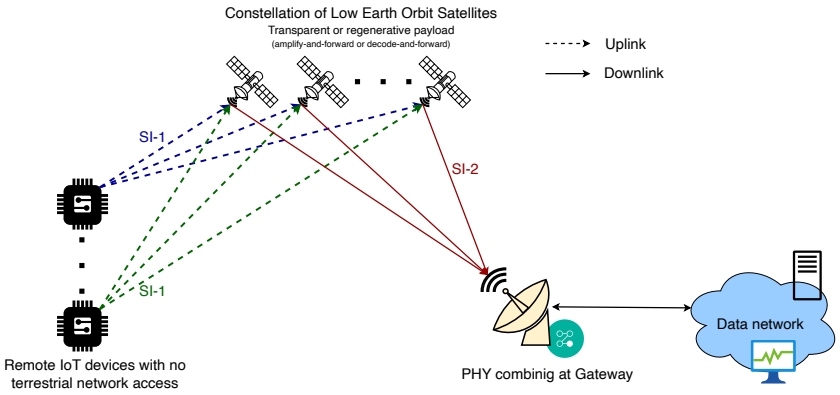

Figure 2.11 Reference scenario A (direct access, transparent payload) and B (direct access, regenerative payload). Reference scenarios C and D are also similar but with steerable beams.

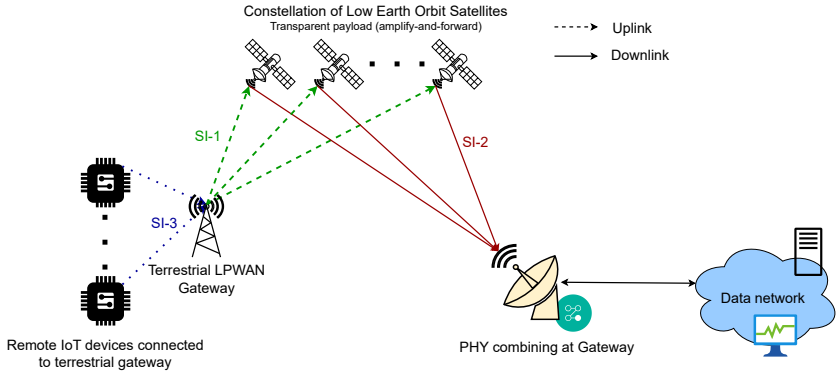

Figure 2.12 Reference scenario E (in-direct access, terrestrial gateway, transparent payload).

2.11, a transparent payload (AF) is assumed for this scenario. It is suitable for large deployments of IoT networks with no scope for terrestrial gateways and applications which can withstand reasonable latencies and outages (ex., weather monitoring).

2. *Reference scenario B*: This scenario considers LEO satellite-based constellations with multiple fixed beam satellites in the visible range for direct access from IoT users. As shown in Figure 2.11, a regenerative payload (DF) is assumed for this scenario. It is suitable for large deployments of IoT networks with no scope for terrestrial gateways and applications which require greater immunity towards propagating transmission errors.

3. *Reference scenario C and D*: This is like the topology for reference scenario A (direct access and transparent payload) and reference scenario B (direct access and regenerative payload), respectively, but with steerable beams.

4. *Reference scenario E*: This scenario considers LEO satellite-based constellation with multiple steerable beam satellites in the visible range for IoT access via a terrestrial gateway. As shown in Figure 2.12, a transparent payload (AF) is assumed for this scenario. It is suitable for IoT

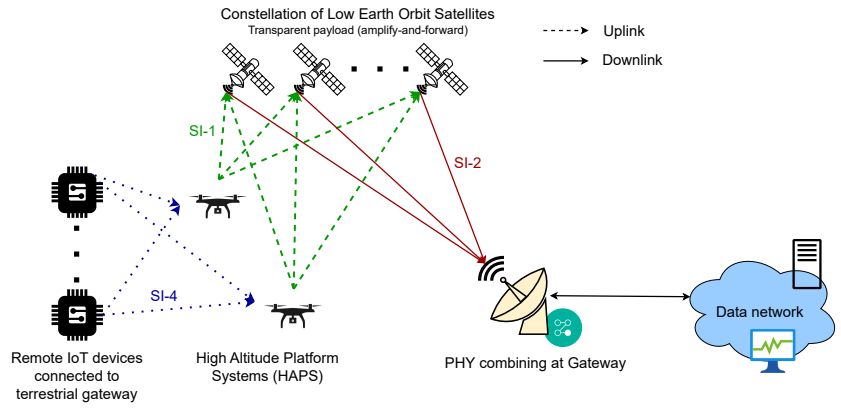

Figure 2.13 Reference scenario F (in-direct access, with HAPS, transparent payload).

Table 2.4 Applications/use-cases mapped to reference scenarios for Satellite-IoT.

Application/Use-Case	**Reference Scenario**
A dense network of rural and urban air quality monitoring	Scenario A, B, C, D, E
Railway track condition monitoring	Scenario A, B, C, D
Crowd monitoring (eg. large gatherings, stadiums, sports events)	Scenario E, F
Smart agriculture applications – monitoring and actuation	Scenario C, D, F
Intrusion detection or emergency (SOS) reporting	Scenario B, D, F

deployments with the feasibility of establishing terrestrial gateways and applications that require lesser latency and outages (e.g., real-time crowd monitoring in large gatherings or sports events).

5. *Reference scenario F*: This scenario considers LEO satellite-based constellation with multiple steerable beam satellites in the visible range for IoT access via HAPS. As shown in Figure 2.13, a transparent payload (AF) is assumed for this scenario. It is suitable for IoT deployments with the feasibility of coverage via drones/balloon facilities/HAPS in a limited area. It can benefit applications like crowd monitoring, smart agriculture, and intrusion detection.

Based on the technical requirements, various applications and use cases are also mapped to these reference scenarios, as shown in Table 2.4.

2.7.2 *Upcoming mega LEO constellations*

Mega LEO constellations, a group of hundreds of small satellites in LEO, have become famous recently. Table 2.5 shows the specifications of a few upcoming mega-LEO constellations. These constellations involve deploying hundreds or thousands of small satellites in low Earth orbit, working together to provide widespread coverage and high-speed internet access to even the most remote regions. Companies such as SpaceX's Starlink, Amazon's Project Kuiper, and OneWeb are at the forefront of

Table 2.5 Upcoming mega LEO constellations.

Constellation	**Starlink**	**OneWeb**	**Kuiper**	**TelSat**
Number of satellites	12,000+	720	3200	300+
Altitude (km)	540-570	1,200	610-630	1015-1325
Frequency Band	Ku, Ka	Ku (2.5 GHz), Ka (3.5 GHz)	Ka (20 GHz, 30 GHz)	Ka (4 GHz)
Announced market	Broadband, backhaul	Broadband, mobility	Broadband, IoT, Transportation	Broadband (Aviation and Maritime)

this new era, with ambitious plans to create constellations that will blanket the Earth with connectivity. These mega-LEO constellations leverage advanced technologies like inter-satellite links and low-latency communications to offer improved performance and reduced signal latency compared to traditional geostationary satellites. With the potential to bridge the digital divide and enable a myriad of applications, ranging from IoT connectivity to remote sensing, these upcoming mega-LEO constellations are set to reshape the way we connect and communicate in the near future.

2.7.3 *Projects in the field of satellite-IoT networks*

The following are some of the most recognised ongoing projects in the field of satellite-IoT networks:

- ***Lacuna Space*:** A LoRaWAN based satellite-IoT service provider providing connectivity for a wide range of IoT applications, including asset tracking, environmental monitoring, agriculture, and logistics [70].

- **everywhereIOT™ - *Kepler Communications Inc*.:** It is a test bench developed by Kepler Communications Inc. It integrates a satellite communication module with an IoT device to enable global connectivity using Ku band LEO satellite [71].

- ***Astrocast*-direct to satellite IoT connectivity:** Building a nanosatellite network to deliver IoT connectivity. They aim to provide low-power and cost-effective communication solutions for IoT devices in remote and challenging environments. They have also launched *Astronode DevKit*, a proprietary L-band, LEO satellite chipset optimised for direct-to-satellite IoT applications [72].

- ***Hiber*:** Working on a network of nanosatellites that provide global IoT connectivity, targeting applications such as well and pipeline monitoring for oil and gas industries [73].

- ***Sateliot*:** LEO satellite communication service provider to offer global satellite IoT connectivity with 3GPP Rel-17 NB-IoT satellites [84].

- ***Swarm Technologies***: Provides low-bandwidth satellite connectivity using ultra-small LEO satellites. Satellites orbit at 450-550 km altitude, with global coverage.

- **Indian efforts towards CubeSats**: The Indian Space Research Organization (ISRO) and other private companies like *Skyroot Aerospace* are at the forefront of developing affordable launch vehicles for rapid deployment of CubeSats [85–87]. Other companies like *XDLinx Labs* are also developing satellite platforms with hosted payloads supported for IoT applications [88].

2.8 Discussion

This chapter explored the building blocks of IoT networks and satellite communication. As highlighted in the thesis's motivation and scope, the LPWAN communication technologies and characteristics of LEO satellites are central to this thesis. Hence, the following discussion is presented as a key takeaway, laying the groundwork for future chapters. The insights gained and assumptions made will guide the formulation of the system model in the coming chapters.

Although LPWAN technologies are at the forefront of supporting large IoT deployments, there are challenges in adopting them in their current form for LEO satellite-based IoT networks. For example, in Sigfox, the small bandwidth of UNB messages contributes to high spectrum efficiency, accommodating more devices simultaneously without overlap, addressing the requirements of the IoT market. This low spectral occupation also enhances resistance to interference, a crucial feature in the unlicensed band. However, in the context of LEO satellites, the small bandwidth of UNB signals makes them sensitive to frequency drifts, a common occurrence in LEO satellite systems.

Recently, many studies have evaluated the feasibility of utilising LoRaWAN with LEO satellites [89–93]. In this context, one of the challenges is the high probability of packet collisions due to the multitude of connected end devices. Although LoRaWAN, with CSS modulation, demonstrates resilience to narrowband and UNB interference, intra-technology interference is a significant concern, especially when signals with different SFs collide. Another challenge involves the Doppler effect. LoRaWAN signals, particularly those with longer symbol times, face difficulties, especially when decoding performance is impacted by Doppler time-variation. SF12, SF11, and SF10 are the only configurations with a link budget suitable for LEO satellite communication. Mitigating the impact of Doppler shift requires various treatments, considering the synchronisation algorithms and carrier frequency offset limitations.

Similarly, studies have been conducted to evaluate the feasibility of utilising NB-IoT with LEO satellites [94–98]. In this regard, the high-speed motion of LEO satellites would introduce the Doppler effect, causing inter-carrier interference [99]. Notably, the presence of high Doppler rates (up to 300 Hz/s) can challenge NB-IoT signal demodulation, particularly for long-duration packets with the lowest data rates. Existing literature proposes various approaches to estimate and compensate for the Doppler shift, which is crucial for effective communication in such scenarios [67, 68, 96].

A list of challenges outlined for individual technologies in the above discussion is summarised below in general terms for easy reference. Addressing these challenges is imperative to establish LPWANs as viable solutions for LEO satellite communication.

1. **Link budget:** LPWAN devices typically operate with low power to conserve energy and extend battery life. Hence, maintaining an adequate signal strength at the satellite receiver is challenging due to the long distance between the devices and the satellites.

2. **High packet collisions due to large field-of-view (FOV):** Due to the high altitude position of satellites, the FoV enables the connection of many devices, in turn increasing the likelihood of packet collisions. This scenario raises the number of lost packets and adversely impacts the throughput of LPWANs. Additionally, the energy consumption of nodes is increased as lost packets are typically re-transmitted after a random period. Therefore, mitigating these issues is crucial to enhance the suitability of LPWANs for LEO satellite communications.

3. **Impact of high Doppler shift:** It is induced by the high-speed relative motion between the devices and the LEO satellites. While static Doppler shifts can be mitigated using various techniques, the Doppler time variation poses a significant problem, especially for LPWAN technologies with extended packet durations and low data rate transmissions.

Chapter 3

Proposed Direct Access Topology for Satellite-IoT: Basic Performance Analysis

This chapter presents the direct access topology proposed in this research. It begins with introducing the topology and discussing its structure, configuration, and key features. An architecture is proposed that suits sensing heavy IoT applications and also leverages the benefits of existing and upcoming mega LEO constellations. The chapter then describes the employed channel model and presents a basic outage analysis for a simplified system model without considering interference. Finally, an asymptotic analysis for SNR is conducted to gain insights into the achieved diversity order and gain by the proposed topology. By encompassing these topics, this chapter aims to lay the basic foundation for a comprehensive understanding of the proposed topology and the analysis presented in the subsequent chapters.

3.1 System description

A LEO satellite-based direct access architecture is considered, where a set of terrestrial IoT users communicate with a GS using S LEO satellites, as shown in Figure 3.1. Similar to the NB-IoT, where dedicated sub-carriers of 3.75 kHz or 15 kHz are utilised, it is assumed that these IoT users utilize separate frequency carriers such that there is no interference from adjacent users [100, 101]. Hence, the analysis is performed for a single IoT user, and the same can be extended for other users as well. As per the proposed system model, the IoT user broadcasts its information to all the S satellites. The signal received at each of the S LEO satellites is amplified and forwarded to the GS for data processing.

The end-to-end communication between the IoT user and the GS takes place in two phases. In the first phase, the IoT user broadcasts its information signal to S satellites. The received signal at the s^{th} satellite can be written as

$$y_s = \sqrt{P_u}\, h_{us}\, x_u + n_s, \tag{3.1}$$

where P_u is the transit power of the IoT user, h_{us} is the coefficient of the channel between the IoT user, and the s^{th} satellite, x_u is the unit energy information signal and n_s the additive noise modelled as independent and identically distributed (i.i.d.) symmetric complex Gaussian with mean zero and

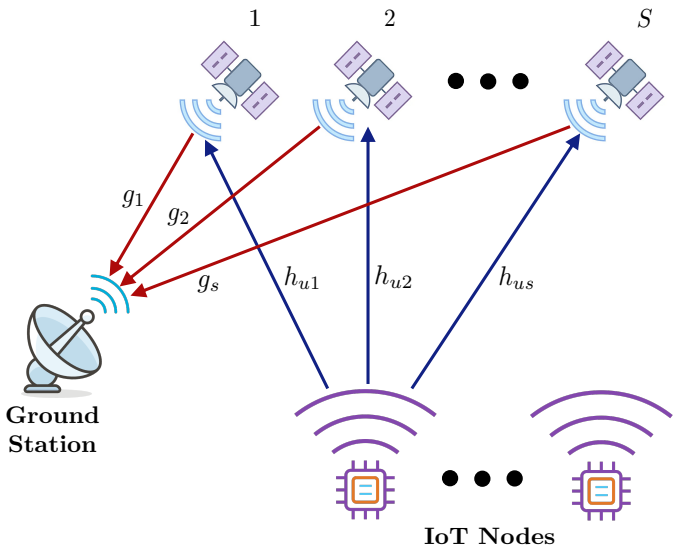

Figure 3.1 Schematic diagram of the proposed LEO satellite-based direct access network where multiple IoT users communicate to GS using S LEO satellites, which are in LoS.

variance σ^2. The instantaneous SNR at the s^{th} satellite for the user-satellite link can be written as $H_{us} = P_u|h_{us}|^2/\sigma^2 = \eta_u|h_{us}|^2$, where $\eta_u = \frac{P_u}{\sigma^2}$.

In the second phase, each satellite relays the signal received from IoT user to the GS by employing AF relaying scheme and using dedicated orthogonal resources. Therefore, the signal received at the GS from the s^{th} satellite can be written as

$$z_s = \sqrt{P_s}\, g_s\, \beta_{\text{AF}}\, (\sqrt{P_u} h_{us} x_u + n_{us}) + w_s, \tag{3.2}$$

where P_s is the transit power of the s^{th} satellite, g_s is the coefficient of the channel between the s^{th} satellite and the GS, β_{AF} is the AF gain factor and w_s is the AWGN noise at the GS receiver. The instantaneous SNR at the GS for a satellite-GS link can be written as $G_s = \eta_s|g_s|^2$, $\eta_s = P_s/\sigma^2$. Note that all the channel coefficients corresponding to user-satellite and satellite-GS links i.e., h_{us} and $g_s, \forall s$, are assumed to follow shadowed-Rician (SR) distribution. The SR fading model is best known for characterizing communication links that suffer from LoS shadowing and small-scale fading [102]. It is a more generalized form of the Rician fading model where the amplitude of the LoS component follows Nakagami-m fading. Moreover, this model is widely accepted for characterizing satellite channels and fits the experimental data very well.

We compare the performance of this architecture in terms of OP at the GS for three different schemes:

- *Scheme-1 (SS)*: In this scheme, information is decoded at the GS using the signal received from a single satellite (SS) only. This scheme does not leverage the benefits of mega-constellations but offers simplicity and lower implementation costs. It also suffers from limited reliability and is

more vulnerable to signal degradation due to fading and loss of LoS. It serves as the baseline for comparing other schemes.

- *Scheme-2 (SC)*: In this scheme, information is decoded at GS using SC in which a strong signal out of S received signals from S LEO satellites is selected for decoding. This scheme is computationally simple and requires minimal hardware since only one branch is active at any time. Although it offers less diversity gain than other methods, it significantly improves signal quality over single-path transmission.
- *Scheme-3 (MRC)*: In this scheme, information is decoded at the GS after coherently combining of S received signals using MRC technique. superior performance, especially in high SNR conditions, by effectively combining the strengths of all available signals to combat fading and improve robustness. While MRC achieves the highest possible diversity gain, it requires more complex processing and greater resource allocation, making it most suitable for systems where achieving the best signal quality is a priority and computational resources are available.

Further to proceed with the derivation of expressions for OP, the instantaneous end-to-end SNR at the GS for scheme-1 (SS) can be derived as

$$\gamma^{\text{SS}} = \frac{G_s\, H_{us}}{G_s + C}, \tag{3.3}$$

where β_{AF} is the AF gain factor defined in [103] as

$$\beta_{\text{AF}} = \left(P_u |h_{us}|^2 + \sigma^2\right)^{-\frac{1}{2}}, \tag{3.4}$$

and $C = 1/\beta_{\text{AF}}^2\, \sigma^2$. Considering variable gain relaying [103], the term C can be simplified as

$$\begin{aligned} C &= \frac{P_u |h_{us}|^2 + \sigma^2}{\sigma^2} \\ &= 1 + H_{us}. \end{aligned} \tag{3.5}$$

Similarly, the end-to-end SNR at the GS under scheme-2 (SC) and scheme-3 (MRC) are derived as

$$\gamma^{\text{SC}} = \max_{s} \left(\frac{G_s\, H_{us}}{G_s + C} \right), \tag{3.6}$$

$$\gamma^{\text{MRC}} = \sum_{s=1}^{S} \frac{G_s\, H_{us}}{G_s + C}. \tag{3.7}$$

The instantaneous SNRs in 3.3, 3.6, and 3.7 are used to calculate the system performance in terms of OP based on a threshold. The threshold typically represents the minimum SNR required to establish the communication link and is selected based on the data rate targeted for the application.

3.2 Statistical characteristics of shadowed-Rician channel

The probability density function (PDF) and cumulative distribution function (CDF) of $X \in \{H_{us}, G_s\}$ are given, respectively in [104] by

$$f_X(x) = \alpha_i \sum_{\kappa=0}^{m_i-1} \frac{\zeta(\kappa)}{\eta_i^{\kappa+1}} x^{\kappa} e^{-\left(\frac{\beta_i-\delta_i}{\eta_i}\right)x}, \tag{3.8}$$

$$F_X(x) = 1 - \alpha_i \sum_{\kappa=0}^{m_i-1} \frac{\zeta(\kappa)}{\eta_i^{\kappa+1}} \sum_{p=0}^{\kappa} \frac{\kappa!}{p!} \left(\frac{\beta_i-\delta_i}{\eta_i}\right)^{-(\kappa+1-p)} \times x^p e^{-\left(\frac{\beta_i-\delta_i}{\eta_i}\right)x}, \tag{3.9}$$

where $\alpha_i = ((2b_i m_i)/(2b_i m_i + \Omega_i))^{m_i}/2b_i$, $\beta_i = 1/2b_i$, $\delta_i = \Omega_i/(2b_i)(2b_i m_i + \Omega_i)$ and $\zeta(\kappa) = (-1)^{\kappa}(1-m_i)_{\kappa}\delta_i^{\kappa}/(\kappa!)^2$ with $(\cdot)_{\kappa}$ being the Pochhammer symbol [105], and m_i, b_i and Ω_i being the parameters of the distribution. Here, m represents the shape parameter of the Nakagami-m faded LoS component, $2b_i$ denotes the average power of the multipath components, and Ω_i is the average power of the LoS component.

3.3 Outage performance of proposed direct topology

In this section, the performance of the proposed architecture is analyzed by deriving the closed-form expressions for OP in all three schemes. The OP of SS and SC schemes are derived in closed form using a step-staircase approximation method. However, for MRC, since obtaining the closed-form expression was not mathematically tractable, an approximation is used to arrive at an exact expression. This expression is later solved using numerical techniques. All the approximations and employed numerical techniques are described in detail below.

3.3.1 *Scheme-1: Single satellite (SS)*

The OP at the GS in the case of a single satellite can be evaluated as

$$\begin{aligned} P_{\text{out}}^{\text{SS}}(\mathcal{R}) &= \Pr\left[\frac{1}{2}\log_2(1+\gamma^{\text{SS}}) \leq R\right] \\ &= \Pr\left[\frac{G_s\, H_{us}}{G_s + C} \leq \gamma_{\text{th}}\right], \end{aligned} \tag{3.10}$$

where R is the target rate and $\gamma_{\text{th}} \triangleq 2^{2R} - 1$. Substituting (3.5) in (3.10), it can reformulated as

$$\begin{aligned} P_{\text{out}}^{\text{SS}}(\mathcal{R}) &= \Pr\left[\frac{G_s\, H_{us}}{G_s + H_{us} + 1} \leq \gamma_{\text{th}}\right], \\ &\overset{(a)}{=} \Pr\left[(G_s - \gamma_{\text{th}})(H_{us} - \gamma_{\text{th}}) \leq \gamma_{\text{th}}^2 + \gamma_{\text{th}}\right], \end{aligned} \tag{3.11}$$

where (a) is obtained by arithmetically rearranging the terms. Further, using (3.8), the above expression is mathematically intractable and difficult to solve in closed form. Hence, we employ an M-step-staircase approximation approach as in [106]. Using this approach and considering $\Upsilon = \gamma_{\text{th}}^2 + \gamma_{\text{th}}$, the closed-form expression for $P_{\text{out}}^{\text{SS}}(\mathcal{R})$ is derived as

$$
\begin{aligned}
P_{\text{out}}^{\text{SS}}(\mathcal{R}) \approx\; & F_{G_s}(\gamma_{\text{th}}) + \{F_{H_{us}}(\gamma_{\text{th}}) \times [1 - F_{G_s}(\gamma_{\text{th}})]\} \\
& + \left\{ \left[F_{G_s}(\sqrt{\Upsilon} + \gamma_{\text{th}}) - F_{G_s}(\gamma_{\text{th}})\right] \times \left[F_{H_{us}}(\sqrt{\Upsilon} + \gamma_{\text{th}}) - F_{H_{us}}(\gamma_{\text{th}})\right] \right\} \\
& + \sum_{i=1}^{M} \left\{ \left[F_{G_s}\left(\frac{\Upsilon}{\sqrt{\Upsilon} + \frac{i-1}{M}L} + \gamma_{\text{th}} \right) - F_{G_s}(\gamma_{\text{th}}) \right] \right. \\
& \qquad \left. \times \left[F_{H_{us}}\left(\sqrt{\Upsilon} + \gamma_{\text{th}} + \frac{iL}{M} \right) - F_{H_{us}}\left(\sqrt{\Upsilon} + \gamma_{\text{th}} + \frac{(i-1)L}{M} \right) \right] \right\} \\
& + \sum_{i=1}^{M} \left\{ \left[F_{H_{us}}\left(\frac{\Upsilon}{\sqrt{\Upsilon} + \frac{i-1}{M}L} + \gamma_{\text{th}} \right) - F_{H_{us}}(\gamma_{\text{th}}) \right] \right. \\
& \qquad \left. \times \left[F_{G_s}\left(\sqrt{\Upsilon} + \gamma_{\text{th}} + \frac{iL}{M} \right) - F_{G_s}\left(\sqrt{\Upsilon} + \gamma_{\text{th}} + \frac{(i-1)L}{M} \right) \right] \right\}. \qquad (3.12)
\end{aligned}
$$

Proof: To obtain the closed-form expression, we have to solve an equation of the form

$$P_{\text{out}} = \Pr\left[(X - \gamma_{\text{th}})(Y - \gamma_{\text{th}}) \;\leq\; \Upsilon\right] \qquad (3.13)$$

where X, Y and Υ are defined from (3.11) as $X = G_s$, $Y = H_{us}$ and $\Upsilon = \gamma_{\text{th}}^2 + \gamma_{\text{th}}$, respectively. To solve (3.13), we can approximate the integral in five regions as shown in Figure 3.2. For regions 4 and 5, following the process given in [106], we divide the integral region into M vertical blocks. We divide region 4 into M blocks from $Y = \sqrt{\Upsilon} + \gamma_{\text{th}}$ to $Y = \sqrt{\Upsilon} + \gamma_{\text{th}} + (L \times \gamma_{\text{th}})$, where L is the depth of integration. Similarly we divide region 5 into M blocks from $X = \sqrt{\Upsilon} + \gamma_{\text{th}}$ to $X = \sqrt{\Upsilon} + \gamma_{\text{th}} + (L \times \gamma_{\text{th}})$. It is also important to note that, since X and Y are independent random variables, the integral values for regions R_1 to R_3, and ith block of R_4 and R_5 can be evaluated as

$$R_1 = \int_{y=0}^{\infty} \int_{x=0}^{\gamma_{\text{th}}} f_{X,Y}(x, y)\, dx\, dy = F_X(\gamma_{\text{th}}), \qquad (3.14)$$

$$R_2 = \int_{y=0}^{\gamma_{\text{th}}} \int_{x=\gamma_{\text{th}}}^{\infty} f_{X,Y}(x, y)\, dx\, dy = F_Y(\gamma_{\text{th}})\left[1 - F_X(\gamma_{\text{th}})\right], \qquad (3.15)$$

$$R_3 = \int_{y=\gamma_{\text{th}}}^{\sqrt{\Upsilon}+\gamma_{\text{th}}} \int_{x=\gamma_{\text{th}}}^{\sqrt{\Upsilon}+\gamma_{\text{th}}} f_{X,Y}(x, y)\, dx\, dy = \left[F_X(\sqrt{\Upsilon} + \gamma_{\text{th}}) - F_X(\gamma_{\text{th}})\right] \times \left[F_Y(\sqrt{\Upsilon} + \gamma_{\text{th}}) - F_Y(\gamma_{\text{th}})\right], \qquad (3.16)$$

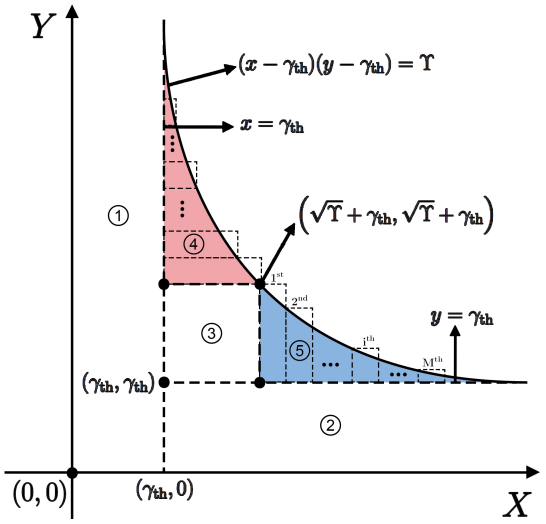

Figure 3.2 Regions of integration for calculating exact OP expression in scheme-1. Regions 1, 2 and 3 are calculated by direct integration. Step staircase approximation is applied for only regions 4 and 5.

$$R_4^i = \int_{y=\sqrt{\Upsilon}+\gamma_{\text{th}}+\frac{i-1}{M}L}^{\sqrt{\Upsilon}+\gamma_{\text{th}}+\frac{i}{M}L} \int_{x=\gamma_{\text{th}}}^{\frac{\Upsilon}{\sqrt{\Upsilon}+\frac{i-1}{M}L}+\gamma_{\text{th}}} f_{X,Y}(x,y)\,dx\,dy$$
$$= \left[F_X\left(\frac{\Upsilon}{\sqrt{\Upsilon}+\frac{i-1}{M}L}+\gamma_{\text{th}}\right)-F_X(\gamma_{\text{th}})\right]\times\left[F_Y\left(\sqrt{\Upsilon}+\gamma_{\text{th}}+\frac{iL}{M}\right)-F_Y\left(\sqrt{\Upsilon}+\gamma_{\text{th}}+\frac{(i-1)L}{M}\right)\right], \tag{3.17}$$

$$R_5^i = \int_{y=\gamma_{\text{th}}}^{\frac{\Upsilon}{\sqrt{\Upsilon}+\frac{i-1}{M}L}+\gamma_{\text{th}}} \int_{x=\sqrt{\Upsilon}+\gamma_{\text{th}}+\frac{i-1}{M}L}^{\sqrt{\Upsilon}+\gamma_{\text{th}}+\frac{i}{M}L} f_{X,Y}(x,y)\,dx\,dy$$
$$= \left[F_Y\left(\frac{\Upsilon}{\sqrt{\Upsilon}+\frac{i-1}{M}L}+\gamma_{\text{th}}\right)-F_Y(\gamma_{\text{th}})\right]\times\left[F_X\left(\sqrt{\Upsilon}+\gamma_{\text{th}}+\frac{iL}{M}\right)-F_X\left(\sqrt{\Upsilon}+\gamma_{\text{th}}+\frac{(i-1)L}{M}\right)\right]. \tag{3.18}$$

The final closed-form expression for OP is given by

$$P_{\text{out}} = R_1 + R_2 + R_3 + \sum_{i=1}^{M} R_4^i + \sum_{i=1}^{M} R_5^i. \tag{3.19}$$

Finally, substituting (3.14)-(3.18) in (3.19) gives (3.12).

3.3.2 *Scheme-2: Selection combining (SC)*

The OP at the GS in the case of the SC can be evaluated as

$$P_{\text{out}}^{\text{SC}}(\mathcal{R}) = \Pr\left[\max_{s}\left(\frac{G_s\, H_{us}}{G_s + C}\right) \leq \gamma_{\text{th}}\right]. \tag{3.20}$$

Further, following the similar analysis as done in the case of scheme-1, the closed form expression for SC under variable gain AF relaying can be derived as

$$P_{\text{out}}^{\text{SC}} = \prod_{s=1}^{S} P_{\text{out,s}}^{\text{SS}}(\mathcal{R}), \tag{3.21}$$

where $P_{\text{out,s}}^{\text{SS}}(\mathcal{R})$ is the OP using the s^{th} satellite in the single satellite scenario for which a generalized expression given in (3.12) for any user.

3.3.3 *Scheme-3: Maximal ratio combining (MRC)*

Using (3.7), the OP in the case of MRC is given by

$$P_{\text{out}}^{\text{MRC}}(\mathcal{R}) = \Pr\left[\sum_{s=1}^{S}\frac{G_s\, H_{us}}{G_s + C} \leq \gamma_{\text{th}}\right], \tag{3.22}$$

Solving (3.22) in closed form using the previously applied step-staircase approximation is not mathematically tractable since it involves summation of SNR random variable. To find an analytically tractable solution, we use the approximation presented in [107] to approximate (3.22) as

$$\gamma^{\text{MRC}} \approx \sum_{s=1}^{S}\min(G_s\,, H_{us}). \tag{3.23}$$

This approximation represents an upper bound on the end-to-end SNR. It is intuitively expected since the end-to-end SNR cannot exceed the individual link SNRs. Therefore, (3.22) can be written as

$$P_{\text{out}}^{\text{MRC}}(\mathcal{R}) \approx \Pr\left[\sum_{s=1}^{S}\min(G_s\,, H_{us}) \leq \gamma_{\text{th}}\right]. \tag{3.24}$$

The first step to finding an expression for the above equation is to find the CDF of $\min(G_s\,, H_{us})$, which is given by

$$F_{\min(G_s\,,H_{us})}(x) = F_{H_{us}}(x) + F_{G_s}(x) - \left(F_{H_{us}}(x)F_{G_s}(x)\right), \tag{3.25}$$

where $F_{H_{us}}(x)$ and $F_{G_s}(x)$ are as given in (3.9). Then the moment generating function of $\min(G_s\,, H_{us})$ can be obtained as

$$M_{\min(G_s\,,H_{us})}(-t) = 1 - t\int\limits_{x=0}^{\infty} e^{-tx}\left(1 - F_{\min(G_s\,,H_{us})}(x)\right)\,dx. \tag{3.26}$$

The integral in the above equation can be efficiently solved using the numerical integration technique in MATLAB. Using the above equation, the OP in the case of MRC can be obtained as

$$\begin{aligned} P_{\text{out}}^{\text{MRC}}(\mathcal{R}) &= \mathcal{L}^{-1}\left\{\frac{M_{\gamma^{\text{MRC}}}(-t)}{t}\right\}(x=\gamma_{\text{th}}) \\ &= \mathcal{L}^{-1}\left\{\frac{1}{t}\prod_{s=1}^{S} M_{\min(G_s\,,H_{us})}(-t)\right\}(x=\gamma_{\text{th}})\,. \end{aligned} \tag{3.27}$$

The inverse Laplace transform in the above equation can be efficiently solved at $x = \gamma_{\text{th}}$ using the numerical technique presented in [108] as

$$P_{\text{out}}^{\text{MRC}}(\mathcal{R}) = \frac{2^{-Q}\,e^{D/2}}{x}\sum_{q=0}^{Q}\binom{Q}{q}\sum_{n=0}^{N+q}\frac{(-1)^n}{\Delta_n}\Re\left\{\frac{M_{\gamma^{\text{MRC}}}\left(-\dfrac{D+2\pi jn}{2\,x}\right)}{\dfrac{D+2\pi jn}{2\,x}}\right\} + E(D,Q,N), \tag{3.28}$$

where

$$\Delta_n = \begin{cases} 2, & n=0 \\ 1, & n=1,2,\cdots,N \end{cases}$$

and

$$E(D,Q,N) = \frac{e^{-D}}{1-e^{-D}} + \frac{2^{-Q}\,e^{D/2}}{x}\sum_{q=0}^{Q}(-1)^{N+1+q}\binom{Q}{q}\Re\left\{\frac{M_{\gamma^{\text{MRC}}}\left(-\dfrac{D+2\pi j(N+q+1)}{2\,x}\right)}{\dfrac{D+2\pi j(N+q+1)}{2\,x}}\right\}.$$

and $\Re\{\cdot\}$ represents the real part. Here, D, Q, and N are constants, and their values are selected during simulation to keep the discretization and truncation errors negligible.

3.4 Asymptotic outage probability analysis

This section provides the asymptotic OP analysis under the high SNR assumption. It provides insights into the theoretical limits of performance and helps simplify complex expressions, making it easier to understand system behaviour under ideal conditions. These analyses often reveal fundamental characteristics like diversity and multiplexing gains. While low SNR analysis is essential for worst-

case scenarios, high SNR results can help design and optimize systems for efficiency and robustness in typical and favourable operating conditions. At high SNR i.e., $\eta_u, \eta_s \to \infty$, the CDF of squared shadowed-Rician channel given in 3.9 can be approximated using [109] as

$$F_{H_i}^{\infty}(x) \approx \frac{\alpha_i}{\eta_i}\, x. \tag{3.29}$$

The total transmit power of the system P_t can be written as $P_t = P_u + \sum_{s=1}^{S} P_s$. This chapter considers equal power allocation to every satellite, such that $\eta_u = \eta_s = \eta$. Hence substituting (3.29) for $F_{H_{us}}(x)$ and $F_{G_s}(x)$ in (3.12) and (3.25), the asymptotic OP for scheme-2 and scheme-3 can be derived respectively, as

$$P_{\text{out}}^{\text{SC},\infty} = \left(\frac{\gamma_{\text{th}}}{\eta} \prod_{s=1}^{S} \sqrt[S]{(\alpha_s + \alpha_{us})} \right)^{S} + \mathcal{O}\left(\frac{1}{\eta^S}\right), \tag{3.30}$$

$$P_{\text{out}}^{\text{MRC},\infty} = \left(\frac{\gamma_{\text{th}} \prod_{s=1}^{S} \sqrt[S]{(\alpha_s + \alpha_{us})}}{\eta \sqrt[S]{\Gamma(S+1)}} \right)^{S} + \mathcal{O}\left(\frac{1}{\eta^S}\right), \tag{3.31}$$

where $\mathcal{O}(\cdot)$ stands for higher order terms. It is worth noting that using (3.29), the asymptotic OP in the case of MRC can be derived in closed form. The OP at high SNR can be approximated as

$$P_{\text{out}}^{\infty} = (\mathcal{G}_c \eta)^{-d} + \mathcal{O}(\eta^{-d}), \tag{3.32}$$

where $\mathcal{G}_c$ and d denote the coding gain and the diversity order, respectively. Hence, by comparing (3.30), (3.31) and (3.32), the diversity order of the system for both scheme-2 and scheme-3 can be seen as S. Moreover, the respective coding gains are

$$\mathcal{G}_c^{\text{SC}} = \left(\gamma_{\text{th}} \prod_{s=1}^{S} \sqrt[S]{(\alpha_s + \alpha_{us})} \right)^{-1}, \tag{3.33}$$

$$\mathcal{G}_c^{\text{MRC}} = \sqrt[S]{\Gamma(S+1)} \left(\gamma_{\text{th}} \prod_{s=1}^{S} \sqrt[S]{(\alpha_s + \alpha_{us})} \right)^{-1}. \tag{3.34}$$

3.5 Simulation results

This section presents simulation results to validate the derived analytical results of this work and to develop several important insights into the system performance. For simulation purposes in MATLAB, we consider the following four possible shadowing conditions for all three schemes:

(a) H-H: each h_{us} and g_s under heavy shadowing (H)

(b) H-A: each h_{us} under heavy shadowing (H) and each g_s under average shadowing (A)

(c) A-H: each h_{us} under average shadowing (A), each g_s under heavy shadowing (H)

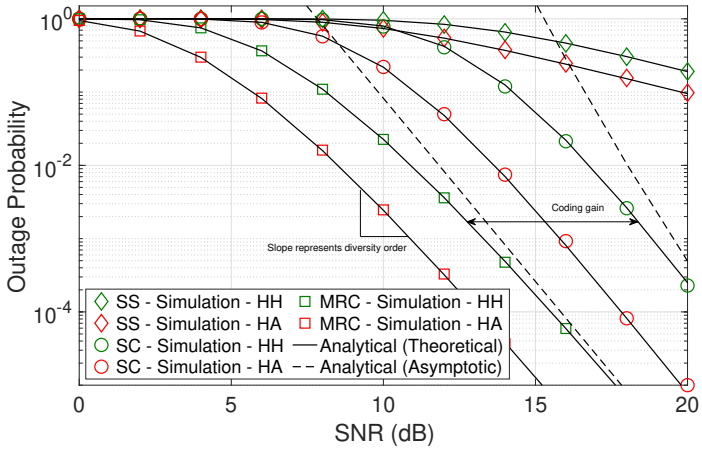

Figure 3.3 OP versus SNR curves for all three schemes under H-H and H-A conditions using $\gamma_{\text{th}} = 1, M = 50, L = 15 \times \gamma_{\text{th}}$, and $S = 5$.

(d) A-A: each h_{us} and g_s under average shadowing (A)

The SR fading parameters (m, b, Ω) under heavy and average shadowing conditions are considered to be $(2, 0.063, 0.0005)$ and $(5, 0.251, 0.279)$, respectively [110]. We set the target rate $R = 0.5$ so that $\gamma_{\text{th}} = 1$ [104]. For step-staircase approximation, we set $M = 50$ and $L = 15\gamma_{\text{th}}$. For simplicity in simulation, we consider equal power allocation with $\eta_u = \eta_s = \eta$ as the transmit SNR.

Further, to be able to identify the range of SNR values which are feasible for the proposed IoT network, we performed the link budget analysis as given in [111]. For the link budget, we consider a LEO satellite at an altitude of 800 km, an uplink central frequency of 950 MHz, satellite elevation angle of 30°, 3GPP Class 3 IoT user transmit EIRP of 23 dBm [112], and sub-carrier bandwidths of 3.7 kHz, 15 kHz, 45 kHz, 90 kHz and 180 kHz. For LEO satellite receiver antenna gain-to-noise-temperature (G/T) varying from -25 dBi/K to -6 dBi/K, SNR in the approximate range of -9 dB to 20 dB are found feasible for our network. Thus, this SNR range is considered for simulations under all four possible channel conditions.

Figure 3.3 shows the outage performance of the system against SNR by considering five LEO satellites in LoS. This figure considers shadowing conditions (a) and (b). It can be observed that the simulated curves match the analytically derived expressions. The asymptotic curves approach the exact analytical curves sharply, thus validating the correctness of the derived formulae. We are using AF relaying where the signal is amplified without decoding as opposed to DF where the effect of shadowing can be un-done by decoding at the relay. As a result, the effect of user-satellite link shadowing is clearly visible in the performance. In this figure, the user-satellite link is under heavy shadowing; consequently, the OP is significantly high for SNR less than 0 dB. Hence, the OP curves are plotted for SNR ranging from 0 dB to 20 dB in this figure to validate our closed-form expressions. It can be seen that the MRC and SC schemes outperform the SS schemes. This proves the superiority of the proposed architecture and

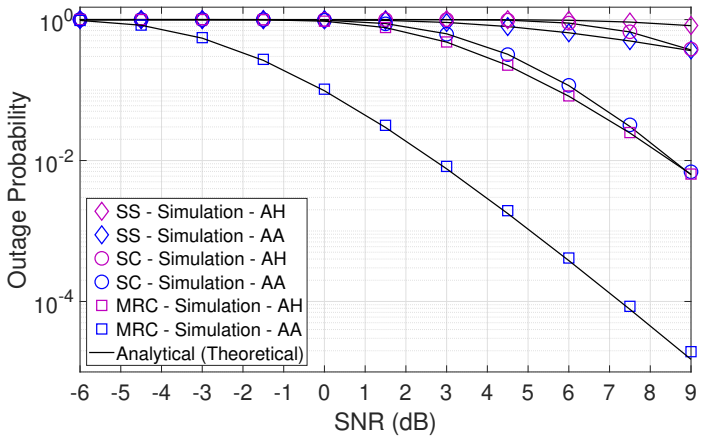

Figure 3.4 OP versus SNR curves for all three schemes under A-H and A-A conditions using $\gamma_{\text{th}} = 1, M = 50, L = 15 \times \gamma_{\text{th}}$, and $S = 5$.

establishes how it is able to leverage the benefits of multiple satellites available as part of mega LEO constellations.

One can also observe that the MRC performs significantly better than the SC. Approximately 6 dB higher SNR is required in case of the SC when compared to the MRC, for an OP of 10^{-2}. Another key observation is that, in the case of SC, approximately 3 dB higher SNR is required when the satellite-GS channel changes from average to heavy. In contrast, the difference in the required SNR is lesser in the case of MRC when the channel changes from average to heavy. Therefore, MRC proves to be much more robust towards change in shadowing conditions of satellite-GS channel. It is also observed that the slope of OP curves for SC and MRC are similar towards higher SNR. This is indicative of the fact that diversity order depends on the number of satellites in LoS. The derived diversity order and the coding gain can also be evidenced numerically from Figure 3.3. For example, in the case of MRC under the H-H shadowing condition, the OP values at 14 dB and 16 dB SNR are approximately 5×10^{-4} and 6×10^{-5}, respectively. Hence, the diversity order represented by the slope $(\Delta \log(P_{\text{out}})/\Delta\eta)$ can be approximated to the number of satellites in LoS i.e. $S = 5$. Similarly, the SNRs required to achieve an OP of 10^{-3} for MRC and SC under the H-H shadowing condition are 14 dB and 18 dB, respectively. Hence, the coding gain between MRC and SC ($\sqrt[S]{\Gamma(S+1)}$) can be approximated by the horizontal shift (4 dB) between the two curves for $S = 5$.

Figure 3.4 shows the outage performance for shadowing conditions (c) and (d). Here, the user-satellite channel is considered to be under average shadowing. Consequently, as the result of AF relaying, the OP is significantly low for SNR greater than 9 dB. Hence, OP curves are plotted for SNR ranging from -6 dB to 9 dB in this figure to validate our closed-form expressions. Observations similar to Figure 3.3 can be made regarding the better performance of the MRC when compared to the SC. Although the MRC still proves to be more robust than the SC towards change in satellite-GS link shadowing conditions, the difference in SNR is much higher compared to Figure 3.3.

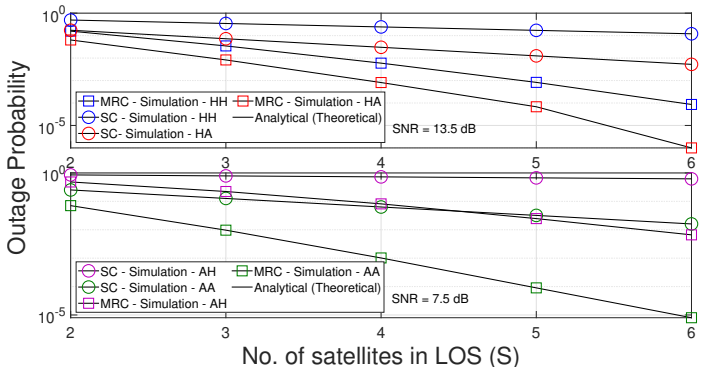

Figure 3.5 OP versus number of satellites in LoS (S) for scheme-2 and scheme-3 using $\gamma_{\text{th}} = 1, M = 50, L = 15 \times \gamma_{\text{th}}$ and $\eta = 13.5$ dB for H-A, H-H conditions and $\eta = 7.5$ dB for A-H, A-A conditions.

To gain more insights about the architecture, we also plot the OP versus the number of satellites (S) in Figure 3.5. A comparison between three famous commercial LEO constellations (SpaceX-Starlink, OneWeb, Telesat) in terms of the possible number of satellites in LoS is given in [5]. According to that, for latitudes where the majority of the world's population is located, 2 to 30 LEO satellites can be in LoS based on the location of user equipment. Hence we simulate for S in the range of 2 to 6. It can be seen from the plot that the system performance can be significantly enhanced by increasing S. This means that the performance of the proposed architecture would increase as and when new constellations or satellites are added to the network. It is also observed that the system utilizing the MRC benefits more when compared to the SC with an increased number of satellites under all channel conditions.

3.6 Summary

This chapter presented the performance analysis of a novel architecture for satellite-IoT networks. It is found that both the SC and the MRC schemes have the same diversity gain but different coding gains. This makes the MRC scheme perform better than the SC scheme. It is demonstrated that the OP reduces sharply as the number of satellites is increased within the possible limits for latitudes where the majority of the world's population resides. The proposed topology suits the era of the burgeoning number of LEO satellite constellations and cleverly uses all the available satellite resources. The analysis can further be enhanced by incorporating aspects like distance between the IoT users and satellite terminals and the effect of interference from nearby satellites and other radio users.

Chapter 4

Performance Analysis of LEO Satellite-Based IoT Networks in the Presence of Interference

This chapter provides a comprehensive analysis of the topology proposed in the previous chapter. It begins with a literature survey that explores various performance analyses conducted on relay-based systems using AF and DF schemes, as well as systems incorporating stochastic geometry, capture and SIC decoding schemes. The chapter then discusses how the performance analysis presented here differs from the existing studies on terrestrial systems. Furthermore, the chapter conducts OP analyses for a generalized system model that incorporates interference from other users and accounts for imperfect CSI. Stochastic geometry is employed to model the random locations of satellites, making the analysis general and independent of any specific constellation. The chapter also presents simplified expressions for the OP under a high SNR assumption, which is next utilized to optimize the system parameters for achieving a target OP. Towards the end, simulation results are presented to provide insights into the impact of various system parameters, such as mask angle, altitude, number of satellites, and decoding order. By encompassing these analyses, this chapter aims to demonstrate how the proposed topology can effectively leverage the benefits of multiple satellites to achieve the desired OP and enable burst transmissions without coordination among IoT users, making it an attractive choice for satellite-based IoT networks.

4.1 Background

In a star-of-star topology, the access between the node and the relay can be direct or indirect, where the satellites can act as a relay/repeater between the node and the server. However, direct-to-satellite IoT (DtS-IoT) has recently gained traction because of its ease of deployment [69]. In [90], it is shown that LPWAN technologies can be configured for realising DtS-IoT communication. Moreover, some manufacturers' low-cost, battery-powered development kits have also impeded DtS-IoT using LEO satellites [70, 72, 113]. The feasibility of DtS-IoT has been established by the link budget analysis carried out on IoT users of various power classes by different companies in a recent 3GPP study item [6].

In DtS-IoT, the satellites can act as DF or AF relays. In [114], the performance of a DF relaying network with randomly distributed interferers is analyzed under Rayleigh and Nakagami-m fading

channels. In Publication [P5], the performance of selective-DF relaying for DtS-IoT network has been analysed for LEO satellites. But, the complexity of AF relaying with a fixed gain is less than DF relaying [74], and has been preferred in [6]. The performance of topologies employing AF relaying has been widely studied for various systems. For example, in [115], the performance of a hybrid satellite-terrestrial cooperative network consisting of a single AF relay has been analyzed for generalized fading. In [116], [117], [118], and [119], the performance of an AF system with multiple relays and MRC at the destination has been analysed for Rayleigh, Nakagami-*m*, Rician, and shadowed-Rician faded channels, respectively. Additionally, co-channel interference has been included in the performance analysis of relay-based topologies in [120], and [121] for Rayleigh and mixed-Rayleigh-Rician fading channels, respectively. However, this interference can be mitigated using various cancellation techniques. In this context, several interference mitigation techniques for both relay and non-relay systems have also been discussed in the literature. A non-orthogonal multiple access (NOMA) inspired system with a single AF relay and a decoding scheme using the signal from two consecutive time slots is analysed in [122]. Similarly, a multi-source, multi-relay system with opportunistic interference cancellation using adaptive AF/DF is analysed in [123]. In both [122] and [123], performance is analysed under the Rayleigh fading assumption. In [10, 11], non-relay terrestrial IoT communication systems have been studied. A LoRaWAN like system with and without fading is considered in [10] and [11], respectively, to show that the CM and SIC-based decoding schemes can perform better than the traditional ALOHA schemes. In CM, the strongest received signal can be decoded successfully despite interference if the SINR is greater than the threshold. Whereas in SIC, decoding is performed in the order of SINRs while cancelling the interference at each step. While NOMA-based IoT network may seem attractive for satellite-based systems as it has more degrees of freedom [124, 125], it is not practical as it will require sophisticated power control algorithms and continuous communication with the ground station, which is not feasible for IoT networks with a large number of devices and limited computational and battery resources.

Recently, many mega-LEO constellations have been launched, and more are being proposed for deployment in the near future. For these, performance analysis done using satellite locations based on their orbit simulations can not be generalized for any new constellation in future. Hence, to generalize the analysis for any constellation, tools from stochastic geometry have been used in recent literature where satellites are assumed to be randomly located around the Earth [12, 13, 15, 16, 126]. In [12], coverage and throughput performance for the uplink of a satellite-based-IoT network has been presented using an empirical channel model representing path-loss and large-scale fading. In [13], a fine-grained analysis has been given for the downlink of a LEO satellites-based mmWave relay network. The satellites are assumed to be uniformly distributed on a spherical cap around the Earth, and meta-distribution of the SINR is used for performance evaluation. In [15, 16], a theoretical analysis of downlink coverage and rate in a LEO constellation is presented. The satellites are modelled as a binomial point process (BPP) on a sphere, and the users are located on the Earth's surface. Expressions for statistical characteristics of range and number of visible satellites have been derived along with the notion of an effective number of satellites to suppress the performance mismatch between the practical and random constellations.

Table 4.1 Comparison of work done in this chapter with other papers in the literature.

Scope/Reference	[10, 11]	[12, 13]	[14]	[114]	[115]	[123]	[15, 16]	[126]	This ch.
Satellite channel model		✓	✓		✓			✓	✓
Direct-access AF topology					✓	✓			✓
Multiple satellites/relays				✓		✓			✓
Interference from other users	✓	✓		✓		✓	✓		✓
Combining at the GS				✓		✓			✓
Random location of satellites		✓					✓	✓	✓
SIC decoding at GS	✓								✓
OP of end-to-end SNR/SINR	✓	✓	✓	✓		✓	✓	✓	✓
Imperfect channel estimates									✓
Asymptotic analysis on SNR			✓	✓	✓	✓			✓
Effect of system parameters		✓	✓	✓			✓	✓	✓

In [126], the performance of an LEO satellite network with ground-based gateways acting as relays has been compared with a fibre-connected network to demonstrate the coverage gain for rural and remote areas using LEO satellites. In the context of GEO satellites, [14] analyzes the performance of downlink channels for randomly located users in single and multibeam areas.

Although performance analysis of relay-based systems with and without LEO satellites have been studied in the past, there are many differences in this proposal from what has been done in the literature. In [116–119], performance analysis was done without considering any interference at the relays as opposed to this chapter. Similarly, in [120, 121], although co-channel interference was considered, only a single relay was employed, different from the multiple satellite relay architecture considered in this thesis. Neither [11] nor [10] considered a relay system with fading in the propagation environment while analyzing decoding schemes as done in this chapter. Moreover, none of the above papers specifically consider satellites as relays in their performance analysis, nor do they include any information about the location of the sources and relays. [12–16, 126], the coverage and rate analysis is limited to only single link (either uplink or downlink) performance using a single-serving satellite. Also, no mask elevation angle has been considered to define the visibility of a satellite. Table 4.1 provides a comprehensive comparison of the aspects covered in the key previous works with respect to the aspects covered in this proposal.

4.2 Stochastic geometry for satellite networks

Stochastic geometry offers a robust mathematical framework for analyzing complex spatial structures. It is extensively used in wireless networks to model the spatial distribution of nodes, such as users, base stations, ground stations, and satellites [127]. In large-scale networks, the positions of nodes are often treated as random variables. This randomness allows for the derivation of average network performance metrics, such as coverage probability and data rates, over different network configurations.

In the context of stochastic geometry, point processes are crucial tools. A point process is a random collection of points in a d-dimensional Euclidean space ($\mathbb{R}^d$). For wireless networks, these points represent the locations of nodes. The Poisson point process (PPP) and the BPP are two widely used point processes.

4.2.1 *Poisson point process (PPP)*

A PPP is characterized by its intensity measure $\Lambda(\mathcal{A})$, where $\mathcal{A}$ is a bounded subset of ($\mathbb{R}^d$). The intensity measure integrates the density function $\lambda(x)$ over the $\mathcal{A}$, i.e., $\Lambda(\mathcal{A}) = \int_{\mathcal{A}} \lambda(x)\, dx$. The number of points in any bounded region follows a Poisson distribution, and points in disjoint regions are independent. PPP is suitable for modelling networks where nodes are distributed over large or infinite areas without a fixed number of nodes.

Mathematically, the probability of finding k points in a bounded set $\mathcal{A}$ is given by

$$\mathbb{P}[N(\mathcal{A}) = k] = \frac{\Lambda(\mathcal{A})^k}{k!} e^{-\Lambda(\mathcal{A})}. \tag{4.1}$$

This property makes PPP ideal for large-scale wireless networks with an infinite number of nodes that can be considered to be distributed randomly over a vast region.

4.2.2 *Binomial Point Process (BPP)*

A BPP models a finite number of nodes within a bounded region. It is characterized by a known number of nodes n distributed over a finite area $\mathcal{W}$. The number of points in a subset $\mathcal{A}$ of $\mathcal{W}$ follows a binomial distribution such that

$$\mathbb{P}[N(\mathcal{A}) = k] = \binom{n}{k} \left(\frac{\Lambda(\mathcal{A})}{\Lambda(\mathcal{W})}\right)^k \left(1 - \frac{\Lambda(\mathcal{A})}{\Lambda(\mathcal{W})}\right)^{n-k}. \tag{4.2}$$

BPP is used for networks where the total number of nodes is fixed, making it suitable for finite satellite constellations. Stochastic geometry's application to satellite networks is an emerging field. Traditionally, the positions of satellites are deterministic, based on predefined orbits. However, due to their continuous movement, from a user's perspective, the satellites' positions can be considered random. This randomness is modelled using BPP in this thesis.

4.3 Performance analysis for terrestrial vs satellite-IoT systems

IoT and cellular users share certain characteristics regarding their communication systems. However, the author would like to emphasize that the work in this research specifically focuses on IoT networks. The performance analysis presented in the subsequent section differs from cellular networks in several important ways, as outlined below:

1. **Topology:** The energy consumption profile in IoT networks fundamentally differs from that in cellular networks. In cellular systems, significant energy is consumed in listening while in the idle state and in synchronization overhead between the user and the base station. However, since limited energy is available in IoT devices, energy consumption for such synchronization and listening in the idle state is undesired. As a result, in the proposed topology, IoT devices are proposed to wake up and transmit in burst mode and sleep without any need for synchronization. Moreover, in the proposed topology, every satellite acts as a single relay for all end devices, whereas in a cellular relay-based system, the relays are typically deployed in a hierarchical manner. These differences make it imperative that the interference from other users of the same network is considered in the mathematical analysis, which is otherwise not considered in the analysis of the cellular systems citing the use of fixed assignment protocols. Moreover, the distances between the users and the satellites are modelled as independent and identically distributed random variables to calculate the mean interference faced by every user.

2. **Communication link:** In a direct access satellite-based IoT system, the communication link between the end devices and the satellite is much longer than in a terrestrial relay-based system. This longer distance leads to higher path loss and atmospheric attenuation, which increases the outage probability of the system. Considering this factor, the benefits of multiple satellites have been leveraged to perform combining at the GS to improve end-to-end SINR and coverage probability. Performing MRC on the end-to-end SINR of a multi-user, a multi-relay system under shadowed-Rician fading is not considered in cellular systems. Cellular systems are generally modelled using Rayleigh or Nakagami fading models, making the mathematical analysis simpler than the complex mathematical formulation of the shadowed-Rician channel model used in this work.

3. **Computational capacity:** Cellular users have a high computational capacity and can run complex routing and scheduling algorithms. However, special care has been taken in our presented topology to ensure minimal computational complexity for the IoT users. That's why no power allocation is done at the IoT devices, which are assumed to transmit without synchronization. In cellular systems with sophisticated power allocation algorithms, a known decoding order in SIC can be assumed without loss of generality, thus making the mathematical analysis more straightforward. Whereas as a result of equal-power allocation in this work, ordered statistics of the end-to-end SINR is used in the mathematical analysis to perform dynamic-order decoding in SIC.

4. **Data rate and packet size:** IoT devices typically have lower data rate requirements and smaller packet sizes compared to cellular devices. This affects the OP analysis as the system design parameters like the SINR threshold and transmit power must be optimized differently.

5. **Coverage requirements:** The coverage requirements of IoT devices may differ from cellular devices. IoT devices may only require intermittent coverage for data transmission, whereas cellular

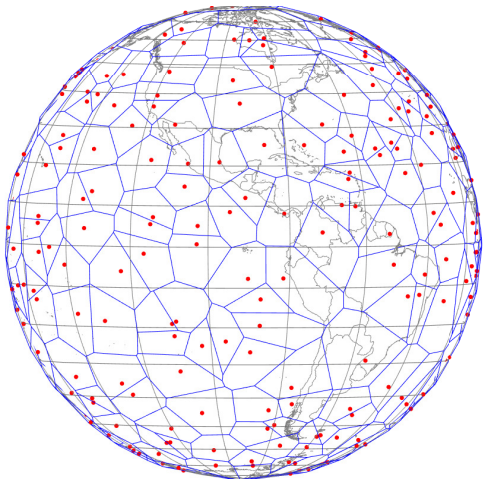

Figure 4.1 An example constellation of size $K = 720$ satellites where the satellites are distributed on a spherical surface following a BPP. The Voronoi diagrams represent the area to which the enclosed satellite is the nearest.

applications typically require continuous coverage. This affects the outage probability analysis as the system may be designed to operate in a bursty mode where the IoT devices only transmit data at specific intervals. Considering this factor, ALOHA, a simple random assignment protocol, is adopted instead of fixed assignment protocols used in cellular systems.

4.4 System description

As shown in Figure 4.1, a total of K satellites are assumed to be distributed uniformly around the Earth at an altitude d km such that they form a BPP on a sphere of radius $r_e + d$, where r_e is the radius of the Earth. The users are assumed to be located on the Earth's surface. A satellite is considered visible and can receive a signal from a user only if its elevation angle θ_e w.r.t user's location is greater than a minimum elevation or mask angle θ_0—any satellite for which $\theta_e < \theta_0$ is considered invisible to the user. The distance between a user and a satellite will be minimum when the satellite is at maximum elevation $\theta_e = 90^\circ$ w.r.t the user. This minimum distance r_{min} equals the altitude d at which all the satellites in the constellation are deployed. Similarly, the distance between a user and a satellite is maximum when the satellite is at an elevation angle $\theta_e = \theta_0$ w.r.t to the user. The maximum distance for a fixed θ_0 can be derived as shown in Section 4.5.

As shown in Figure 4.2, a direct access topology based on a mega-LEO constellation is explored, where U IoT users communicate their sensed information to a GS via S satellites among all the K_{vis} visible-satellites. The IoT users are assumed to broadcast their information simultaneously using shared resources at the start of every slot as per the slotted-ALOHA scheme similar to the case shown in [128]. Keeping in mind the low complexity of IoT users and design for a common application, it is assumed that all the users transmit at equal power. The visible satellites amplify and re-transmit the received

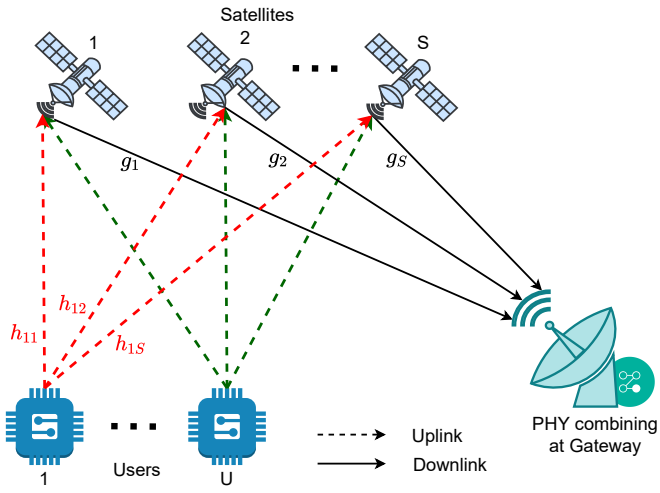

Figure 4.2 Schematic diagram of the proposed topology with U IoT users broadcasting their sensed information to S visible satellites simultaneously (different colours are used to indicate transmissions from each user). All the satellites forward the signals to the GS using fixed-gain AF relaying.

information to the GS. The GS decodes the information of all the users after coherently combining the signals received from all satellites. Thus, end-to-end communication takes place in two phases. In the first phase, all the IoT users who have sensed information broadcast their signal to all the satellites in the visible range. The signal received at the s^{th} satellite denoted as y_s can be written as

$$y_s = \sum_{u=1}^{U} \sqrt{P_u \mathcal{G}_u \mathcal{G}_s(\varphi_{us})(\lambda/4\pi r_{us})^{\alpha}}(\hat{h}_{us} + e_{us})x_u + n_s, \tag{4.3}$$

where P_u is the transmit power of the u^{th} IoT user, r_{us} is the distance between the u^{th} user and the s^{th} satellite, α is the path loss exponent, x_u is the unit energy information signal, λ is the wavelength of the information signal, n_s is the AWGN with zero mean and variance σ_n^2 at the satellite receiver, $\hat{h}_{us}$ is the SR distributed imperfect estimate of the channel coefficient and e_{us} is the estimation error. Similar to the approach followed in [129–132], the estimation error e is considered to be distributed as $\mathcal{CN}(0, \sigma_e^2)$ with an SNR dependent variance $\sigma_e^2 = \phi\,\eta^{-\chi}$, where ϕ and χ are deterministic constants. A perfect CSI can be obtained if $\chi \to \infty$ for $\eta > 0$. The transmit and the receive antenna gains at the user and the satellite are denoted as $\mathcal{G}_u$ and $\mathcal{G}_s(\varphi_{us})$ respectively, where φ_{us} is the angle between the u^{th} user location and the beam center w.r.t the s^{th} satellite. The LEO satellites also observe Doppler shifts, but it has not been considered here to keep the analysis simple. It is assumed that the Doppler can be compensated using known techniques [65].

In the second phase, the satellites employ AF to send the received signals to the GS using dedicated orthogonal resources without interference. This assumption considers that the downlink between the satellites and GS is resource-sufficient. Moreover, it keeps the analysis simpler and focused on the effect of uplink, which is limited by the transmit power of the IoT users. Similar to the store-and-

forward scheme adopted in [70], it is considered that satellites offload their information when they are nearest to the GS within a time range, i.e. $r_g = r_{\min}$. The S satellites among the K_{vis} visible satellites which offload their information to the GS in the defined time range are considered for MRC. The received signal from the s^{th} satellite at the GS denoted as z_s can be written as

$$z_s = \beta_{\text{AF}} \sqrt{\mathcal{G}_s \, \mathcal{G}_{\text{GS}} \left(\varphi_s\right) \left(\lambda / 4\pi r_{\min}\right)^{\alpha}} \left(\hat{g}_s + e_s\right) y_s + w_s, \tag{4.4}$$

where $\hat{g}_s$ is the estimated SR channel coefficient between the s^{th} satellite and GS, e_s is the estimation error distributed as $\mathcal{CN}(0, \sigma_{e_s}^2)$, β_{AF} is the AF gain factor and w_s is the additive white Gaussian noise with zero mean and variance σ_w^2 at the GS receiver. The transmit and the receive antenna gains at the satellite and the GS are denoted as $\mathcal{G}_s$ and $\mathcal{G}_{\text{GS}}(\varphi_s)$ where φ_s is the angle between the s^{th} satellite location and the beam centre with respect to the GS. Ideally, the channel effect between the user and the satellite is equalized by the AF gain factor [74]. In this chapter, the received signal is scaled at the satellite by a fixed-gain factor β_{AF}, which is inversely proportional to the total received power and is defined as

$$\beta_{\text{AF}} = \sqrt{\frac{P_s}{\sum\limits_{u=1}^{U} P_u \mathcal{G}_u \mathcal{G}_s(\varphi_{us}) \left(\frac{\lambda}{4\pi}\right)^{\alpha} \mathbb{E}_{r,\hat{h}} \left[r_{us}^{-\alpha} \left(|\hat{h}_{us}|^2 + \sigma_{e_{us}}^2 \right) \right] + \sigma_n^2}}. \tag{4.5}$$

where P_s is the transmit power of the s^{th} satellites, and $\mathbb{E}[\cdot]$ represents the expectation operator. The instantaneous end-to-end SINR of the information signal from the s^{th} satellite for the u^{th} user at the GS can be written as

$$\begin{aligned}
&\gamma_{us} \\
&= \frac{r_{\min}^{-\alpha} \, r_{us}^{-\alpha} \, G_s \, H_{us}}{r_{\min}^{-\alpha} \, G_s \left(\sum\limits_{\substack{i=1 \\ i \neq u}}^{U} r_{is}^{-\alpha} H_{is} + \sum\limits_{u=1}^{U} \eta_u r_{us}^{-\alpha} \sigma_{e_{us}}^2 + 1 \right) + \eta_s \sigma_{e_s}^2 \, r_{\min}^{-\alpha} \left(\sum\limits_{u=1}^{U} r_{us}^{-\alpha} \left(H_{us} + \eta_u \sigma_{e_{us}}^2 \right) + 1 \right) + \dfrac{P_s}{\beta_{\text{AF}}^2 \, \sigma_n^2}}, \\
&= \frac{r_{us}^{-\alpha} \, G_s \, H_{us}}{G_s \left(\sum\limits_{\substack{i=1 \\ i \neq u}}^{U} r_{is}^{-\alpha} H_{is} + \sum\limits_{u=1}^{U} \eta_u r_{us}^{-\alpha} \sigma_{e_{us}}^2 + 1 \right) + \eta_s \sigma_{e_s}^2 \left(\sum\limits_{u=1}^{U} r_{us}^{-\alpha} \left(H_{us} + \eta_u \sigma_{e_{us}}^2 \right) + 1 \right) + \widehat{C}},
\end{aligned} \tag{4.6}$$

where $H_{us} = \eta_u \, |\hat{h}_{us}|^2$ is the instantaneous SNR of a user-satellite link, $G_s = \eta_s \, |\hat{g}_s|^2$ is the instantaneous SNR of a satellite-GS link, $\widehat{C} = \frac{P_s}{r_{\min}^{-\alpha} \, \sigma_n^2 \, \beta_{\text{AF}}^2}$ is a deterministic constant, and

$$\eta_u = \frac{P_u}{\sigma_n^2} \left(\frac{\lambda}{4\pi} \right)^{\alpha} \mathcal{G}_u \, \mathcal{G}_s(\varphi_{us}),$$
$$\eta_s = \frac{P_s}{\sigma_w^2} \left(\frac{\lambda}{4\pi} \right)^{\alpha} \mathcal{G}_s \, \mathcal{G}_{\text{GS}}(\varphi_s).$$

Using (4.5), we can further simplify $\widehat{C}$ as

$$\widehat{C} = \frac{1}{r_{\min}^{-\alpha}} \left\{ 1 + \sum_{u=1}^{U} \left(\mathbb{E}\left[r_{us}^{-\alpha} H_{us} \right] + \eta_u \, \sigma_{e_{us}}^2 \mathbb{E}[r_{us}^{-\alpha}] \right) \right\}. \tag{4.7}$$

Since the GS combines the signals from all the visible satellites using MRC, the end-to-end SINR of the combined signal for the u^{th} user at the GS denoted as γ_u is given by

$$\gamma_u = \sum_{s=1}^{S} \gamma_{us}. \tag{4.8}$$

where γ_{us} is the instantaneous end-to-end SINR between the s^{th} satellite and the u^{th} user at the GS. In this chapter, two decoding schemes are compared to analyse the performance of the proposed topology:

- *Capture model (CM)*: The GS is assumed to perfectly decode the information of the desired user out of many interfering signals if its SINR is higher than a threshold. This type of decoding is similar to the capture effect used in LoRa [52].

- *Successive interference cancellation (SIC)*: The GS decodes the information of the intended user by successively removing the information of other users in the order of their SINRs [133]. The user with the highest SINR is decoded first, and its reconstructed signal is subtracted from the received superimposed signal to decode the remaining users. However, even after removing the interference, there may still be some residual error remaining due to noise or imperfect decoding. The user with SINR less than the threshold and subsequent users in the order are considered non-decodable and contribute to the outage.

4.5 Slant distance and the number of visible satellites

Since the satellites are considered to be distributed on a spherical surface following a BPP, the distance between a user and a satellite is random. Moreover, the number of visible satellites is also random and depends upon the mask angle θ_0 and the number of satellites in the constellation K. The mask angle, which depends on the environment (e.g., higher in urban areas due to obstructions, lower in rural areas), is crucial for determining the instance of obtaining a usable signal. It ensures communication

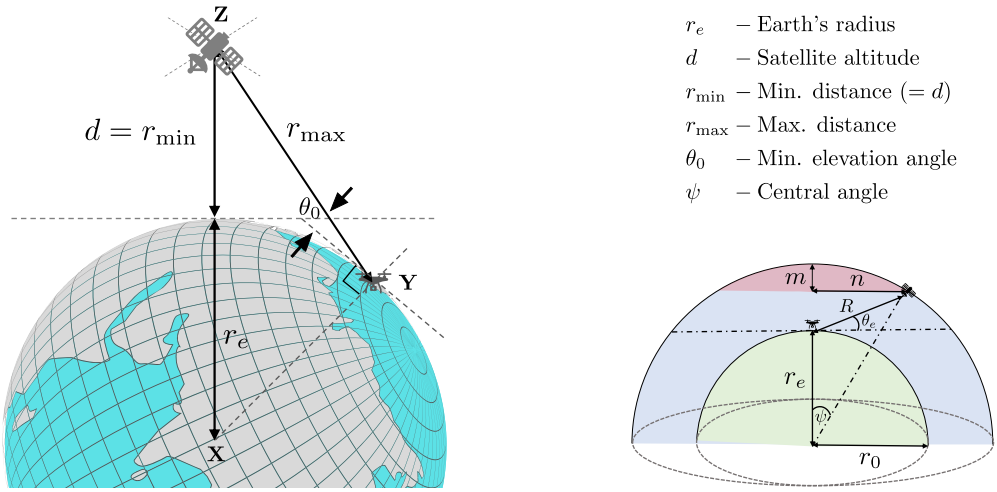

Figure 4.3 A geometric representation of the elevation angle θ_e and slant range R between a particular satellite and the IoT user being decoded at GS (maximum slant range $r_{\max}$ is obtained when $\theta_e = \theta_0$).

avoids interference from obstacles and maintains a clear line of sight, optimizing system performance. Statistical characteristics of the slant distance and number of visible satellites are derived in this section.

4.5.1 *Statistical characteristics of the distance between the user and the satellite*

The CDF $F_R(r)$ of the distance R between a user and visible satellites in the constellation is given by

$$F_R(r) = \begin{cases} 0, & r < r_{\min}, \\ \dfrac{r^2 - r_{\min}^2}{r_{\max}(\theta_0)^2 - r_{\min}^2}, & r_{\min} \le r \le r_{\max}(\theta_0), \\ & 0 \le \theta_0 < 90^\circ, \\ 1, & r > r_{\max}, \end{cases} \tag{4.9}$$

where $r_{\min} = d$ is the orbital altitude, $r_{\max}(\theta_0) = \sqrt{(r_e \sin\theta_0)^2 + (r_e + r_{\min})^2 - r_e^2} - r_e \sin\theta_0$ is the maximum distance observed at mask elevation angle θ_0 and, r_e is the radius of the Earth. The corresponding PDF $f_R(r)$ is given by

$$f_R(r) = \begin{cases} \dfrac{2\,r}{r_{\max}(\theta_0)^2 - r_{\min}^2}, & r_{\min} \le r \le r_{\max}(\theta_0), \\ & 0 \le \theta_0 < 90^\circ, \\ 0, & \text{otherwise}. \end{cases} \tag{4.10}$$

Proof: The distribution of R can be found in three steps:

1. Finding r_{min}, r_{max} and the relationship between R and the surface area of the spherical cap, A_{cap} formed by the satellites at a distance less than or equal to R
2. Finding the distribution of A_{cap}
3. Finding the distribution of R from the distribution of A_{cap}

Step 1: From basic geometry as as shown in Figure 4.3, $r_{\text{min}} = d$ is the orbital altitude, observed at $\theta_e = 90°$. Also, $r_{\text{max}}(\theta_0)$ will be observed at the mask elevation angle θ_0. Hereafter it is written as simply r_{max} to maintain brevity. Applying law-of-cosines for triangles at $\angle XYZ$ gives,

$$(r_e + r_{\text{min}})^2 = r_e^2 + r_{\text{max}}^2 - 2\, r_e\, r_{\text{max}} \cos{(90 + \theta_0)}. \tag{4.11}$$

Solving the quadratic equation (4.11) for r_{max} and considering all the distances to be positive, we get

$$r_{\text{max}} = \sqrt{(r_e \sin\theta_0)^2 + (r_e + r_{\text{min}})^2 - r_e^2} - r_e \sin\theta_0 \tag{4.12}$$

Further derivation to find the relationship between A_{cap} and R can be done on similar lines of [15]. From Figure 4.3 where m and n are shown, we can write

$$A_{\text{cap}} = \pi\,(m^2 + n^2), \tag{4.13}$$

$$R^2 = (r_{\text{min}} - m)^2 + n^2 \tag{4.14}$$

Using (4.13) and (4.14), we can obtain

$$R^2 = r_{\text{min}}^2 - 2\, r_{\text{min}}\,(r_e + r_{\text{min}})(1 - \cos\psi) + \frac{A_{\text{cap}}}{\pi}. \tag{4.15}$$

Using the geometric identity for the surface area of any spherical cap, we can write $A_{\text{cap}} = 2\pi\,(r_e + r_{\text{min}})^2\,(1 - \cos\psi)$. Substituting A_{cap} in (4.15), we get

$$R^2 = r_{\text{min}}^2 + \frac{A_{\text{cap}}}{\pi}\left(1 - \frac{r_{\text{min}}}{r_e + r_{\text{min}}}\right) \tag{4.16}$$

Similarly, at $\theta_e = \theta_0$, a spherical cap of surface area A_{vis} is formed by all the visible satellites at a distance less than or equal to maximum distance r_{max} from the user. Hence similar to (4.16), for $R = r_{\text{max}}$, we can write

$$r_{\text{max}}^2 = r_{\text{min}}^2 + \frac{A_{\text{vis}}}{\pi}\left(1 - \frac{r_{\text{min}}}{r_e + r_{\text{min}}}\right). \tag{4.17}$$

or

$$A_{\text{vis}} = \frac{\pi}{r_e}\,(r_{\text{max}}^2 - r_{\text{min}}^2)\,(r_e + r_{\text{min}}). \tag{4.18}$$

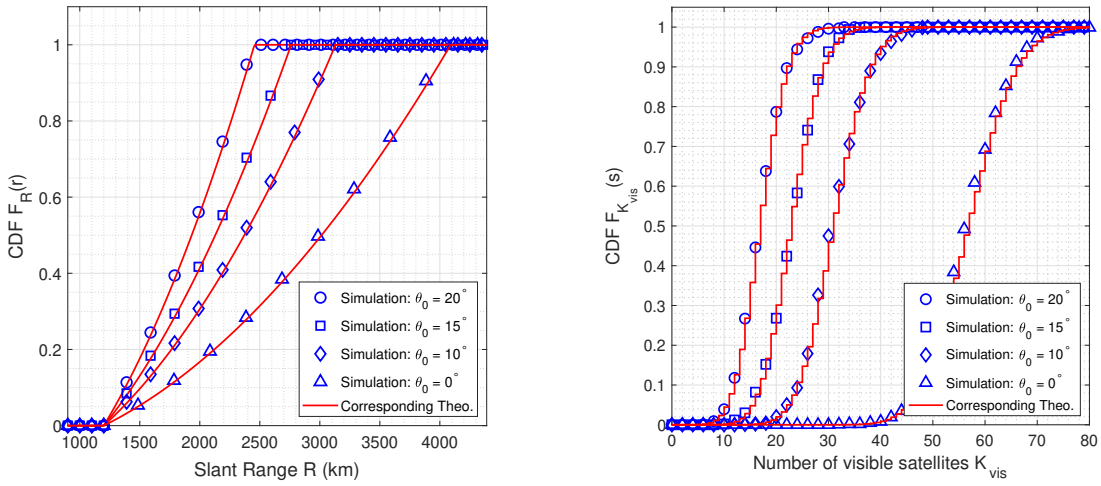

(a) (b)

Figure 4.4 (a) CDF $F_R(r)$ of the distance between a user and a visible satellite in the constellation at 1200 km altitude. (b) CDF $F_{K_{\text{vis}}}(s)$ of the number of satellites visible to any user in a constellation of 720 satellites at 1200 km altitude.

Step 2: From Figure 4.3, the CDF of the surface area of the spherical cap formed by satellites at a random distance less than or equal to R from a user is

$$F_{A_{\text{cap}}}(x) = \frac{x}{A_{\text{vis}}}. \tag{4.19}$$

Step 3: Using the relationship between A_{cap} and R as derived in (4.16), the CDF of the distance $F_R(r)$ can be written as

$$\begin{aligned} F_R(r) &= \mathbb{P}(R \leq r) = \mathbb{P}(R^2 \leq r^2) \\ &= \mathbb{P}\left(r_{\text{min}}^2 + \frac{A_{\text{cap}}}{\pi}\left(1 - \frac{r_{\text{min}}}{r_e + r_{\text{min}}}\right) \leq r^2\right) \\ &= \mathbb{P}\left(A_{\text{cap}} \leq \frac{\pi\left(r^2 - r_{\text{min}}^2\right)}{1 - \frac{r_{\text{min}}}{r_e + r_{\text{min}}}}\right) \\ &= \frac{\pi\left(r^2 - r_{\text{min}}^2\right)}{A_{\text{vis}}\left(1 - \frac{r_{\text{min}}}{r_e + r_{\text{min}}}\right)}. \end{aligned} \tag{4.20}$$

Using (4.18) in (4.20), we can write

$$F_R(r) = \frac{r^2 - r_{\text{min}}^2}{r_{\text{max}}^2 - r_{\text{min}}^2}, \text{ for } r_{\text{min}} \leq r \leq r_{\text{max}} \tag{4.21}$$

where the r_{max} is given by (4.12). The corresponding PDF can be found by differentiating (4.21) with respect to r to obtain (4.10).

The effect of θ_0 on the range can be inferred from Figure 4.4(a). It can be observed that the derived expressions match the simulation results. The slant range for which the CDF reaches 1 corresponds to the maximum possible range for a user. As the mask angle increases, the maximum possible range decreases. However, it can be observed that the maximum range decreases rapidly with an increase in the mask angle from 0° to 10° when compared to 10° to 20°. It can be attributed to the fact that r_{max} changes non-linearly with change in θ_0 as shown in (4.12).

Remark: For the special case of $\theta_0 = 0^\circ$, $r_{\text{max}}(0^\circ) = \sqrt{r_{\text{min}}^2 + 2r_e r_{\text{min}}}$. Hence for $r_{\text{min}} \leq r \leq r_{\text{max}}(0^\circ)$, (4.9) and (4.10) can be simplified as

$$F_{R_0}(r) = \frac{r^2 - r_{\text{min}}^2}{2\, r_e\, r_{\text{min}}} \tag{4.22}$$

$$f_{R_0}(r) = \frac{r}{r_e\, r_{\text{min}}} \tag{4.23}$$

where R_0 denotes the random variable for R at $\theta_0 = 0^\circ$. The expressions in (4.22) and (4.23) match with the expressions given for the characteristics of the distance in [13], where they are derived for $\theta_0 = 0^\circ$ only. The simplified expressions above are used for scenarios where high-rise structures like mountains and buildings do not mask satellite visibility.

4.5.2 *Statistical characteristics of the number of visible satellites*

A satellite is visible to a user only if its elevation angle exceeds the minimum required elevation θ_0, also called the mask angle. For a given mask elevation angle θ_0, the number of visible satellites K_{vis} to any user is a binomial random variable with success probability $\mathcal{P}$. The success probability is given by the ratio of the surface area of the spherical cap region where a visible satellite can lie to the total surface area of the sphere. It can be written as

$$\mathcal{P} = \frac{A_{\text{vis}}}{4\pi\,(r_e + r_{\text{min}})^2} \tag{4.24}$$

Using (4.18) in (4.24), we can write

$$\begin{aligned} \mathcal{P} &= \frac{\pi(r_{\text{max}}^2 - r_{\text{min}}^2)(r_e + r_{\text{min}})}{4\pi\, r_e\,(r_e + r_{\text{min}})^2} \\ &= \frac{r_{\text{max}}^2 - r_{\text{min}}^2}{4\, r_e\,(r_e + r_{\text{min}})} \end{aligned} \tag{4.25}$$

where r_{max} is the distance observed at θ_0. The effect of mask angle on the number of visible satellites can be inferred from Figure 4.4(b). It can be observed that the derived expressions match the simulation results. The number of visible satellites for which CDF equals 1 denotes the maximum possible number of satellites which can be visible to a user. As the mask angle increases, the surface area of the cap region shown in Figure 4.3 decreases, and so does the maximum number of visible satellites. It can be

observed that the maximum possible number of visible satellites decreases rapidly from 0° to 10° when compared to 10° to 20°. It can be understood using (4.12) and (4.18), since A_{vis} decreases non-linearly with an increase in θ_e.

Remark: With $\mathcal{P}_0$ denoting the success probability for the special case of $\theta_0 = 0^\circ$, (4.25) can be simplified as

$$\mathcal{P}_0 = \frac{r_{\min}}{2\left(r_e + r_{\min}\right)}. \tag{4.26}$$

4.6 Outage probability analysis

The outage probability of a particular user is defined as

$$\begin{aligned} P_{\text{out}}(\mathcal{R}) &\triangleq \mathbb{P}\left[\frac{B}{2}\log_2(1+\text{SINR}) \leq \mathcal{R}\right] \\ &= \mathbb{P}\left[\text{SINR} \leq \gamma_{\text{th}}\right], \end{aligned} \tag{4.27}$$

where $\mathcal{R}$ is the target rate, B is the bandwidth, $\gamma_{\text{th}} \triangleq 2^{2\mathcal{R}/B} - 1$ is the threshold, $\mathbb{P}[\cdot]$ represents the probability of the event and SINR needs to be calculated for CM and SIC schemes separately.

4.6.1 *OP for CM-based decoding*

In CM based decoding, the desired signal is decoded in the presence of interference from all other users. Hence the OP of a user at the GS can be written as

$$\begin{aligned} P_{\text{out}}(\mathcal{R}) &= \left(\mathbb{P}\left[\gamma_u \leq \gamma_{\text{th}}\right] \times \mathbb{P}[K_{\text{vis}} \geq S]\right) + \mathbb{P}[K_{\text{vis}} < S] \\ &= \left(F_{\gamma_u}(\gamma_{\text{th}}) \times \mathbb{P}[K_{\text{vis}} \geq S]\right) + \mathbb{P}[K_{\text{vis}} < S], \end{aligned} \tag{4.28}$$

where $\gamma_u = \sum_{s=1}^{S} \gamma_{us}$ and $\mathbb{P}[K_{\text{vis}} \geq S] = 1 - \sum_{j=0}^{S-1} \binom{K}{j} \mathcal{P}^j \left(1-\mathcal{P}\right)^{K-j}$. The following three-step approach has been followed to find the exact expression for (4.28).

1. Finding the CDF of γ_{us} conditioned on r_{us} for a single satellite scenario.
2. Finding the moment generating function (MGF) of γ_{us} and γ_u for extending the analysis to the multi-satellite scenario.
3. Finding the CDF of γ_u and consequently the OP in multi-satellite scenario.

Step 1: Using the theorem of transformation of random variables, the CDF of γ_{us} conditioned on the distance between the user and the satellite can be found as

$$F_{\gamma_{us}\,|\,r_{us}}(x) = \mathbb{P}[\gamma_{us} \le x \,|\, r_{us}] \overset{\text{(i)}}{\approx} \mathbb{P}\left[\frac{r_{us}^{-\alpha}\, G_s\, H_{us}}{G_s\,\left((U-1)\bar{I} + U\,\overline{E}_1 + 1\right) + \overline{E}_2 + \widehat{C}} \le x \,\middle|\, r_{us}\right]$$
$$\overset{\text{(ii)}}{=} \int_{g=0}^{\infty} F_{H_{us}}\left(\frac{x\,a}{r_{us}^{-\alpha}} + \frac{x\,C}{r_{us}^{-\alpha}\,g}\right)\, f_{G_s}(g)\; dg, \tag{4.29}$$

where $f_{G_s}(g)$ is the PDF of G_s. Also, in (i), interference for a user and error terms due to CSI mismatch are approximated as $\bar{I} = \mathbb{E}[r_{is}^{-\alpha}\, H_{is}]$, $\overline{E}_1 = \eta_u\, \sigma_{e_{us}}^2\, \mathbb{E}[r_{is}^{-\alpha}]$ and $\overline{E}_2 = \eta_s\, \sigma_{e_s}^2\, U\,(\bar{I} + \overline{E}_1)$ for mathematical tractability and in (ii), $a = (U-1)\,\bar{I} + U\overline{E}_1 + 1$ and $C = \overline{E}_2 + \widehat{C}$ for convenience. Since H_{us} and R_{us} are independent, $\mathbb{E}\left[r_{us}^{-\alpha}\, H_{us}\right]$ can be written as $\mathbb{E}[r_{us}^{-\alpha}\, H_{us}] = \mathbb{E}[r_{us}^{-\alpha}]\,\mathbb{E}[H_{us}]$. Using (3.8) and (4.10), $\mathbb{E}[r_{us}^{-\alpha}]$ and $\mathbb{E}[H_{us}]$ can be solved as

$$\mathbb{E}[r_{us}^{-\alpha}] = \int_{r_{\min}}^{r_{\max}} r_{us}^{-\alpha}\, f_R(r_{us})\, dr_{us} = \begin{cases} \dfrac{2\,(r_{\max}^{2-\alpha} - r_{\min}^{2-\alpha})}{(2-\alpha)(r_{\max}^2 - r_{\min}^2)} & \text{for } \alpha \neq 2, \\ \dfrac{2}{r_{\max}^2 - r_{\min}^2} \ln\left(\dfrac{r_{\max}}{r_{\min}}\right) & \text{for } \alpha = 2, \end{cases} \tag{4.30}$$

$$\mathbb{E}[H_{us}] = \int_{0}^{\infty} h_{us}\, f_{H_i}(h_{us})\, dh_{us} = \sum_{\kappa=0}^{m_i-1} \frac{\alpha_i\, \zeta(\kappa)\, \eta_i\, \Gamma(\kappa+2)}{(\beta_i - \delta_i)^{\kappa+2}}. \tag{4.31}$$

Using (3.8), (3.9), with the knowledge of binomial expansion and interchanging the order of summation and integration, (4.29) can be simplified as

$$F_{\gamma_{us}\,|\,r_{us}}(x) = 1 - \sum_{k_1=0}^{m_{us}-1} \sum_{p=0}^{k_1} \alpha_{us}\, \frac{k_1!\,\zeta(k_1)}{p!\,\eta_{us}^{k_1+1}} A_1^{-(k_1+1-p)} \sum_{k_2=0}^{m_s-1} \alpha_s \frac{\zeta(k_2)}{\eta_s^{k_2+1}} \sum_{z=0}^{p} \binom{p}{z} \left(\frac{x\,a}{r_{us}^{-\alpha}}\right)^{p-z} \left(\frac{x\,C}{r_{us}^{-\alpha}}\right)^{z}$$
$$\times \exp\left[-A_1\left(\frac{x\,a}{r_{us}^{-\alpha}}\right)\right] \int_{g=0}^{\infty} g^{-z+k_2}\, \exp\left[-A_1\left(\frac{x\,C}{r_{us}^{-\alpha}\,g}\right) - A_2\, g\right]\, dg \tag{4.32}$$

where $A_1 = \frac{\beta_{us}-\delta_{us}}{\eta_{us}}$ for uplink and $A_2 = \frac{\beta_s-\delta_s}{\eta_s}$ for downlink. The integral expression in (4.32) can be solved using [105, Eq. 3.471.9] to get the closed-form expression for $F_{\gamma_{us}\,|\,r_{us}}(x)$ as

$$F_{\gamma_{us}\,|\,r_{us}}(x) = 1 - \sum_{k_1=0}^{m_{us}-1} \sum_{p=0}^{k_1} \alpha_{us}\, \frac{k_1!\,\zeta(k_1)}{p!\,\eta_{us}^{k_1+1}} A_1^{-(k_1+1-p)} \sum_{k_2=0}^{m_s-1} \alpha_s \frac{\zeta(k_2)}{\eta_s^{k_2+1}} \sum_{z=0}^{p} \binom{p}{z} \left(\frac{x\,a}{r_{us}^{-\alpha}}\right)^{p-z} \left(\frac{x\,C}{r_{us}^{-\alpha}}\right)^{z}$$
$$\times \exp\left[-A_1\left(\frac{x\,a}{r_{us}^{-\alpha}}\right)\right]\; 2\left(\frac{A_1\,x\,C}{A_2\,r_{us}^{-\alpha}}\right)^{(1-z+k_2)/2} K_{1-z+k_2}\left(2\sqrt{\frac{A_1 A_2\,x\,C}{r_{us}^{-\alpha}}}\right), \tag{4.33}$$

where $K_v(\cdot)$ is the v^{th} order modified Bessel function of second kind.

Step 2: For any random variable X, with MGF $M_X(t)$ and $\mathcal{L}\{\cdot\}$ denoting the Laplace transform operator, we can write

$$\begin{aligned}\mathcal{L}\{f_X(x)\} &= M_X(-t),\\ \mathcal{L}\{F_X(x)\} &= \frac{M_X(-t)}{t},\end{aligned} \tag{4.34}$$

where (4.34) follows from the integral property of Laplace transform. Therefore, flipped MGF, $M_X(-t)$ is required to obtain CDF by applying the inverse Laplace transform on (4.34). The flipped MGF (referred simply as MGF hereafter) of γ_{us} conditioned on r_{us} can be derived using the definition of the Laplace transform as

$$M_{\gamma_{us}\,|\,r_{us}}(-t) = 1 - t\int_{x=0}^{\infty} e^{-tx}\left(1 - F_{\gamma_{us}\,|\,r_{us}}(x)\right)\,dx. \tag{4.35}$$

Using (4.33) and [105, Eq. 6.643.3], the integral in (4.35) can be solved to arrive at the closed-form expression for $M_{\gamma_{us}\,|\,r_{us}}(-t)$ as

$$\begin{aligned}M_{\gamma_{us}\,|\,r_{us}}(-t) = 1 - t\sum_{k_1=0}^{m_{us}-1}\sum_{p=0}^{k_1}\alpha_{us}\,\frac{k_1!\,\zeta(k_1)}{p!\,\eta_{us}^{k_1+1}}\,A_1^{-(k_1+1-p)}\sum_{k_2=0}^{m_s-1}\alpha_s\,\frac{\zeta(k_2)}{\eta_s^{k_2+1}}\sum_{z=0}^{p}\binom{p}{z}\,(C\,r_{us}^{\alpha})^{\frac{(1+z+k_2)}{2}}\\ \times\,(a\,r_{us}^{\alpha})^{p-z}\left(\frac{A_1}{A_2}\right)^{(1-z+k_2)/2}\epsilon^{-\mu}\,\exp\left[\frac{\Lambda^2}{2\,\epsilon}\right]\,\frac{\Gamma(\mu+\nu+\frac{1}{2})\Gamma(\mu-\nu+\frac{1}{2})}{\Lambda}\,W_{-\mu,\nu}\left(\frac{\Lambda^2}{\epsilon}\right),\end{aligned} \tag{4.36}$$

where $\mu = p + 1 + \frac{k_2-z}{2}, \epsilon = A_1\,a\,r_{us}^{\alpha} + t, \Lambda = \sqrt{A_1\,A_2\,C\,r_{us}^{\alpha}}, \nu = \frac{1-z+k_2}{2}$, and $\Gamma(\cdot)$, $W_{\mu,v}(\cdot)$ are the Gamma and Whittaker functions, respectively. Subsequently, the MGF of γ_{us} can be calculated by averaging over r_{us} using (4.10) and (4.36) as

$$\begin{aligned}M_{\gamma_{us}}(-t) &= \int_{r_{\min}}^{r_{\max}} M_{\gamma_{us}\,|\,r_{us}}(-t)\,f_R(r_{us})\,dr_{us}\\ &= \frac{2}{r_{\max}^2 - r_{\min}^2}\int_{r_{\min}}^{r_{\max}} r_{us}\,M_{\gamma_{us}\,|\,r_{us}}(-t)\,dr_{us}.\end{aligned} \tag{4.37}$$

It is worth mentioning that the above averaging of the conditional MGF to obtain the unconditional MGF is valid as per the law of total expectation i.e. the expected value of the conditional expected value of a random variable given another random variable is the same as the expected value of the initial random variable itself [134]. The integral term in (4.37) can be efficiently calculated using the `vpaintegral` function of MATLAB. It uses the global adaptive quadrature technique and variable precision arithmetic to perform the integration. The speed of the execution can be traded off with the

tolerance value. Consider

$$\texttt{func} = M_{\gamma_{us}\,|\,r_{us}}(-t)\, f_R(r_{us}),$$

where $f_R(r_{us})$ and $M_{\gamma_{us}\,|\,r_{us}}(-t)$ are given in (4.10) and (4.36), respectively. Then, the integral term in (4.37) can be evaluated using

$$\texttt{vpaintegral(func, r, rMin, rMax, 'RelTol', 1e-4, 'AbsTol', 0);}$$

where $\texttt{rMin} = r_{\text{min}}$, $\texttt{rMax} = r_{\text{max}}$ and the integration is done for a relative tolerance of 10^{-4} and the option to set the absolute tolerance is turned off.

The MRC is implemented at the GS on the signal with end-to-end SINR as defined in (4.8). Since all the S satellite-GS links are independent, the MGF of the end-to-end SINR can be written as

$$M_{\gamma_u}(-t) = \prod_{s=1}^{S} M_{\gamma_{us}}(-t) \tag{4.38}$$

Step 3: The CDF of γ_u as be obtained as

$$F_{\gamma_u}(x) = \mathcal{L}^{-1}\left\{\frac{M_{\gamma_u}(-t)}{t}\right\}(x)\,. \tag{4.39}$$

The inverse Laplace transform in (4.39) can be efficiently calculated using the numerical technique presented in [108], and also elucidated in Section 3.3.3. Thus, using (4.25) and (4.39) in (4.28) completes the derivation of OP for CM-based decoding.

4.6.2 *OP for SIC-based decoding*

SIC is an ordering-based scheme where the GS decodes the information of users in the order of their end-to-end SINRs. The residual error due to imperfect interference cancellation is considered to be distributed as $\mathcal{CN}(0,\xi)$ where ξ represents the power of the residual error. For ease of understanding, $l \in [1, U]$ is used to denote the order/iteration of SIC decoding and $\mathbf{D}[\,l\,]$ is used to denote the set of indexes for all decoded users till the l^{th} iteration. Additionally, $\mathbf{D}\{l\}$ is used to denote the index of the user decoded at the l^{th} iteration. Therefore end-to-end SINR of the signal from u^{th} user received via s^{th} satellite in the l^{th} iteration of SIC decoding for all $u \notin \mathbf{D}[\,l-1\,]$ can be written as

$$\begin{aligned}\gamma_{us}^{(l)} &= \frac{r_{us}^{-\alpha}\, G_s\, H_{us}}{G_s\left(\sum\limits_{\substack{i,\, i\neq u\\ i\notin\mathbf{D}[l-1]}}^{U} r_{is}^{-\alpha} H_{is} + \sum\limits_{u=1}^{U} \eta_u r_{us}^{-\alpha}\sigma_{e_{us}}^2 + \sum\limits_{\substack{i,\, i\neq u\\ i\in\mathbf{D}[l-1]}} \eta_u \xi r_{is}^{-\alpha} + 1\right) + \eta_s\sigma_{e_s}^2\left(\sum\limits_{u=1}^{U} r_{us}^{-\alpha}\left(H_{us} + \eta_u\sigma_{e_{us}}^2\right) + 1\right) + \widehat{C}},\\ &= \frac{r_{us}^{-\alpha}\, G_s\, H_{us}}{G_s\,\left((U-l)\bar{I} + U\overline{E}_1 + (l-1)\overline{E}_3 + 1\right) + \overline{E}_2 + \widehat{C}} \quad \forall\, u \notin \mathbf{D}[\,l-1\,],\end{aligned} \tag{4.40}$$

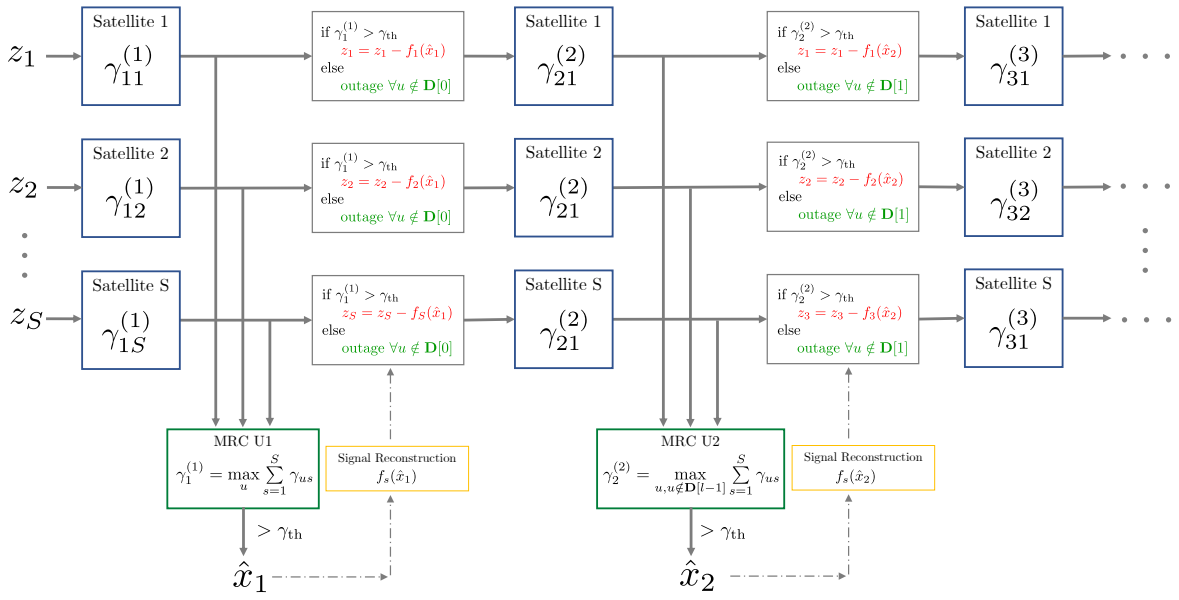

Figure 4.5 Schematic diagram explaining the steps involved in the implementation of the proposed MRC along with SIC. It is assumed that the users get decoded in sequential order $1, 2, \cdots, U$, for ease of understanding; however, the order can be dynamic as per Eqn. (4.42). The reconstruction function for interference cancellation is represented as $f_s(\cdot)$.

where $\overline{E}_3 = \eta_u \, \xi \, \mathbb{E}[r_{is}^{-\alpha}]$, and $u \notin \mathbf{D}[\, l-1\,]$ denotes the index of the users not decoded till $(l-1)^{\text{th}}$ iteration. Also, the end-to-end SINR of the MRC combined signal of the u^{th} user can be written as

$$\gamma_u^{(l)} = \sum_{s=1}^{S} \gamma_{us}^{(l)} \quad \forall \, u \notin \mathbf{D}[\, l-1\,]. \tag{4.41}$$

As shown in Figure 4.5, at every iteration, the user with the highest SINR is decoded such that

$$\gamma_{\mathbf{D}\{l\}}^{(l)} = \begin{cases} \max\limits_{u} \gamma_u^{(l)}, & l = 1 \\ \max\limits_{u, u \notin \mathbf{D}[\,l-1\,]} \gamma_u^{(l)}, & \gamma_{\mathbf{D}\{l-1\}}^{(l-1)} > \gamma_{\text{th}}, \, l > 1 \\ 0, & \text{otherwise}, \end{cases} \tag{4.42}$$

where the set of indexes for all the decoded users is updated after every iteration as

$$\mathbf{D}[\, l-1\,] = \begin{cases} \emptyset, & l = 1 \\ \mathbf{D}[\, l-2\,] \cup \{ \underset{u, u \notin \mathbf{D}[l-2]}{\arg\max} \, \gamma_u^{(l-1)} \}, & \gamma_{\mathbf{D}\{l-1\}}^{(l-1)} > \gamma_{\text{th}}, l > 1 \\ \mathbf{D}[l-2], & \gamma_{\mathbf{D}\{l-1\}}^{(l-1)} \leq \gamma_{\text{th}}, l > 1. \end{cases} \tag{4.43}$$

where $\emptyset$ denotes an empty set. Therefore the OP of l^{th} user in case of SIC can be written as

$$P_{\text{out}}^{(l)}(\mathcal{R}) = \begin{cases} \left(\mathbb{P}[\max\limits_{u} \gamma_u^{(l)} \leq \gamma_{\text{th}}]\, \mathbb{P}[K_{\text{vis}} \geq S]\right) + \mathbb{P}[K_{\text{vis}} < S], & l = 1 \\ \left\{\mathbb{P}[\gamma_{\mathbf{D}\{l\}}^{(l)} \leq \gamma_{\text{th}} \,|\, \gamma_{\mathbf{D}\{l-1\}}^{(l-1)} > \gamma_{\text{th}}]\,(1 - P_{\text{out}}^{(l-1)}(\mathcal{R})) + P_{\text{out}}^{(l-1)}(\mathcal{R})\right\} \mathbb{P}[K_{\text{vis}} \geq S] & \\ \quad + \mathbb{P}[K_{\text{vis}} < S], & l > 1, \end{cases} \tag{4.44}$$

or simply as

$$P_{\text{out}}^{(l)}(\mathcal{R}) = \left(F_{\gamma_u^{(l)}}(\gamma_{\text{th}}) \times \mathbb{P}[K_{\text{vis}} \geq S]\right) + \mathbb{P}[K_{\text{vis}} < S]. \tag{4.45}$$

The exact expression of (4.45) for $l = 1$ can be obtained. However, for $l > 1$ it is not mathematically tractable since the distribution of $\gamma_{\mathbf{D}\{l\}}^{(l)}$ conditioned on $\gamma_{\mathbf{D}\{l-1\}}^{(l-1)} > \gamma_{\text{th}}$ is difficult to obtain. Therefore, the exact expression for OP in case of SIC is obtained for the best user ($l = 1$) only, which is a lower bound on the average OP of the system and simulation results are presented for $l > 1$. For the case of $l = 1$, distribution for the maximum of dependent random variables $\gamma_u^{(1)}$ is required. Hence, the derivation is done using the following steps:

1. Finding the CDF of $\gamma_{us}^{(1)}$ conditioned on G_s for single satellite scenario.
2. Finding the MGF of $\gamma_{us}^{(1)}$ and $\gamma_u^{(1)}$ conditioned on G_s for the analysis on multi-satellite scenario.
3. Finding the CDF and consequently the OP for $\max\limits_{u} \gamma_u^{(1)}$ averaged over all G_s.

Step 1: Using the theorem of transformation of random variables, the CDF of $\gamma_{us}^{(1)}$ conditioned on G_s can be written as:

$$\begin{aligned} F_{\gamma_{us}^{(1)}|G_s} &= \mathbb{P}\left[\frac{r_{us}^{-\alpha}\, G_s\, H_{us}}{a\, G_s + C} \leq x \,\middle|\, G_s\right] \\ &= \mathbb{P}\left[r_{us}^{-\alpha}\, H_{us} \leq a\, x + \frac{C\, x}{G_s} \,\middle|\, G_s\right] \\ &= F_{\widetilde{H}_{us}|G_s}\left(a\, x + \frac{C\, x}{g_s}\right), \end{aligned} \tag{4.46}$$

where $a = \left((U-1)\bar{I} + U\overline{E}_1 + 1\right)$, $C = \overline{E}_2 + \widehat{C}$ and $\widetilde{H}_{us} = r_{us}^{-\alpha}\, H_{us}$. The CDF $F_{\widetilde{H}_{us}}(z)$ can be written as

$$\begin{aligned} F_{\widetilde{H}_{us}}(z) &= \int_{r_{\min}}^{r_{\max}} F_{H_{us}}\left(\frac{z}{r_{us}^{-\alpha}}\right) f_R(r_{us})\, dr_{us} \\ &= 1 - \frac{2\,\alpha_{us}}{r_{\max}^2 - r_{\min}^2} \sum_{k=0}^{m_{us}-1} \sum_{p=0}^{k} \frac{k!\,\zeta(k)}{p!\,\eta_{us}^{k+1}} A^{-(k+1-p)} \int_{r_{\min}}^{r_{\max}} (z\, r_{us}^{\alpha})^p \exp[-A z r_{us}^{\alpha}]\, r_{us}\, dr_{us}. \end{aligned} \tag{4.47}$$

The integral in (4.47) can be solved using [105, Eq. 3.381.8] to obtain

$$F_{\widetilde{H}_{us}}(z) = 1 - \frac{2}{r_{\max}^2 - r_{\min}^2} \sum_{k=0}^{m_{us}-1} \sum_{p=0}^{k} \alpha_{us} \frac{k!\,\zeta(k)}{p!\,\eta_{us}^{k+1}} A^{-(k+1-p)} \left(\frac{\gamma(V, \rho r_{\max}^{\alpha}) - \gamma(V, \rho r_{\min}^{\alpha})}{\alpha \rho^{V}} \right) z^{p}, \tag{4.48}$$

where $A = \frac{\beta-\delta}{\eta}$, $V = \frac{\alpha p+2}{\alpha}$, $\rho = A\,z$ and $\gamma(\cdot,\cdot)$ is the lower incomplete Gamma function.

Step 2: Similar to the approach followed in the derivation of CM decoding, the MGF of $\gamma_{us}^{(1)}$ conditioned on G_s can be written as

$$M_{\gamma_{us}^{(1)}|G_s}(-t) = 1 - t \int_{x=0}^{\infty} e^{-tx} \left(1 - F_{\widetilde{H}_{us}|G_s} \left(ax + \frac{Cx}{g_s} \right) \right) dx. \tag{4.49}$$

Rearranging the terms, (4.49) can be written as

$$M_{\gamma_{us}^{(1)}|G_s}(-t) = 1 - \frac{2\,t}{r_{\max}^2 - r_{\min}^2} \sum_{k=0}^{m_{us}-1} \sum_{p=0}^{k} \frac{\alpha_{us}}{\alpha} \frac{k!\,\zeta(k)}{p!\,\eta_{us}^{k+1}} A^{-(k-p+V+1)} \left(a + \frac{C}{g_s} \right)^{p-V}$$
$$\times \int_{x=0}^{\infty} e^{-tx}\, x^{p-V} \left\{ \gamma\left(V, A\, r_{\max}^{\alpha} \left(a + \frac{C}{g_s} \right) x \right) - \gamma\left(V, A\, r_{\min}^{\alpha} \left(a + \frac{C}{g_s} \right) x \right) \right\} dx. \tag{4.50}$$

The integral in (4.50) can be solved using [105, Eq. 6.455.2] to obtain

$$M_{\gamma_{us}^{(1)}|G_s}(-t) = 1 - \frac{2\,t}{r_{\max}^2 - r_{\min}^2} \sum_{k=0}^{m_{us}-1} \sum_{p=0}^{k} \frac{\alpha_{us}}{\alpha} \frac{k!\,\zeta(k)}{p!\,\eta_{us}^{k+1}} A^{-(k-p+V+1)} \left(a + \frac{C}{g_s} \right)^{p-V} \frac{\Gamma(p+1)}{V}$$
$$\times \left\{ \frac{[\upsilon_1(g_s)]^{V}}{[\upsilon_1(g_s)+t]^{p+1}}\, {}_2F_1\left(1, p+1; V+1; \frac{\upsilon_1(g_s)}{\upsilon_1(g_s)+t} \right) \right.$$
$$\left. - \frac{[\upsilon_2(g_s)]^{V}}{[\upsilon_2(g_s)+t]^{p+1}}\, {}_2F_1\left(1, p+1; V+1; \frac{\upsilon_2(g_s)}{\upsilon_2(g_s)+t} \right) \right\}, \tag{4.51}$$

where $\upsilon_1(g_s) = A\, r_{\max}^{\alpha} \left(a + \frac{C}{g_s} \right)$, $\upsilon_2(g_s) = A\, r_{\min}^{\alpha} \left(a + \frac{C}{g_s} \right)$ and ${}_2F_1(\cdot)$ is the Gauss hypergeometric function [105, Eq. 9.100]. Since all the S satellites-GS links are independent, the MGF of $\gamma_u^{(1)}$ conditioned on G_s can therefore be written as

$$M_{\gamma_u^{(1)}|G_s}(-t) = \prod_{s=1}^{S} M_{\gamma_{us}^{(1)}|G_s}(-t). \tag{4.52}$$

Step 3: Averaging over all the G_s, the CDF of $\max_u \gamma_u^{(1)}$ can be derived as

$$F_{\gamma_u^{(1)}}(x) = \int_{g_1} \cdots \int_{g_S} \left[\mathcal{L}^{-1} \left\{ \frac{M_{\gamma_u^{(1)}|G_s}(-t)}{t} \right\}(x) \right]^U \times \left\{ \prod_{s=1}^{S} f_{G_s}(g_s) \right\} dg_1 \cdots dg_S. \tag{4.53}$$

As explained in the previous subsection, the integral in (4.53) can be efficiently calculated numerically. Thus, using (4.25) and (4.53) in (4.45) with $l = 1$ completes the derivation of the OP in SIC decoding for best user.

4.7 Asymptotic analysis of outage probability

This section presents the asymptotic analysis to obtain simplified expressions of OP for both CM and SIC-based decoding schemes under the assumption that $\eta_u, \eta_s \to \infty$.

4.7.1 *Asymptotic OP for CM-based decoding*

The end-to-end SINR expression for the CM-based decoding as shown in (4.6) can be approximated under the assumption $\eta_u, \eta_s \to \infty$ as

$$\gamma_{us}^{\infty} \approx \frac{r_{us}^{-\alpha} H_{us}}{\sum\limits_{\substack{i=1 \\ i \neq u}}^{U} r_{is}^{-\alpha} H_{is} + \sum\limits_{u=1}^{U} \eta_u r_{us}^{-\alpha} \sigma_{e_{us}}^2 + 1}, \tag{4.54}$$

since at high SNR, the system tends to become interference-limited only. For mathematical tractability, we write $\mathcal{I} = (U-1)\,\mathbb{E}[r_{is}^{-\alpha}\,|\hat{h}_{us}|^2] + U\,\sigma_{e_{us}}^2\,\mathbb{E}[r_{us}^{-\alpha}]$ and $a = \eta_u\,\mathcal{I} + 1$. Hence γ_{us} can be written as

$$\gamma_{us}^{\infty} \approx \frac{1}{a}\, r_{us}^{-\alpha}\, H_{us}. \tag{4.55}$$

Therefore, using the theorem of transformation of random variables, the asymptotic CDF of γ_{us}^{∞} can be computed as:

$$\begin{aligned} F_{\gamma_{us}}^{\infty}(x) &= \mathbb{P}\left[\frac{1}{a}\, r_{us}^{-\alpha}\, H_{us} \leq x \right] \\ &= \int_{r_{\min}}^{r_{\max}} F_{H_{us}}\left(\frac{a\,x}{r_{us}^{-\alpha}} \right) f_R(r_{us})\, dr_{us} \\ &= F_{\widetilde{H}_{us}}(a\,x)\,, \end{aligned} \tag{4.56}$$

where $F_{\widetilde{H}_{us}}(z)$ is derived in closed form in (4.48). Using the series expansion of the lower incomplete Gamma function, $\gamma(\cdot,\cdot)$ as given in [105, Eq. 8.354.1] in the above equation, we get

$$F_{\widetilde{H}_{us}}(z) = 1 - \left\{ \sum_{(k,p,q)} \frac{(-1)^q \, 2 \, k! \, \zeta(k) \, \alpha_{us}}{p! \, q! \, (\alpha \, \bar{p} + 2) \, (\beta - \delta)^{(k+1-\bar{p})}} \left(\frac{r_{\max}^{(\alpha \, \bar{p}+2)} - r_{\min}^{(\alpha \, \bar{p}+2)}}{r_{\max}^2 - r_{\min}^2} \right) (z \, \mathcal{I})^{\bar{p}} \left(1 + \frac{\bar{p}}{\mathcal{I} \, \eta_{us}} \right) \right\} + \mathcal{O}\left(\frac{1}{\eta_{us}} \right), \tag{4.57}$$

where q is the iterator for the series expansion of $\gamma(\cdot, \cdot)$, $\bar{p} = p + q$ and $\mathcal{O}\left(\frac{1}{\eta_{us}}\right)$ represents the higher order terms of $(1/\eta_{us})$. Since $\eta_u, \eta_s \to \infty$, the (4.57) can further be simplified by neglecting the higher order terms to obtain finally

$$F_{\gamma_{us}}^{\infty}(x) = 1 - \sum_{(k,p,q)} C(k,p,q) \left(1 + \frac{\bar{p}}{\mathcal{I} \, \eta_{us}} \right) x^{\bar{p}} \tag{4.58}$$

$$M_{\gamma_{us}}^{\infty}(-t) = 1 - \sum_{(k,p,q)} C(k,p,q) \, \bar{p} \, ! \left(1 + \frac{\bar{p}}{\mathcal{I} \, \eta_{us}} \right) t^{-\bar{p}}, \tag{4.59}$$

where the quantities $C(k,p,q), \mathcal{I}$, and a are defined as

$$C(k,p,q) = \frac{(-1)^q \, 2 \, k! \, \zeta(k) \, \alpha_{us} \, \mathcal{I}^{\bar{p}}}{p! \, q! \, (\alpha \, \bar{p} + 2) \, (\beta - \delta)^{(k+1-\bar{p})}} \times \left(\frac{r_{\max}^{(\alpha \, \bar{p}+2)} - r_{\min}^{(\alpha \, \bar{p}+2)}}{r_{\max}^2 - r_{\min}^2} \right), \tag{4.60}$$

$\mathcal{I} = (U-1) \, \mathbb{E}[r_{is}^{-\alpha} \, |\hat{h}_{us}|^2] + U \, \sigma_{e_{us}}^2 \, \mathbb{E}[r_{us}^{-\alpha}], a = \eta_u \, \mathcal{I} + 1$ and $\bar{p} = p + q$. These expressions are much simpler to comprehend and do not include any integrals. It can be observed that at high SNR, the OP attains a floor. It can be attributed to the fact that at high SNR, the performance is limited by the interference and the mismatch due to imperfect CSI such that any further increase in SNR cannot decrease the OP. The asymptotic CDF $F_{\gamma_u}^{\infty}(x)$ and consequently the asymptotic OP $P_{\text{out}}^{\infty}(\mathcal{R})$ in scenarios with multiple satellites can therefore be written as

$$\begin{aligned} F_{\gamma_u}^{\infty}(x) &= \mathcal{L}^{-1} \left\{ \frac{(M_{\gamma_{us}}^{\infty}(-t))^S}{t} \right\}(x), \\ P_{\text{out}}^{\infty}(\mathcal{R}) &= \left(F_{\gamma_u}^{\infty}(\gamma_{\text{th}}) \times \mathbb{P}[K_{\text{vis}} \geq S] \right) + \mathbb{P}[K_{\text{vis}} < S]. \end{aligned} \tag{4.61}$$

The above simplified expressions can be used to obtain the optimal number of supported users and the required number of satellites with assured visibility (i.e. the number of satellites S such that $\overline{P}_{\text{vis}}(S) = 1$) for a target OP. The optimization problem can be formulated as

$$\begin{aligned} \max \quad & S \\ \text{s.t.} \quad & \overline{P}_{\text{vis}}(S) = 1, \, \theta_0 \in [0, 90], \\ & S \in [1, K], \, S \in \mathbb{Z}^+. \end{aligned}$$

As S is increased, the probability of seeing those many satellites with assured visibility decreases. Hence, in the above optimization problem, S is being maximized to get the maximum number of satellites for which the visibility is assured. Using the optimized values of satellites S^* and mask angle θ_0^*, the number of supported users can be obtained by solving

$$\begin{aligned} \max \quad & U \\ \text{s.t.} \quad & P_{\text{out}}^{\infty}(\mathcal{R}) \leq 0.001 \\ & U \geq 1,\, U \in \mathbb{Z}^+. \end{aligned}$$

The above optimization problems can be solved using a Genetic algorithm (GA), which can solve both constrained and unconstrained problems with linear, non-linear and integer constraints. However, for integer constraints, the GA can only find solutions with non-linear inequalities. Hence, the assured visibility condition can be approximated and reformulated as $0.999 - \overline{P}_{\text{vis}}(S) \leq 0$. A Genetic Algorithm (GA) is inspired by the process of natural selection. It finds optimal or near-optimal solutions by simulating the evolution of potential solutions. The GA operates on a population of candidate solutions (also represented by chromosomes or a combination of genes) and iteratively applies genetic operators such as selection, crossover, and mutation to evolve the population over successive generations. Through this process, the algorithm aims to converge towards solutions that exhibit desirable traits based on the objective function or the fitness function evaluation.

If G represents the maximum number of generations, N represents the initial size of the population, and L represents the size of the chromosome, the complexity of a genetic algorithm can be broken down into the following steps:

- **Initialization ($\mathcal{O}(NL)$):** Generating an initial population of N individuals by creating and initializing each gene within the chromosome. A *uniform* function, the MATLAB default for integer constraints, is opted in our implementation.
- **Selection ($\mathcal{O}(N)$):** Selecting individuals from the population for crossover. The MATLAB default *tournament selection* method is opted in our implementation.
- **Crossover ($\mathcal{O}(NL)$):** Combining genetic information from two parent chromosomes to create new offspring. A *Laplace crossover* function, the MATLAB default for integer constraints, is opted in our implementation.
- **Mutation ($\mathcal{O}(NL)$):** Modifying a small portion of the genetic information of individuals. The MATLAB default *Power mutation* function is opted in our implementation.
- **Fitness Evaluation ($\mathcal{O}(NL)$):** Evaluating the objective function for each chromosome.
- **Population Replacement ($\mathcal{O}(N)$):** Replacing the old population with the new one.
- **Termination ($\mathcal{O}(1)$):** Checking if the termination criteria (e.g., maximum generations reached or desired fitness achieved) are met.

Then, the overall time complexity of the GA can be approximated as the sum of the complexities of its individual steps as $\mathcal{O}(G(N + NL + NL + NL + NL + NL + N + 1))$. It can further be simplified to obtain the estimated upper bound on the time complexity of the entire GA over all iterations as $\mathcal{O}(G(N + NL))$. As shown in Section 4.8, the above-simplified expressions can be used to derive interesting insights on the optimal region of operation in terms of the number of devices, satellites, mask angle and constellation size.

Remark (diversity order): Although the OP attains a floor in scenarios with interference and imperfect CSI, the diversity order can be determined for a simpler scenario with perfect CSI and no interference from other users. When there is no interference from other users, a becomes equal to 1 in 4.55. Hence the CDF of γ_{us} under the assumption $\eta_u, \eta_s \to \infty$ can be further simplified as

$$F^{\infty}_{\gamma_{us}}(x) = \mathbb{P}\left[r_{us}^{-\alpha} H_{us} \leq x\right]. \tag{4.62}$$

However, as shown in [109], the CDF of H_{us} under the high SNR assumption can be approximated as

$$F^{\infty}_{H_{us}}(x) \approx \frac{\alpha_{us}}{\eta_{us}} x. \tag{4.63}$$

Therefore, $F^{\infty}_{\gamma_{us}}(x)$ can be simplified as

$$F^{\infty}_{\gamma_{us}}(x) = \int_{r_{\text{min}}}^{r_{\text{marx}}} \frac{\alpha_{us}}{\eta_{us}} \left(x\, r_{us}^{\alpha}\right) f_R(r)\, dr. \tag{4.64}$$

Using the PDF of R shown in (4.10) of the manuscript, the above equation can be solved as

$$F^{\infty}_{\gamma_{us}}(x) = \frac{\alpha_{us}}{\eta_{us}} R_0\, x, \tag{4.65}$$

where

$$R_0 = \frac{2}{\alpha + 2} \left(\frac{r_{\text{max}}^{(\alpha+2)} - r_{\text{min}}^{(\alpha+2)}}{r_{\text{max}}^{2} - r_{\text{min}}^{2}} \right). \tag{4.66}$$

Further, the MGF and the CDF for the multiple satellites scenario can be derived as

$$M^{\infty}_{\gamma_{us}}(-t) = \frac{\alpha_{us}}{\eta_{us}} R_0\, t^{-1}, \tag{4.67}$$

$$F^{\infty}_{\gamma_u}(x) = \mathcal{L}^{-1}\left\{ \frac{((\alpha_{us}/\eta_{us})\, R_0\, t^{-1})^S}{t} \right\}(x) = \frac{(\alpha_{us}\, R_0)^S}{\Gamma(S+1)} \left(\frac{x}{\eta_{us}} \right)^S. \tag{4.68}$$

The OP at high SNR can be approximated as

$$P^{\infty}_{\text{out}}(\mathcal{R}) = (G_c \eta_u)^{-\hat{d}} + \mathcal{O}(\eta_u^{-\hat{d}}), \tag{4.69}$$

where G_c and $\hat{d}$ denote the cooperation gain and the diversity order, respectively. The term $\mathcal{O}(\eta_u^{-\hat{d}})$ represents the higher order terms of $\eta_u^{-\hat{d}}$. Here, it is worth mentioning that the CM and the SIC schemes are synonymous with each other under the no-interference scenario. Using (4.55) with the approximation of $F_{H_{us}}(x)$ as shown in [109], and ignoring the higher order terms, the asymptotic OP under the no-interference scenario can be written as

$$P_{\text{out}}^{\infty}(\mathcal{R}) = \frac{(\alpha_{us}\, R_0\, \gamma_{\text{th}})^S}{\Gamma(S+1)} \left(\frac{1}{\eta_u}\right)^S, \tag{4.70}$$

where $R_0 = \dfrac{2}{\alpha+2}\left(\dfrac{r_{\text{max}}^{(\alpha+2)} - r_{\text{min}}^{(\alpha+2)}}{r_{\text{max}}^2 - r_{\text{min}}^2}\right)$. Hence the proposed topology achieves a diversity order of S and a cooperation gain $G_c = \sqrt[S]{\Gamma(S+1)}\,(\alpha_{us}\, R_0\, \gamma_{\text{th}})^{-1}$. It is also intuitively verifiable since there are S independent paths between every user and the GS. Also, the term $\sqrt[S]{\Gamma(S+1)}$ indicates that as the number of satellites (S) increases, the cooperation gain G_c grows sublinearly. This suggests that while adding more satellites improves cooperation, the marginal gain diminishes with each additional satellite.

4.7.2 *Asymptotic OP for SIC-based decoding*

Since the asymptotic SINR γ_{us}^{∞} in (4.55) is independent of G_s, the asymptotic SINR $\gamma_u^{\infty(1)}$ and consequently the OP $P_{\text{out}}^{\infty(1)}(\mathcal{R})$ for the best user in SIC-based decoding can be conveniently calculated as

$$\gamma_u^{\infty(1)} = \max_u \left(\sum_{u=1}^{U} \gamma_{us}^{\infty}\right), \tag{4.71}$$

$$\begin{aligned} P_{\text{out}}^{\infty(1)}(\mathcal{R}) &= F_{\gamma_u^{(1)}}^{\infty}(\gamma_{\text{th}}) \\ &= \left(\left[F_{\gamma_u}^{\infty}(\gamma_{\text{th}})\right]^U \times \mathbb{P}[K_{\text{vis}} \geq S]\right) + \mathbb{P}[K_{\text{vis}} < S]. \end{aligned} \tag{4.72}$$

Similar to CM-decoding, the optimal number of supported users and the required number of satellites with assured visibility can be obtained in SIC as well.

4.8 Simulation results

This section presents simulation and theoretical results derived in this work to get useful insights into the system. The algorithm for computing OP using Monte-Carlo simulations for both the proposed decoding schemes is provided in Algorithm 1. This section initially validates the theoretical analysis with the simulation results. Later, the effect of various system parameters on OP performance is analyzed. Since many parameters affect the performance, an attempt is made to understand them individually by keeping all other parameters constant. All the simulations and plots have been generated using MATLAB with $= 10^5$ channel realizations. Unless stated otherwise, the default parameters used for simulations are mentioned in Table 4.2. The link and stochastic geometry-related parameters have been selected following 3GPP TR 36.763 [6], and [15], respectively. The imperfect CSI has

Algorithm 1 OP simulation for CM and SIC

Initialize: No. of channel realizations L
Initialize: $U, S, r_{\text{min}}, \theta_0$, and other link parameters
Generate: Channel $\mathbf{H}_{U,S,\text{L}}$, $\mathbf{G}_{S,\text{L}}$, Range $\mathbf{R}_{U,S,\text{L}}$
for $l = 1$ to U **do**
  Compute: $\gamma_{us}^{(l)} \quad \forall\, u \notin \mathbf{D}[\,l-1\,]$
  Perform: MRC: $\gamma_u^{(l)} \leftarrow \sum_{s=1}^{S} \gamma_{us}^{(l)} \quad \forall\, u \notin \mathbf{D}[\,l-1\,]$.
  if $l = 1$ **then**
    CM: $\gamma_u \leftarrow \texttt{sort}\, \gamma_u^{(1)}$
    SIC: $\gamma_{\mathbf{D}\{l\}}^{(l)} \leftarrow \max_u \gamma_u^{(l)}$
  else if $l > 1$ & $\gamma_{\mathbf{D}\{l-1\}}^{(l-1)} > \gamma_{\text{th}}$ **then**
    SIC: $\gamma_{\mathbf{D}\{l\}}^{(l)} \leftarrow \max_{u, u \notin \mathbf{D}[\,l-1\,]} \gamma_u^{(l)}$
  else
    SIC: $\gamma_{\mathbf{D}\{l\}}^{(l)} \leftarrow 0$
  end if
  Remove: Entries of $\mathbf{D}[l]$ from $\mathbf{H}$, $\mathbf{G}$ and $\mathbf{R}$
end for
Compute: $\mathbb{P}[K_{\text{vis}} \geq S] = 1 - \sum_{j=0}^{S-1} \binom{K}{j} \mathcal{P}^j \left(1-\mathcal{P}\right)^{K-j}$
Compute: $\mathbb{P}\left[\gamma_u \leq \gamma_{\text{th}}\right] = \texttt{sum}(\gamma_u^{(l)} \leq \gamma_{\text{th}})/L$
Compute: $P_{\text{out}}(\mathcal{R}) = \mathbb{P}\left[\gamma_u \leq \gamma_{\text{th}}\right] \times \mathbb{P}[K_{\text{vis}} \geq S]$

Table 4.2 List of parameters considered for simulation.

Parameter	**Value**	**Ref.**
Mask elevation angle θ_0	10°	[6]
Target rate $\mathcal{R}$	10 kbps	
Bandwidth B	125 kHz	
User antenna transmit gain	0 dBi	
Satellite antenna Tx/Rx gain	30 dBi	
Constellation Size K	720	[15]
Constellation altitude h	1200 km	
Radius of the Earth r_e	6371 km	
Noise power at the GS σ_w^2	-98 dBm	
Path loss exponent α	2	
Average Shadowing (m, b, ω)	$(2, 0.063, 0.0005)$	[110]
Heavy Shadowing (m, b, ω)	$(5, 0.251, 0.279)$	

been modelled using $\chi = 0.05, \phi = 10$ and $\xi = 0.05$ as done in [130]. Also, while computing the numerical Laplace inverse as in (4.39), parameters mentioned in Table 4.2 are used to maintain the discretization and truncation error less than 10^{-10} which is negligible compared to the range of derived OP. For solving the optimization problem using GA in MATLAB, the `ConstraintTolerance`,

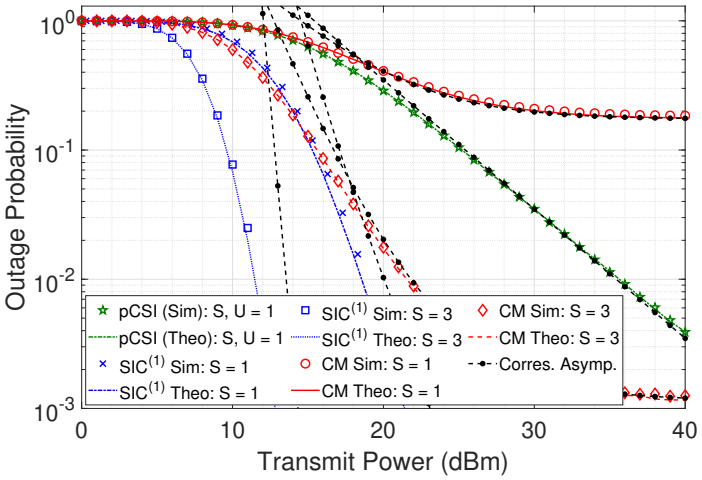

Figure 4.6 Validation of theoretical and simulation results: OP vs transmit power P_u in both SIC and CM for $U = 5$ and different number of satellites S. Expressions for no-interference (U=1) and perfect CSI (pCSI) are also verified.

`FunctionTolerance`, and `PopulationSize` were set to 10^{-6}, 10^{-8}, and 50 respectively. A desktop PC with Intel(R) Core(TM) i7-8700 CPU operating at 3.20 GHz $\times$ 6 cores and 32 GB of memory was utilized for running the solver.

4.8.1 *Validation of theoretical and simulation results*

Fig. 4.6 shows the average OP vs transmit power P_u for $U = 5$ users in the case of $S = 1$ and $S = 3$ satellites. The OP for every user in the order of their SINRs has been calculated and then averaged to obtain the average OP of the system. It is observed that the average OP derived theoretically using the approximation is very close to the simulation results for CM decoding and best user in SIC based decoding. This validates the correctness of the derivation presented in Section 4.6.1 and Section 4.6.2. It can also be observed that the asymptotic curves derived analytically in (4.61) and (4.72) approach the simulated curves rapidly, thus validating the correctness of the derived expressions. Moreover, the asymptotic expression presented in (4.70) for the special case with no interference ($U = 1$) and perfect CSI (pCSI) also matches with the simulations. It can indeed be observed that the slope of the curves is also equal to the number of satellites used for AF ($S = 1$ in this case), thus validating the diversity order as well.

Two more observations can be made from Fig. 4.6. First, the OP per user decreases with an increase in the transmit power of the IoT users. An IoT user's feasible transmit power range from 12 dBm to 20 dBm can achieve OP ranging from 10^{-1} to 10^{-3} in SIC. Second, as the transmit power increases, the interference effect starts dominating, thus leading to the performance difference between SIC and the CM decoding. However, with an increase in the number of satellites, the OP decreases sharply. The scenario with $S = 1$ represents the conventional satellite communication scheme without multiple satellites being visible, unlike the mega-LEO constellations. At high SNRs, the OP in the case of CM

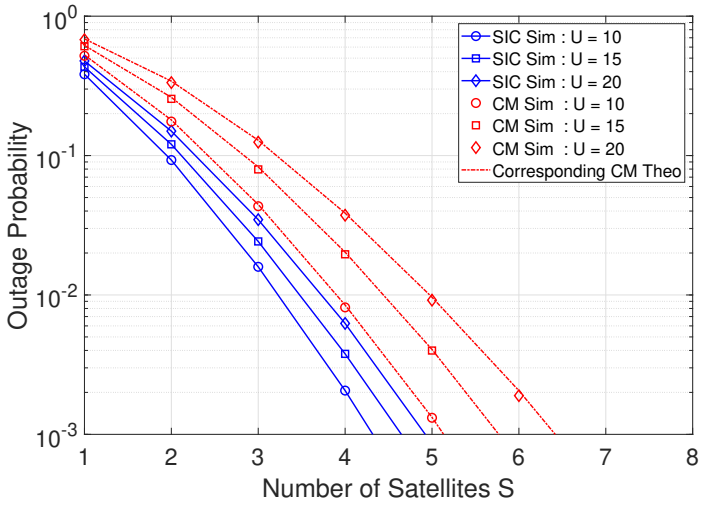

Figure 4.7 Effect of number of satellites S: Averaged OP vs S in both SIC and CM at $P_u = 20$ dBm and different number of users U.

decoding decreases from 10^{-1} to 10^{-3} by the addition of two more satellites. It can be observed that by leveraging the benefits of multiple visible satellites, transmit power of 30-35 dBm in CM and 12-15 dBm for the best user in SIC can achieve an OP of 10^{-3} in a 3 satellite, 5 user system.

4.8.2 *Effect of the number of satellites*

Figure 4.7 shows the OP as a function of the number of satellites S for $U = 10, 15$ and 20 users at $P_u = 20$ dBm. It is observed that for a fixed number of users, as the number of satellites increases, the OP decreases sharply. It can be observed that merely an addition of 3-4 satellites can reduce the OP from 10^{-1} to 10^{-3} in both CM and SIC decoding. This also clearly demonstrates how the IoT users can leverage multiple visible satellites of the constellation to enhance system performance. Additionally, it is interesting to note that the OP for 15 users case in SIC is less than the OP for five users case in CM.

4.8.3 *Effect of constellation size*

Fig. 4.8 shows the effect of the constellation size K on OP for $U = 15$ users at $P_u = 20$ dBm, and $S = 2, 3$ and 4 satellites. It can be observed that OP decreases smoothly with an increase in K until a floor is reached. In this case, the floor represents the scenario where OP can't be decreased further, even by adding more satellites to the constellation. The point at which OP saturates denotes the constellation size for which the visibility of S satellites to be utilized in AF-relaying can be ensured (i.e. the constellation size such that $\mathbb{P}[K_{\text{vis}} \geq S] = 1$). Given a target OP to be achieved and the number of satellites intended to be used for AF-relaying, this figure can be utilized to obtain the minimum required size of the mega-LEO constellation. For example, if 4 satellites are to be used for AF-relaying, increasing the constellation size from 150 to 360 can improve the OP from 10^{-1} to $3 * 10^{-3}$ in the case of SIC decoding and from 10^{-1} to $2 * 10^{-2}$ in case of CM decoding. It can also be observed that

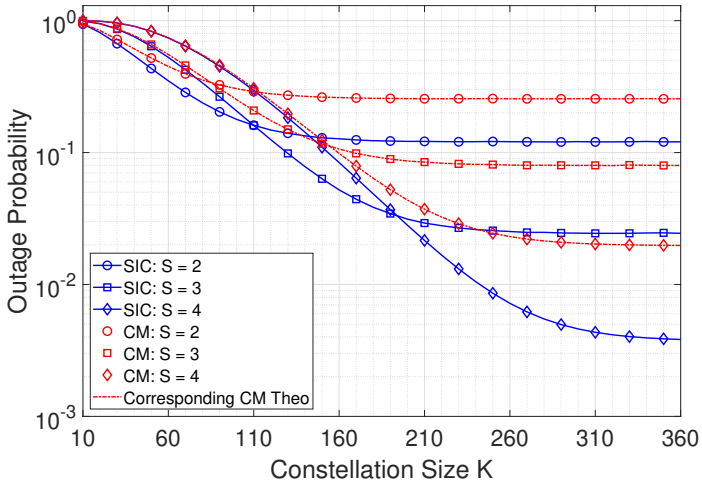

Figure 4.8 Effect of constellation size K: OP vs K for both SIC and CM at $P_u = 20$ dBm, $U = 15$, and different number of satellites S.

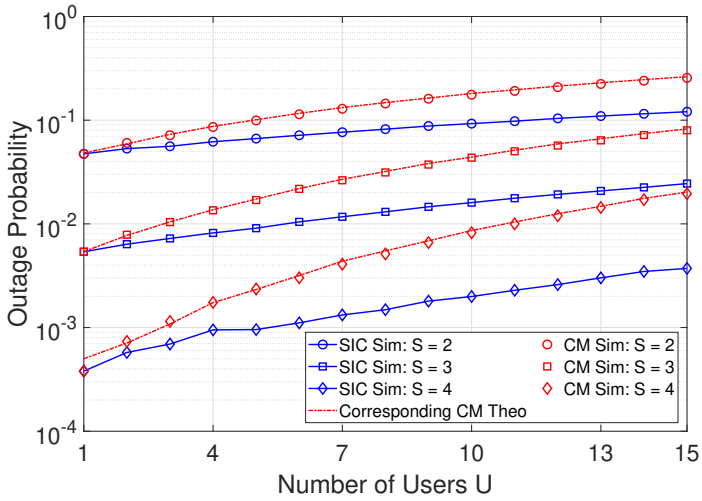

Figure 4.9 Effect of number of users U: Average OP vs U for both SIC and CM scheme at $P_u = 20$ dBm and different values of satellites S.

for a fixed S, the performance difference between SIC and CM increases with an increase in K before saturating. This can be attributed to the fact that the term $\mathbb{P}[K_{\text{vis}} < S]$ in (4.28) and (4.45) dominates at low K values irrespective of the decoding schemes. However, as K increases, $\mathbb{P}[K_{\text{vis}} \geq S]$ also increases, making the performance of decoding schemes more evident.

4.8.4 *Effect of the number of users*

Figure 4.9 shows the impact on the OP as a function of the number of users U at $P_u = 20$ dBm for $S = 2, 3$ and 4. It can be observed that the OP increases with an increase in the number of users due to the increase in interference. It can also be observed that the performance gap between the SIC and CM

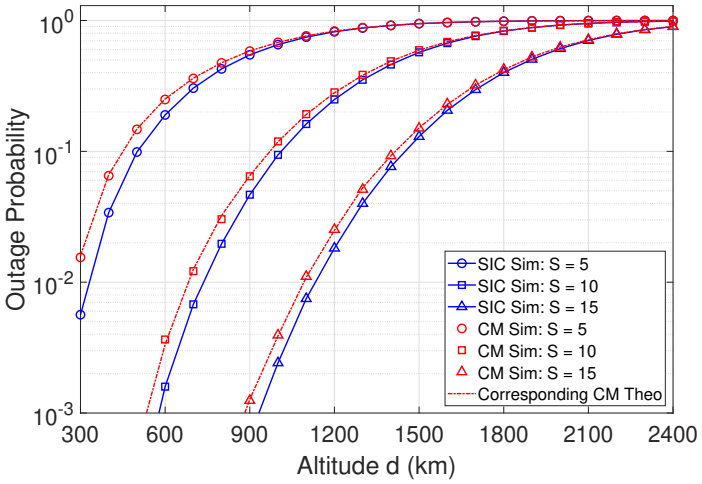

Figure 4.10 Effect of altitude d: Average OP vs d for both SIC and CM at $P_u = 20$ dBm, $U = 15$ and different values of satellites S.

also increases with an increase in U. This can be attributed to the fact that the impact of interference decreases with decoding of subsequent users in SIC whereas CM assumes a constant number of interferers for all the users. It is interesting to note that the difference between the performance of SIC and CM becomes significant as more and more satellites are added to the system.

4.8.5 *Effect of altitude*

Figure 4.10 shows the impact of altitude on the OP for $S = 5, 10$ and 15 satellites and $U = 15$ users at $P_u = 20$ dBm. It can be observed that OP increases as the altitude increases. This is because the constellation's altitude directly impacts the path loss observed by the signals. It can also be observed that while more satellites enhance the OP performance because of better elevation angles, the benefit of adding more satellites diminishes rapidly with increasing altitude. Hence, the number of satellites and the selection of decoding scheme can be traded off with the altitude and number of users.

Usually, the LEO satellites are considered to be placed between 600 km to 1800 km. Hence, for a desired OP at a fixed transmit power, Figure 4.10 can be used to determine the minimum number of satellites required in look angle for various constellations at different altitudes. For example, using SIC, in a network of 15 active users, a minimum of 15 satellites at nearly 900 km are required to achieve an OP of 10^{-3}. A similar performance can be achieved with ten satellites only if placed at an altitude of 600 km.

4.8.6 *Effect of mask elevation angle*

Figure 4.11 shows the effect of θ_0 on OP for $S = 3$ satellites and $U = 15, 20$ and 25 users at $P_u = 20$ dBm. The OP decreases with an increase in θ_0; however, the rate of decrease changes at around $\theta_e = 40^\circ$ for the shown case of $S = 3$. It can be explained by the two-fold impact of θ_0 on the

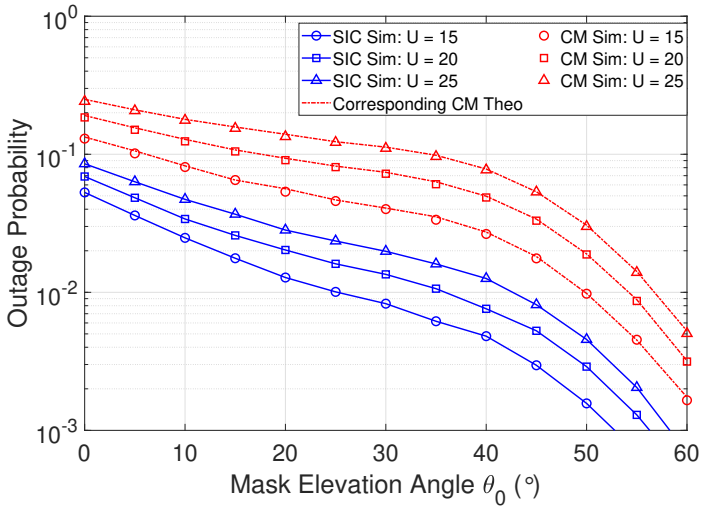

Figure 4.11 Effect of mask elevation angle θ_0: OP vs θ_0 for both SIC and CM at $P_u = 20$ dBm, $S = 3$ and different number of users U.

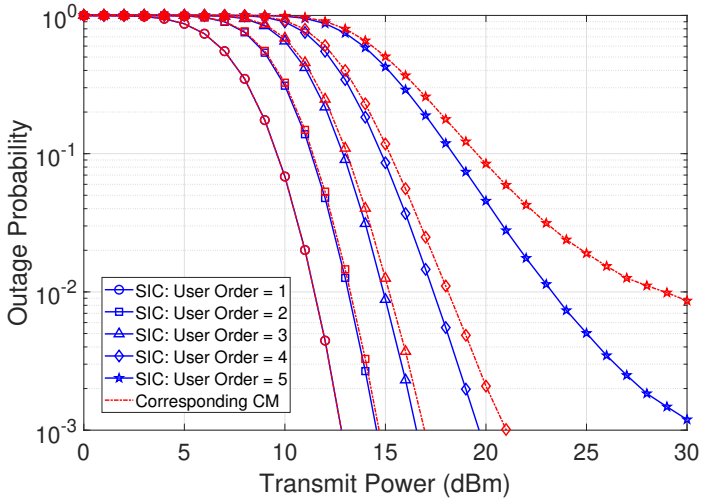

Figure 4.12 Effect of decoding order l: OP vs transmit power P_u for ordered decoding in both SIC and CM for $U = 5$ and $S = 3$.

OP. As evident from (4.12) and (4.18), A_{vis} decreases with an increase in θ_0. Hence the probability of seeing a defined number of satellites decreases with an increase in θ_0 for every user. It, therefore, tends to increase the OP. On the other hand, as evident from (4.30), an increase in θ_0 decreases the distance and, consequently, the average path loss between the users and the satellites. It, therefore, tends to reduce the OP. The impact of reducing path loss dominates nearly till $\theta_0 = 40°$. However, after that, the reduced probability of seeing a defined number of satellites rapidly decreases the OP.

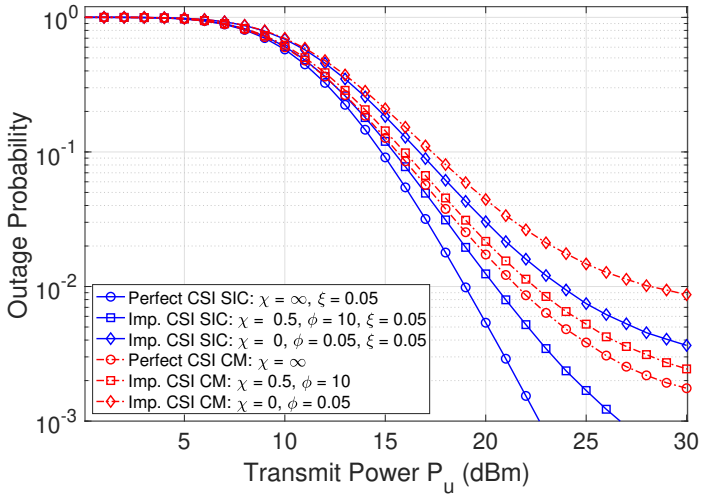

Figure 4.13 Effect of imperfect CSI: OP vs SNR plots for scenarios with perfect ($\chi = \infty$) and imperfect CSI in both CM and SIC-based decoding for $U = 5$, $S = 3$ and different values of mismatch parameters χ, ϕ and ξ. Here $\chi = 0$ represents SNR-independent, and $\chi \neq 0$ represents SNR-dependent CSI mismatch.

4.8.7 *Effect of decoding order and trade-offs*

Figure 4.12 shows the OP for various users in ordered decoding, where user 1 means the first user being decoded in SIC. Similarly, in a 5-user scenario, user 5 means the last user decoded in SIC. The OP for corresponding CM has also been shown in Figure 4.12 where the user order is solely determined by the SINRs without removing interference for any user. It can be observed that the initial few users in the order have similar OP for both SIC and CM. It can be attributed to the fact that the interference in both SIC and CM remains nearly similar for the initial few users. However, for higher order decoding in SIC, the interference decreases significantly due to the subtraction of information signals of the decoded user. This is not the case in CM; decoding of higher order users happens in heavy interference from users with better channel conditions. Hence, the difference between the OP performance of SIC and CM increases significantly for higher-order users. It can be concluded that trading off with the throughput and desired OP, the initial few users can be decoded using CM only, thus reducing the decoding complexity. However, for applications requiring decoding of all or most users, SIC is preferable to CM.

4.8.8 *Effect of channel imperfections*

Figure 4.13 shows the average OP versus the transmit power P_u for both the CM and the SIC-based schemes for $U = 5$ users and $S = 3$ satellites under perfect and imperfect CSI scenarios. The results demonstrate that the OP performance deteriorates in the presence of CSI mismatch compared to the ideal case when perfect CSI ($\chi = \infty$) is available. Two types of CSI mismatch: the SNR-dependent CSI mismatch ($\chi \neq 0$) and the SNR-independent CSI mismatch ($\chi = 0$) are shown in Figure 4.13. When $\chi \neq 0$, the variance of the CSI estimation error depends on the link SNR, and the impact of χ

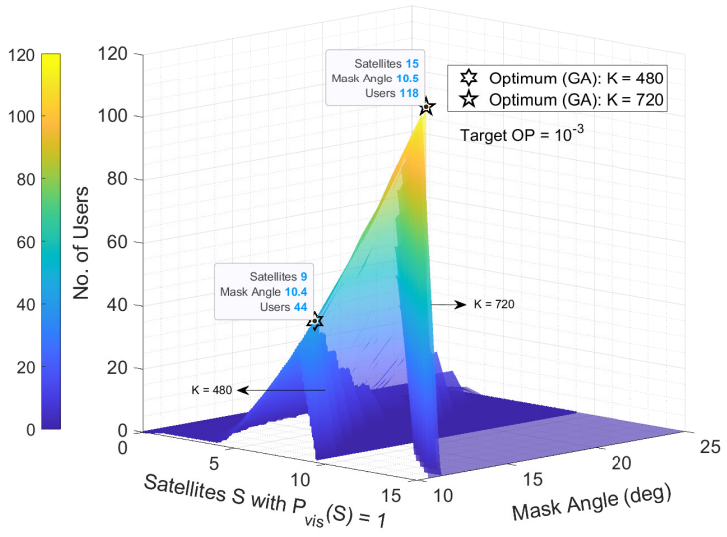

Figure 4.14 Maximum number of users which can achieve the target OP of 10^{-3} using CM decoding versus the number of satellites S required with $\overline{P}_{\text{vis}}(S) = 1$ (also mentioned as number of satellites with assured visibility) and varying mask angle. (generated for a constellation of 720 satellites at 1200 km and IoT users with P_u = 20 dBm)

is dominant in determining the system performance. The rate of decline in $\sigma^2_{e_{us}}$ and $\sigma^2_{e_s}$ depends on χ, and thus an increase in χ is expected to result in improved OP performance. The SIC decoding is more affected than the CM decoding as the residual error due to imperfect decoding accumulates successively in SIC. For example, at 22 dBm transmit power, the OP with imperfect CSI at $\chi = 0.5$ is 3.4 times higher than the OP with perfect CSI in the case of SIC decoding but only 1.3 times higher in the case of CM decoding.

In contrast, when $\chi = 0$, the variance of the CSI estimation error solely depends on ϕ. It can be observed that the impact of imperfect CSI is negligible at low SNRs as the products $\eta_{us}, \sigma^2_{e_{us}}$ and $\eta_{us}, \sigma^2_{e_{us}}$ approach zero, and the CSI quality tends to be perfect. However, significant degradation in OP performance is observed as the transmit power increases, particularly above 15 dBm in SIC and 18 dBm in CM decoding.

4.8.9 *Optimum number of users for a target OP*

Fig. 4.14 shows the approximate number of users which can be served for a target OP of 10^{-3} using CM decoding against the number of satellites with assured visibility and varying mask angles for two different constellation sizes, $K = 480$ and $K = 720$. These results are obtained using the asymptotic expressions derived in Section 4.7. Here, the number of satellites S with assured visibility refers to the number of satellites required such that $\overline{P}_{\text{vis}}(S) = 1$. It can be observed that A_{vis} decreases with an increase in θ_0, as derived in (4.12) and (4.18), thereby decreasing the number of satellites with assured visibility. The maximum number of supported users obtained using the GA optimizer can be verified

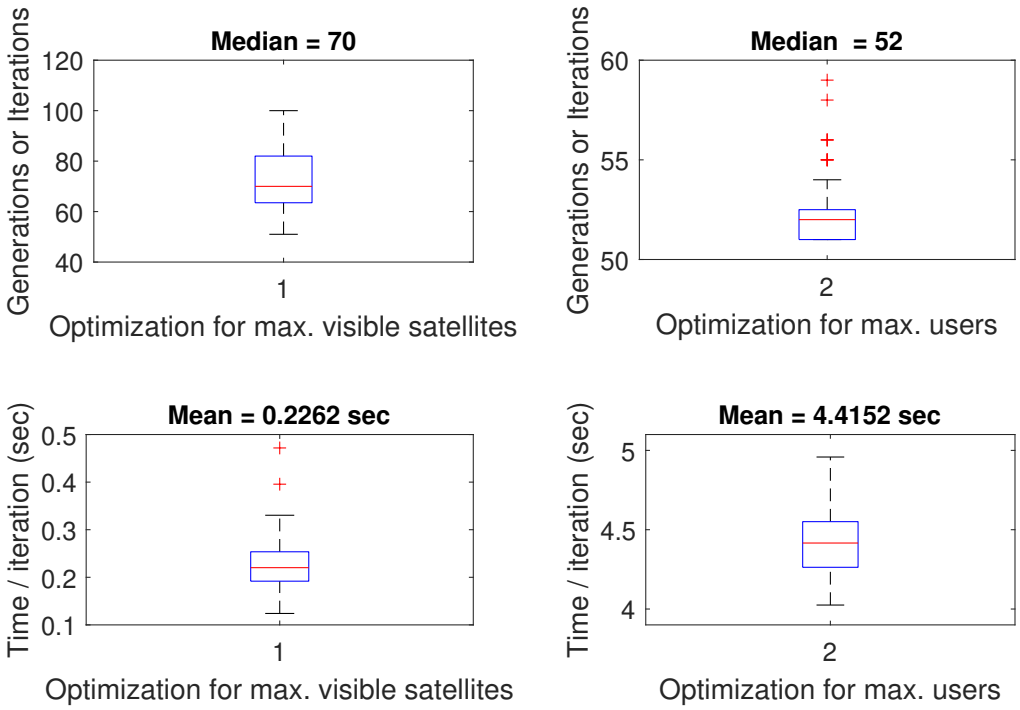

Figure 4.15 Box plots (generated using 100 repetitions) representing the median number of generations (iterations) and time per generation (in sec) taken to converge for the two GA-based optimizations. The maximum number of satellites with assured visibility and the corresponding mask angle is obtained in 70 generations, each taking 0.2262 sec on average. Meanwhile, the maximum number of supported users is obtained in 52 generations, each taking 4.4152 seconds on average.

using a simple grid-based algorithm where the OP is calculated for every possible U for a (θ_0, S) pair obtained from a grid of all likely S, θ_0 values. It is worth mentioning that the asymptotic expressions can be efficiently used for such iterative grid-search methods since they do not contain any integrals to be computed numerically. As shown in Fig. 4.14, the optimal values obtained from the GA optimizer match the values obtained using the grid search algorithm. For example, considering 720 satellites in the constellation and users with 20 dBm transmit power, approximately 118 users can be supported optimally using CM decoding for a target OP of 10^{-3} using 15 satellites at $\theta_0 = 10.5°$. The number of supported users falls to 44 if the constellation has 480 satellites only. Similar approximations can also be made for SIC decoding.

The GA algorithm converged in 70 iterations (median), taking 0.2262 sec per iteration on average to obtain the number of satellites S^* and the mask angle θ_0^*. Given S^* and θ_0^*, it converged in 52 iterations (median), taking 4.4152 sec per iteration on average to obtain the number of users U^*. The statistics of the number of iterations and the average time per iteration are presented in Figure 4.15. Also, the convergence of the GA for both optimization problems in terms of the average change in the penalty fitness values is presented in Figure 4.16. In both optimizations, the GA terminates when the average change in the penalty fitness value is less than the defined `FunctionTolerance` and constraint

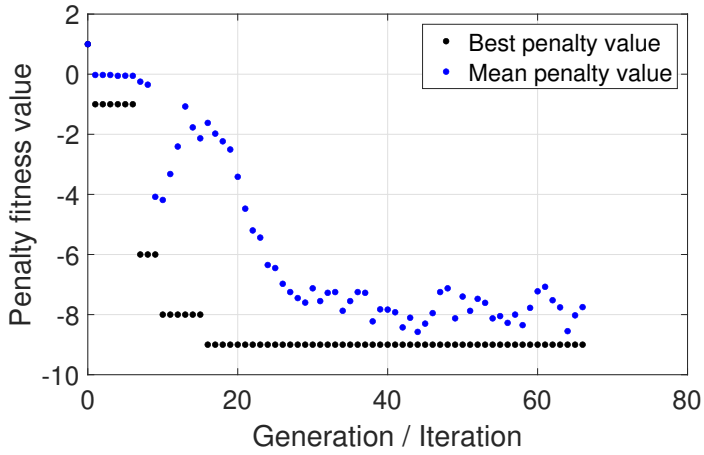

(a) Optimization for max. visible satellites

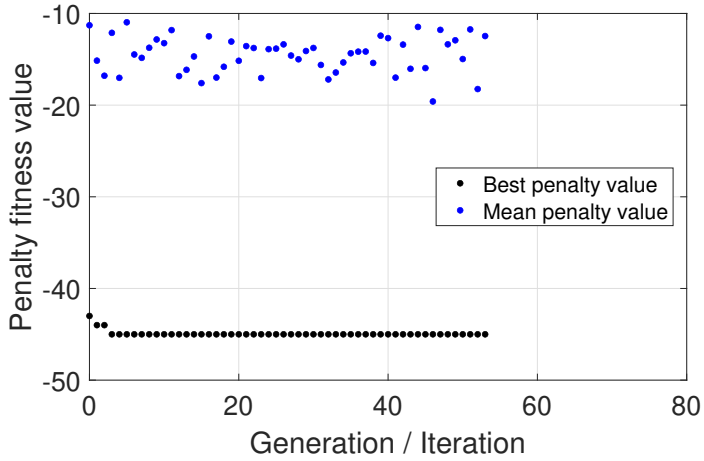

(b) Optimization for max. users

Figure 4.16 Penalty fitness value vs. the number of generations (iterations) for a single GA optimization run. In both optimizations, the GA terminates when the average change in the penalty fitness value is less than the defined `FunctionTolerance` and constraint violation is less than the defined `ConstraintTolerance`. It can be observed that the GA converges within the number of iterations shown in Fig. 4.15.

violation is less than the defined `ConstraintTolerance`. It is worth observing that the GA solver for obtaining the maximum number of supported users takes relatively more time per iteration. In GA, the time taken per iteration depends upon the fitness function, which depends on the application. In our case, the time difference is obvious because the fitness function in the case of obtaining the maximum number of users involves calculating end-to-end OP, $P_{\text{out}}^{\infty}(\mathcal{R})$. Whereas the fitness function in the case of obtaining maximum visible satellites calculates relatively less complex $\overline{P}_{\text{vis}}(S)$ only.

4.9 Summary

This chapter presented a simple and energy-efficient direct-access topology for LEO satellites-based IoT networks. The OP performance of the topology was analysed using stochastic geometry to model the random satellite locations. In this context, analytical expressions were derived for average OP in the CM decoding scheme, and the OP of the best user was derived for the SIC decoding scheme, assuming imperfect knowledge of the CSI. Simplified expressions of the OP were also derived under high SNR assumptions which demonstrate that OP attains a floor due to interference and imperfect CSI. The asymptotic expressions were utilized to obtain an optimal region of operation achieving a target OP. Although all the IoT users transmit at the same power, it was found that the SIC decoding scheme performs better than the CM decoding scheme. The theoretical analysis was verified through rigorous simulations. The effects of system parameters like the number of users, number of satellites, altitude, and mask elevation angle of the constellation on the OP performance were discussed in detail. The results of this chapter demonstrate that for the practical values of the above system parameters, the proposed topology is feasible and attractive for low-powered IoT networks.

Chapter 5

Efficient Transmission Scheme for LEO Satellite-Based IoT Networks

This chapter focuses on the MAC aspects by proposing a change detection and ML-based transmission scheme for satellite IoT. A Shewhart-based transmission reduction scheme is utilized to optimize the transmission scheme to accommodate more users within the network and improve energy efficiency. ML algorithms are also proposed to reduce the payload size by leveraging the correlation among the sensed parameters. Initially, the system model is described, followed by an in-depth discussion of the real-world data from an IoT testbed, which is used for performance analysis in this chapter. The measurement campaign and various steps involved in prepossessing and data-set creation are also described. The Shewhart-based transmission reduction scheme, along with the ML algorithms and the proposed transmission modes, are also described in this chapter. Towards the end, the performance of the proposed scheme is analysed in terms of the percentage reduction in transmissions, collision probability, effective data received at the server and battery life.

5.1 Background

Many LEO constellations targeting IoT applications provide discontinuous coverage, introducing the challenge of limited visibility duration [135,136]. The satellites in sparse LEO constellations make multiple passes in a day with inter-pass duration depending upon the constellation size and orbit. Moreover, the longer propagation distance and higher path loss also lead to lower data rates in LEO satellite-based systems than terrestrial systems. Hence, traffic/overhead reduction and energy efficiency efforts are paramount in all NTN scenarios. Recently, the adaptation of LPWAN protocols like NB-IoT and LoRaWAN for NTN connectivity have gained much traction. In [96], authors proposed a novel uplink resource allocation strategy considering the dynamic nature of LEO satellite channels, differential Doppler shifts, and increased propagation delays. The study in [97] proposed a robust random access technique addressing the key challenges of long delays, significant Doppler effects, and wide beams. It also demonstrated its adaptability to various NTN configurations outlined by 3GPP for the 5G new radio system. The adaptability of LoRa modulation technology to LEO satellite IoT scenarios and its various aspects, such as network architecture, access mechanisms, and bandwidth, were studied in [91]. The potential application of chirp spread spectrum (CSS), a technology traditionally employed in radar

and sonar, in the realm of LEO satellite communication systems for low-data-rate transmission was also studied in [92]. In [93], the synchronization challenges were addressed through the innovative Scheduling Algorithm for LoRa to LEO Satellites (SALSA). Using TDMA instead of traditional ALOHA-based LoRa, SALSA ensures reliable communication, mitigating issues like packet drops and collisions.

Apart from scheduling algorithms, various random access algorithms and MAC protocols have also been studied for satellite IoT networks. A comprehensive review of MAC protocols for nanosatellite IoT was presented in [137]. The assessment considered channel load, throughput, energy efficiency, and complexity factors. ALOHA-based protocols and interference cancellation-based protocols emerged with notable performance metrics, yet the study emphasized the need for improved designs that balance communication performance, energy consumption, and complexity. In [138], an innovative collision detection scheme for satellite-based IoT was proposed, emphasizing enhanced access efficiency and resource utilization. The scheme enabled rapid collision detection, and the paper provided optimal preamble selection probabilities to maximize load monitoring accuracy. The constrained application protocol (CoAP) was studied in [139] for reliable delivery of IoT traffic. It established an analytical model to assess system performance under non-saturated conditions, considering MAC parameters over a random access satellite channel with a closed-loop congestion control mechanism.

The limited visibility duration of LEO satellites necessitates an optimized access scheme to accommodate more users within the network. Transmission reduction schemes, traditionally used as a measure to improve energy efficiency in IoT networks, can be used along with access protocols to reduce traffic in satellite-based IoT networks. Various transmission reduction schemes have been studied in the literature specifically for terrestrial IoT networks. Authors in [140] proposed a Shewhart change detection test for a real-time smart metering system. The system transmitted local power measurements to a central processing point only when deviations exceeded a predefined threshold from the last transmitted measurement. The average time to a new transmission was derived analytically. The authors in [141] introduced piggybacking and interpolation techniques to further reduce the error without increasing packet transmissions in a Shewhart-based temperature monitoring system. The battery lifetime analysis showed a significant error reduction with a marginal battery lifespan decrease. In [142], the authors introduced an innovative ML-driven approach to transmission reduction in IoT. The study comprehensively compared supervised machine learning algorithms, considering the challenges posed by memory and computation constraints on microcontrollers.

In the context of IoT, the Poisson traffic model is widely adopted, including in the standardization works at 3GPP [143], and for performance analysis of random access schemes in general [144]. Various traffic models for analysing the performance of MAC schemes in IoT networks are also studied in [145–147]. The Poisson model is adopted in [143] considering the *Palm-Khintchine Theorem*, which states that the superposition of asymptotically large independent renewal processes with iid inter-arrival times would lead to a Poisson process. However, as shown in [145], this assumption could lead to large errors for aggregated periodic IoT data. Even for aperiodic event-driven IoT applications with real-world data, the Poisson model is not followed as shown in [146] and [147]. With the implementation of the

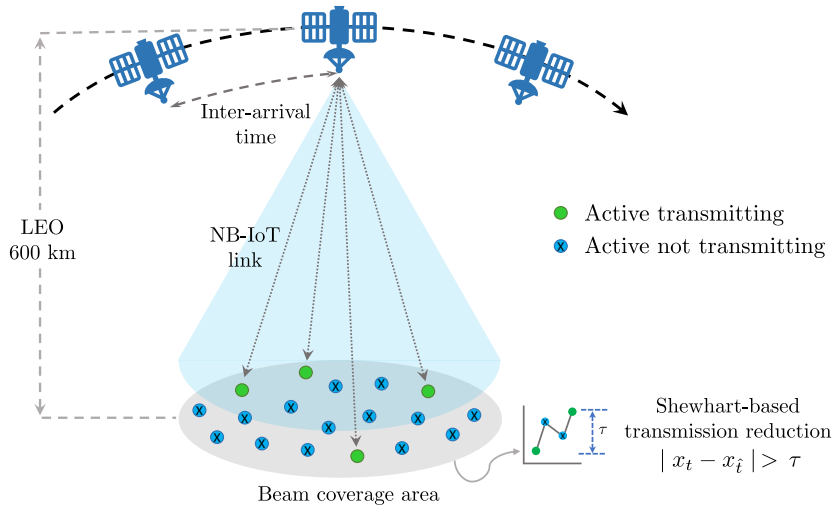

Figure 5.1 System model: Direct-access NB-IoT network with LEO satellites at 600 km and having discontinuous coverage. All the devices under the coverage area perform Shewhart-based transmissions during the visibility period.

transmission reduction scheme, the average time for a new transmission does not remain independent of the last transmission as assumed in the Poisson process. On the contrary, it depends on the nature of sensed data and factors affecting the sensing environment in the case of IoT applications. Thus, traditional assumptions like Poisson traffic may not align with real-world scenarios while analysing the performance of transmission reduction schemes. Real data from IoT deployment is necessary to emulate the traffic accurately.

While the previous study in [93] proposed an access scheme for LEO satellite-based IoT networks considering the limited visibility aspect, it utilizes TDMA in LoRaWAN, unlike the Shewhart-based RACH procedure being proposed in this thesis for NB-IoT. Similarly, [138] focused on collision detection and load estimation while [139] focused on designing a rate-control algorithm implemented as a CoAP congestion control algorithm. On the contrary, this thesis utilises transmission reduction to reduce collisions, increase energy efficiency, and improve resource utilisation. Moreover, unlike this chapter, none of the above papers utilized any dataset from real-world IoT deployment to analyse their systems. The work in [140–142] was related to Shewhart and ML-based schemes for transmission reduction in IoT, but none of them considered a LEO satellite scenario.

5.2 System model

In this chapter, NB-IoT is adopted as an IoT communication protocol, as shown in Figure 5.1. In the 3GPP framework, four reference scenarios have been specified depending on the orbit nature: GEO, MEO or LEO, and beam type—whether steerable or fixed. All scenarios are studied under the assumptions of sub-6 GHz bands, transparent payload, and no inter-satellite link. In this work, we adopt an NTN

Table 5.1 Satellite parameters for Set-1 and Set-4 configuration [6].

Parameters	LEO - 600 km	
	Set-1	**Set-4**
Central beam center elevation angle	30°	90°
Central beam edge elevation angle	27°	30°
3 dB beam width	4.4127°	104.7°
Frequency band	S-band (i.e. 2 GHz)	
Satellite EIRP density (dBW/MHz)	34	21.45
Satellite G/T (dB/K)	1.1	-18.6

architecture where the IoT devices are distributed in rural and suburban areas and connected via LEO satellites with sparse constellations. 3GPP has defined four sets of beam layout and radio frequency parameters for the payload: Set-1, Set-2, Set-3, and Set-4. The Set-1 represents the best-case scenario with small spot beams. On the contrary, the Set-4 configuration represents the general and worst cases with one large beam. Although this chapter considers constellation with discontinuous coverage, the observations remain relevant for constellations for continuous coverage also since it is assumed that IoT terminals would connect and follow one satellite at a time to reduce the complexity in antenna and signal processing aspects. Table 5.1 provides the Set-1 and Set-4 configuration parameters for LEO satellites at 600 km altitude.

5.2.1 *Link budget*

The uplink budget for Set-1 and Set-4 is presented in Table. 2.3 of Chapter 2. The evaluation considers operation in the S-band at a carrier frequency of 2 GHz. For the UL, the SNRs depend on the signal bandwidth. In Set-1, the best case with multiple spot beams, 15.96 dB and 19.56 dB SNR is achieved with a 3.75 kHz single-tone configuration at the edge and centre of the beam, respectively. On the other hand, the SNRs are reduced to -0.85 dB and 2.75 dB when using full NB-IoT bandwidth (multi-tone) at the edge and centre of the beam, respectively. Although decent for Set-1, the obtained SNRs for Set-4 are quite low. In set-4, the SNRs achieved are -3.13 dB to 4.93 dB in 3.75 kHz single-tone configuration and -19.95 dB to -11.88 dB for full bandwidth multi-tone configuration. In this chapter, we adopt the Set-4 configuration for further analysis to show the show performance in the worst-case scenario. According to [148], the link can still be closed with the obtained SNRs in Set-4 configuration such that one can achieve a data rate of up to 1.6 kbps for the UL.

5.2.2 *Communication steps in NB-IoT*

In NB-IoT, communication unfolds in two distinct phases. The initial phase, known as the access or contention phase, involves nodes vying for connection establishment with the eNB through the narrow-

band physical uplink shared channel (NPRACH). This is achieved by transmitting a preamble during random access opportunities (RAO), which can present 12 to 48 connection possibilities as subcarriers. Contesting nodes randomly select an index within these possibilities for preamble transmission. Collisions resulting from two or more nodes choosing the same preamble index lead to retries and failures. Successful preamble transmission initiates the data phase, exchanging messages on allocated resources without contention. Despite this, failures may still occur due to congestion or transmission errors. However, this chapter focuses on the collision probability during the random access phase of NB-IoT.

To compute the collision probability, consider an individual subcarrier in a particular RAO with m_{RAO} subcarriers [149]. Let X_i be the random variable representing the number of nodes that select the i^{th} subcarrier for transmitting their preamble in the same RAO for a network with N nodes. Then, the probability $\mathbb{P}[X_i = k]$, that k nodes select the same subcarrier can be written as

$$\mathbb{P}[X_i = k] = \binom{N}{k} \left(\frac{1}{m_{\text{RAO}}}\right)^k \left(\frac{m_{\text{RAO}} - 1}{m_{\text{RAO}}}\right)^{N-k}. \tag{5.1}$$

A transmission is considered successful only if a preamble is selected by one node. Therefore, the number of nodes that reattempt the procedure can be written as

$$\begin{aligned} N_{\text{coll}} &= N - (m_{\text{RAO}} \times \mathbb{P}[X_i = 1]) \\ &= N \left(1 - e^{-N/m_{\text{RAO}}}\right). \end{aligned} \tag{5.2}$$

Each of the colliding devices selects another sub-carrier after a back-off (BO) window with probability P_{BO}. The collision probability for a node in an arbitrary RAO is given in [150] by

$$\mathcal{P}_{\text{coll}} = 1 - \exp\left(-\frac{N_{\text{coll}}\, P_{\text{BO}}}{m_{\text{RAO}}}\right). \tag{5.3}$$

5.3 IoT testbed and dataset for experimental validation

In this work, the performance of the proposed schemes and system model is experimentally validated using the data from an IoT testbed, AirIoT, established by IIIT Hyderabad (IIITH), India, for air quality monitoring in a city.

5.3.1 *Measurement campaign*

AirIoT is a network of 49 air pollution monitoring devices deployed in an area of approximately 4 km^2 in the Gachibowli region of Hyderabad, the capital city of Telangana state in India. This kind of deployment could indicate many other IoT networks, e.g. livestock, agriculture, and floating sensors for tsunami prevention, thus helping in understanding a real-life scenario. In AirIoT, the devices were

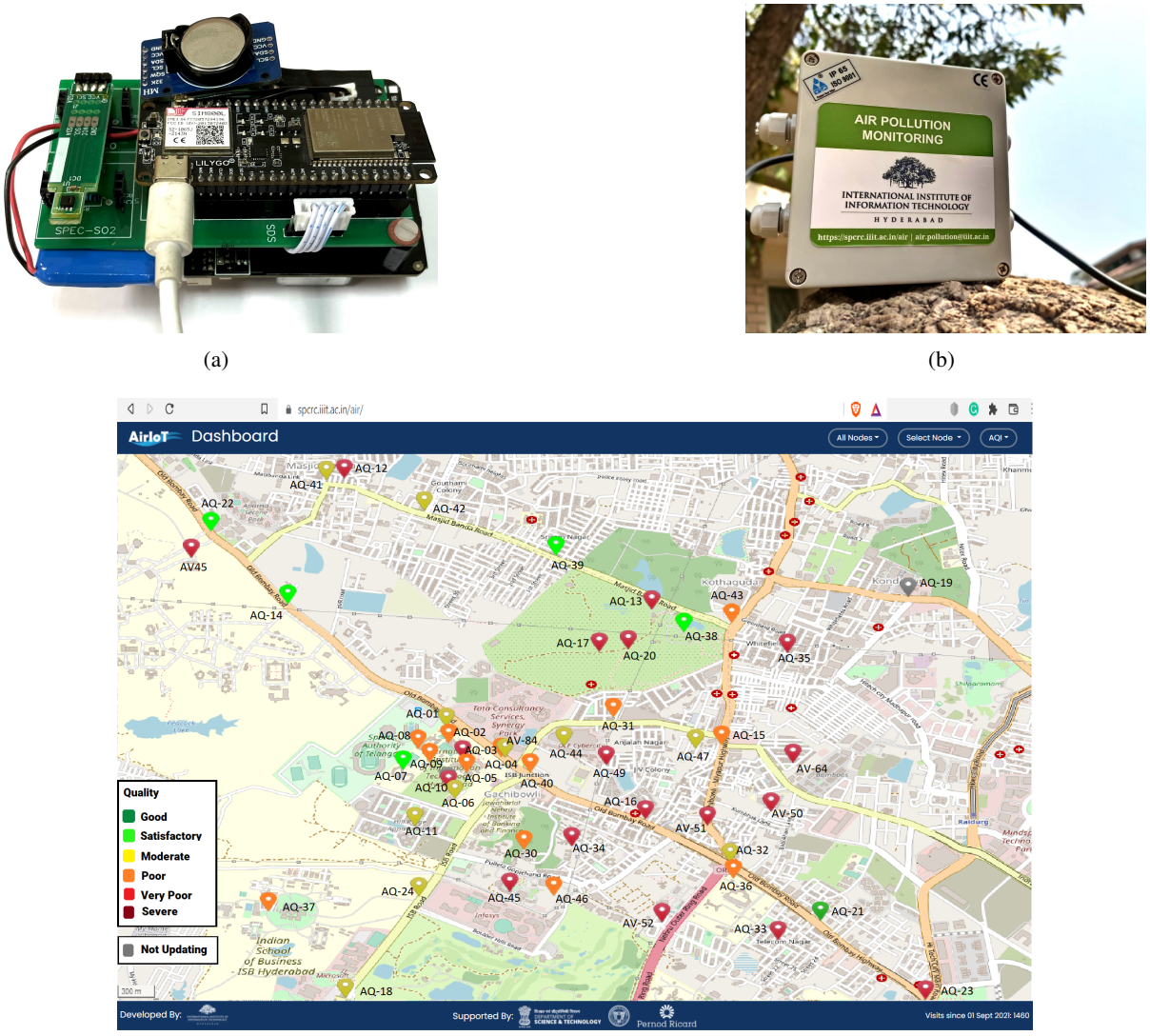

(a) (b)

(c)

Figure 5.2 Deployment of air pollution monitoring devices: (a) Circuit board and sensors (b) Developed device (c) Live data with locations on the map.

strategically placed to cover urban, semi-urban and green areas, as shown in Figure 5.2(c). Every device consists of the following components: a Nova SDS011 sensor for measuring the concentration of particulate matter (PM) with a diameter of 2.5 and 10 microns or less (PM2.5 and PM10), a Sensirion SHT21 sensor for measuring ambient temperature and humidity, a communication module (SIM800L and eSIM), a real-time clock (RTC), and a lithium polymer (LiPo) battery. These components are connected to an ESP-32 microcontroller that senses the data every 30 seconds and offloads to ThingSpeak, a cloud-based server. The device is powered through an AC-DC power adapter and a Li-Po battery, as shown in Figure 5.2(a). It is enclosed in an IP-65 box with dedicated inlets to facilitate the free ambient air flow and safeguard against environmental wear and tear, as shown in Figure 5.2(b).

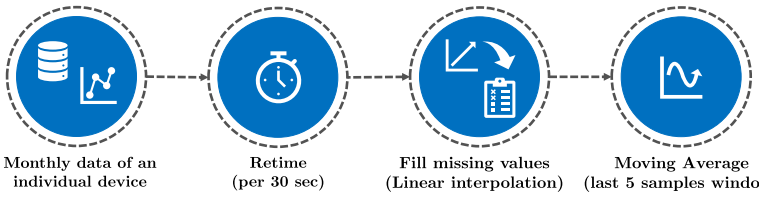

Figure 5.3 Preprocessing steps employed on the raw sensed data to fill missing values and avoid sensor noise.

The entire network was deployed in a phased-wise manner starting from Dec 2019. The air quality data of the region has been collected for more than three years. A comprehensive network and dataset analysis has been presented in [29, 151]. A subset of the dataset collected from November 2019 to January 2023 obtained from 49 devices is used in this work.

5.3.2 *Data preprocessing*

Every device offloads a vector of data points for every sensing instance in the following format:

- **device_id**: A unique identification number specific to every device.
- **created_at**: Time at which the sensor values are sensed in `"yyyy-MM-dd HH:mm:ss Z"` format.
- **PM10**: Concentration of PM10 in $\mu g\,m^{-3}$.
- **PM2.5**: Concentration of PM2.5 in $\mu g\,m^{-3}$.
- **RH**: Relative humidity values in terms of %.
- **Temp**: Temperature value in $^{\circ}C$.

The collected data was preprocessed following the steps shown in Figure 5.3. Although the devices are programmed to sense every 30 seconds, the entire dataset was re-sampled at 30 seconds to ensure that no timestamp in the time series is missed due to data loss. The missing values were filled utilizing a simple linear interpolation technique. As a last step, a moving average filter of window size five samples (2.5 minutes) was applied to replicate the usual practice of IoT devices to avoid spurious or noisy behaviour of the sensors. Figure 5.4 shows an example snapshot of the final time series data obtained for analysing the performance of the proposed access schemes in this chapter. The temperature and relative humidity (RH) values exhibit apparent periodicity, reflecting the predictable day-night cycles. In contrast, the PM concentration is largely aperiodic and lacks a distinct periodic pattern, indicating its reliance on anthropogenic activities. Also, the temperature and RH time series demonstrate minimal abrupt changes in values, maintaining a relatively steady trend. On the other hand, the PM time series displays numerous abrupt changes in concentration values, highlighting its sensitivity to dynamic and rapidly changing environmental factors.

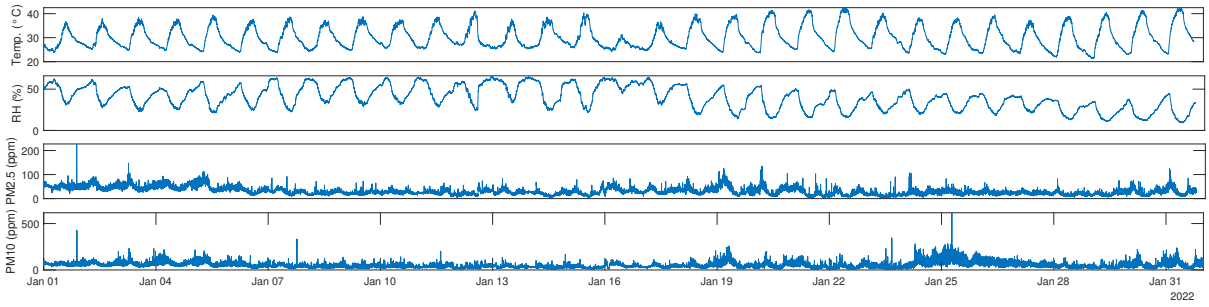

Figure 5.4 An example snapshot of the pre-processed time-series data collected from every device. This study is based on sensing of four parameters, namely Temperature (in °C), Relative Humidity (RH in %), concentration of PM2.5 (in ppm) and concentration of PM10 (in ppm). It can be observed that the temperature and RH values exhibit clear periodicity, depicting the day-night cycles; however, the PM concentration is largely aperiodic, depicting its dependency on anthropogenic activities. It is also worth noticing that the temperature and RH time series hardly encounter any abrupt change in values; however, the PM time series has many abrupt changes in concentration values.

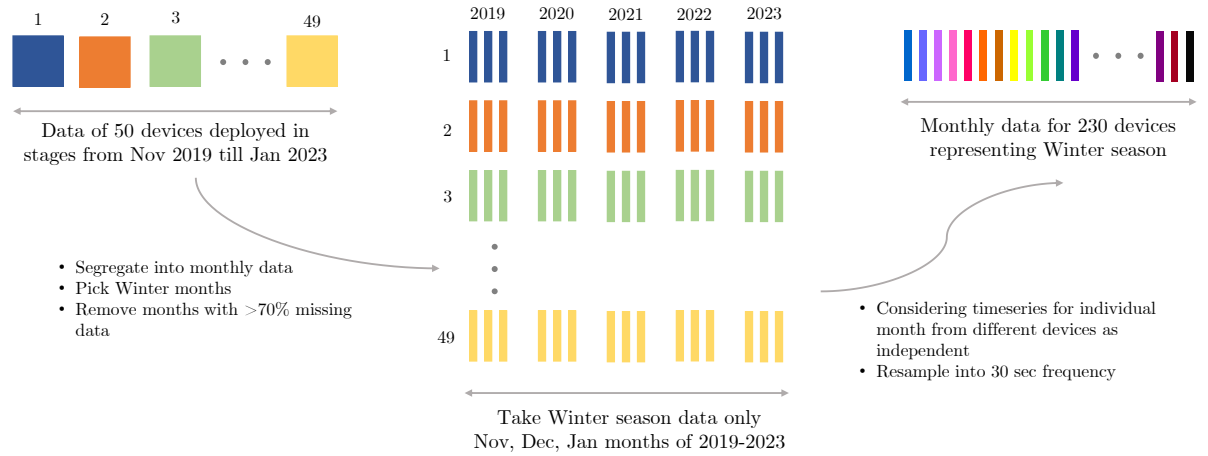

Figure 5.5 A visual representation of the process followed to create a monthly dataset virtually representing 230 devices, as utilized for this chapter.

5.3.3 *Dataset creation*

Figure 5.5 shows the process of creating the final dataset from the preprocessed data. Data from all the devices was divided into monthly chunks for each device. There have been instances of data loss primarily because the devices had to be returned to the lab for regular repair and maintenance. Additionally, the devices were brought for seasonal calibration at regular intervals and to make firmware upgrades. Hence, the data for months with more than 70% missing values was discarded. After that, the data was arranged monthly from 2019 to 2023. The data from November to January, representing the winter months in India, was then collected for this study. Since the PM has a high seasonal correlation, the analysis in this chapter has been restricted to one representative season only to avoid any seasonal

bias. The variations in all four parameters sensed in this study heavily depend on local anthropogenic activities. Therefore, the time series data for individual months from different devices can be considered independent and virtually treated as data from different devices. As a result, monthly data virtually representing 230 devices was curated for this study.

5.4 Transmission reduction schemes

In this work, multiple modes of operation for the IoT devices are envisioned to reduce data transmission from the devices, thus generating varied traffic patterns. Additionally, ML algorithms are proposed to decrease payload by excluding the transmission of strongly correlated parameters which can be predicted at the server. This approach diminishes reliance on variations in multiple parameters when implementing transmission reduction techniques, thus leading to higher gains. The proposed transmission reduction scheme and machine learning models are described below.

5.4.1 *Transmission reduction using Shewhart*

The Shewhart test for transmission reduction is a simple change detection algorithm [152]. Its ability to detect large changes and simple implementation makes it an attractive choice for IoT applications, as demonstrated in [140] and [141]. In Shewhart, newly sensed data is transmitted only if it differs from the previously transmitted value by more than a threshold. In other words, if x_t is the sensed data at t^{th} time instance, then a transmission is triggered if

$$\mid x_t - x_{\hat{t}} \mid > \tau, \tag{5.4}$$

where $x_{\hat{t}}$ is the last transmitted value and τ is the threshold. If a new value is not received at the server, the last received value is also considered to be the value at the current time instance. Therefore, the maximum error at the server is bounded by the threshold. The tolerable error usually governs the selection of threshold, transmission rate and the application at large.

5.4.2 *Machine learning-based prediction models for non-transmitted parameters*

Supervised ML algorithms can eliminate the need to transmit all the sensor values or parameters among a set of strongly correlated parameters. In this work, the concentration of PM2.5 is strongly correlated with the concentration of PM10 since, by definition, the concentration of PM10 also encompasses the concentration of PM2.5 pollutants. Hence, by transmitting PM10, the transmission of PM2.5 can be avoided, thus reducing the payload size. While the sensor data in our investigation comprises only four parameters, reducing a single parameter may not intuitively lead to a significant decrease in payload size. Nonetheless, the ML algorithms introduced in this thesis for payload reduction are designed with the broader context of IoT applications in mind, such as energy monitoring, which may

involve numerous parameters. In these diverse scenarios, payload reduction holds substantial advantages for enhancing the battery lifetime of devices, as demonstrated in Section 5.5.7 of this chapter. The traffic generated from the dataset employed in this chapter serves as a representative example in this context.

Predicting the concentration of PM2.5 based on the concentration of PM10 is a regression problem. Therefore, we propose using simple machine learning algorithms like linear regression [153], decision tree regression [154], and random forest (RF) [155] regression-based prediction of PM2.5 values using PM10 at the server. These algorithms have been selected based on their suitability for real-time deployment on cloud servers. A successful use-case of these ML algorithms in transmission reduction was demonstrated in [142].

- **Linear regression** is a statistical method used to model the relationship between a dependent variable and one or more independent variables by fitting a linear equation to observed data. The goal is to find the best-fitting line that minimizes the sum of the squared differences between the predicted and actual values. Linear regression is commonly employed for predictive analysis and understanding the correlation between variables.

- **Decision tree regression** is a machine learning algorithm for predicting continuous outcomes. It recursively partitions the dataset into subsets based on input features, forming a tree structure. Splits are chosen to minimize variance in predicted values. Hyperparameters, such as tree depth and minimum samples per leaf, influence the model's complexity and generalization ability. Decision tree regression is versatile and interpretable, making it helpful in understanding complex relationships in data and making predictions for regression tasks.

- **RF regression** is a supervised machine learning algorithm which can be used for both classification and regression tasks. It is essentially an ensemble of decision trees i.e. growing and combining multiple trees to produce a decision. In the case of regression, the outcome is the average of predictions made by individual trees. A decision tree, as the name suggests, is a tree or a flowchart-like structure that leads to an outcome based on the logical tests performed on features at every branching point. An RF regressor can be trained by tuning the hyper-parameters like the number of ensembles, maximum depth of the tree, minimum samples split and minimum samples leaf.

5.4.3 *Various modes of transmission*

In this study, Shewhart and ML-based transmission reduction schemes have been proposed in the form of various modes of transmission. While PM2.5 and PM10 are monitored as primary pollutants in this study, the AQI emerges as a widely recognized metric for conveying air pollution levels to the general public. Once PM2.5 and PM10 levels are known, AQI can be easily calculated both at the node and the server using the standard formula recommended by the Central Pollution Control Board (CPCB)

in India [156] as shown below:

$$\text{AQI} = \max(I_p),$$
$$\text{where, } I_p = \frac{I_{\text{HI}} - I_{\text{LO}}}{B_{\text{HI}} - B_{\text{LO}}}(C_p - B_{\text{LO}}) + I_{\text{LO}},$$

C_p is the pollutant concentration, and $p = 1, 2, 3, \cdots, n$ is the number of pollutants. Here, B_{HI} represent the breakpoint concentration greater or equal to the given concentration, B_{LO} is the given concentration, I_{HI} is the AQI value corresponding to B_{HI}, I_{LO} is the AQI value corresponding to B_{LO}.

This study uses different transmission modes based on specific use cases. The list of proposed modes of transmission and the corresponding schemes are as follows:

- **Mode 0**: Transmit all the parameters as soon they are sensed. This mode is representative of a baseline to compare the performance of all other proposed schemes.
- **Mode 1**: Apply Shewhart on all the parameters and transmit all of them if one or more parameters change significantly.
- **Mode 2**: Apply Shewhart on PM10 only and transmit only PM10 value to the server. When only PM10 is transmitted, the concentration of PM2.5 corresponding to every PM10 value is predicted using the ML algorithm at the server, and the AQI is calculated subsequently.
- **Mode 3**: Apply Shewhart on AQI only, however transmit PM10 if AQI changes significantly. The concentration of PM2.5 corresponding to every PM10 value is predicted using ML algorithms at the server, and AQI is calculated subsequently.

Mode 1 suits the scenarios demanding detailed data on all parameters, while for situations where only AQI information is needed, particularly in public information systems, and higher capacity is desired, either Mode 2 or Mode 3 can be employed.

5.5 Results and observations

In this section, we present the performance of the proposed access schemes with various transmission modes and compare them with the baseline method through different performance metrics. These metrics include the percentage reduction in transmission w.r.t the threshold in Shewhart, root mean squared error (RMSE) of the sensed parameters at the server, the average number of simultaneously transmitting nodes, collision probability during the access/contention phase of NB-IoT, the effective data received at the server within the visibility duration, and the expected battery lifetime. The RMSE and the reduction in transmissions represent the efficiency of the proposed scheme, while the other metrics represent its suitability for the LEO satellite scenario. The threshold values for Shewhart are carefully chosen, considering the sensor's accuracy tolerance and the nominal values of the sensed parameter in the specific environment. For instance, the Sensirion SHT21 sensor, employed for temperature and humidity

Table 5.2 List of parameters and their values utilized for performance analysis in this chapter.

Parameter	**Value**
LEO satellite altitude	600 km
Coverage type	Sparse constellation
System bandwidth	180 kHz
Sub-carrier width	3.75 kHz
No. of sub-carriers per RAO	48
RAO periodicity	160 ms
UL data rate	1.6 kbps
Shewhart threshold	Temp: 0.5°C, RH: 5%, AQI: 15 PM2.5: 5 ppm, PM10: 5 ppm
Sensing rate	30 sec
Back-off (BO)	$[0, 256 \cdot 2^i]$ sec, $i = 10$
Beam visibility window	246.9 sec (set-4)

sensing, exhibits an accuracy tolerance of $\pm 0.3°C$ and $\pm 2\%$, respectively. Since the temperature in Hyderabad, India, typically ranges between 10-20°C in winter, the thresholds for temperature and humidity are set at $0.5°C$ and 5%, respectively. Similarly, the Nova SDS011 sensor used for PM monitoring has a maximum accuracy tolerance of $\pm 15\%$ up to 10 ppm. Usually, PM2.5 ranges between 80 and 120 ppm, and PM10 ranges between 180 and 250 ppm during winter in Hyderabad. However, according to CPCB, 30 ppm for PM2.5 and 50 ppm for PM10 is categorised as "Good" [156]. Hence, a threshold of 5 ppm is selected for both PM2.5 and PM10 values to ensure that both the trend is captured and the data is reliable, even for the "Good" category with the least concentrations. Based on similar reasoning, given that an AQI between 50-100 is deemed satisfactory, a threshold of 15 index points is selected for AQI. Unless stated otherwise, all the system-level simulations have been performed using the parameters shown in Table 5.2.

5.5.1 *Performance of Shewhart in transmission reduction*

Initially, to demonstrate the working of Shewhart, an example implementation on a snapshot of a single time series for AQI is shown in Figure 5.6. The snapshot presented has a duration of 100 hours with a threshold of 15 index points. The reduction in transmission instances for the presented snapshot is nearly 99%, affirming the Shewhart scheme's efficacy. Notably, the plot illustrates a significant decrease in transmitted instances while accurately capturing the trendline and essential variations in AQI. This highlights the substantial benefits of integrating Shewhart for transmission reduction in this study.

Table 5.3 provides a comprehensive overview of the Shewhart scheme's performance across various modes of operation applied to the entire dataset. The results are evaluated in terms of transmission reduction, the number of simultaneously transmitting nodes, and the associated RMSE in the sensor values calculated at the server. It can be observed that all three modes with the proposed Shewhart-based

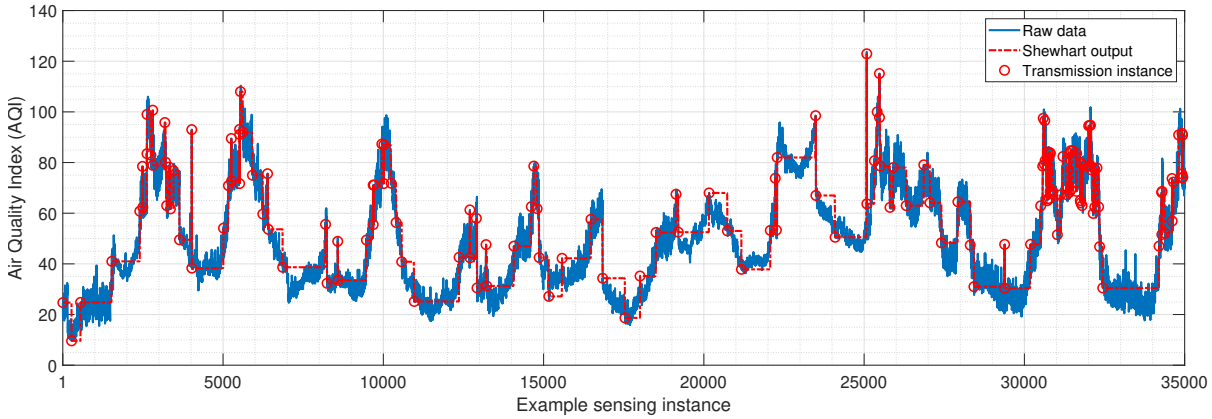

Figure 5.6 An example snapshot of Shewhart output at the server for AQI at a threshold of 15 index points for 100 hrs. The reduction in transmission for this snapshot is nearly 99%.

Table 5.3 Performance of various modes of operation in terms of the number of simultaneously transmitting nodes, % reduction and RMSE.

Transmission Mode		**Simultaneously Tx. Nodes**	**% Reduction**	**RMSE**	
M0	Baseline: Transmit all the parameters	230	0	0	
M1	Shewhart on all parameters	30	87.16	T: 0.16	RH: 0.62
				PM2.5: 1.29	PM10: 2.10
M2	Shewhart on PM10 only (transmit PM10 and predict PM2.5)	26	88.33	PM2.5: 2.34	PM10: 2.22
M3	Shewhart on AQI only (transmit PM10 and predict PM2.5, calculate AQI at the server)	8	96.54	PM2.5: 4.23	PM10: 7.56

access scheme produce a significant reduction in transmission. In Mode 1 and Mode 2, nearly 87-88% of transmissions are reduced, while in Mode 3, nearly 96% of transmissions are reduced. Notably, in Mode 1, the reduction percentage is less pronounced than in Mode 2 and Mode 3 due to the application of the Shewhart scheme to all four simultaneously varying time series. Even a sudden change in any parameter can trigger a new transmission. It can also be observed that Mode 2 also demonstrates a similar reduction percentage. This can be attributed to its tracking of PM10, where spurious changes are more prominent compared to the relatively smooth temperature and humidity data. It is noteworthy and encouraging to observe that an outstanding reduction in transmission is achieved with minimal error in the received information at the server. The RMSE values of 0.16°C for temperature and 0.62% for RH are negligible compared to both the nominal values of these parameters and the selected thresholds. This favourable trend extends to PM2.5 and PM10, with RMSE values of 2.34 and 2.22 ppm, respectively. These values are also negligible compared to the nominal values and do not significantly impact the calculation of the AQI, which is the ultimate marker of air pollution in general applications.

In Mode 3, a remarkable 96.54% reduction in transmissions and a decrease in simultaneously transmitting nodes from 230 to 8 are achieved. Shewhart is applied on AQI in Mode 3, which, being a

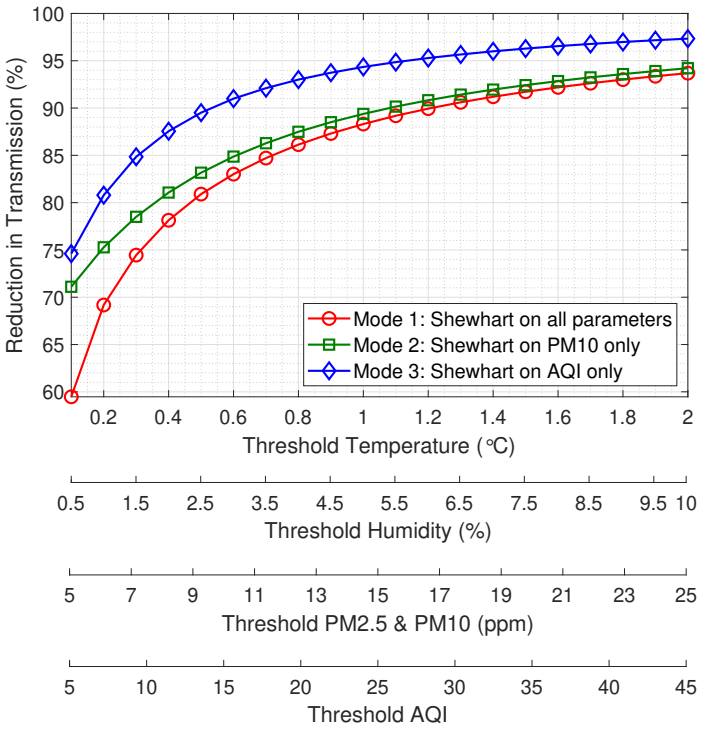

Figure 5.7 Average percentage reduction in transmission across the entire dataset as a function of varying thresholds for different transmission modes.

derived quantity, exhibits stability against minute fluctuations in PM values. This stabilizing effect is explained by the AQI calculations, as discussed in Section 5.4.3, where the AQI primarily depends on the breakpoints of PM concentration values and not on the specific value. The breakpoint concentrations for PM10 are Good (50), Satisfactory (100), Moderate (250), Poor (350), Very Poor (430) and Severe (430+). Similarly, the breakpoint concentrations for PM2.5 are Good (30), Satisfactory (60), Moderate (90), Poor (120), Very Poor (250) and Severe (250+). Hence, any fluctuations within these breakpoints do not change the AQI, making it a less fluctuating parameter. It can also be observed that the improved reduction in transmissions incurs only a nominal cost in terms of an increased RMSE. For Mode 3, even though AQI is tracked for Shewhart, PM10 values are transmitted, and AQI is calculated at the server. Hence, the RMSE is calculated for PM2.5 and PM10 to analyse the performance. In mode 3, the RMSE values of PM2.5 and PM10 are 2.43 ppm and 7.56 ppm, respectively, which is considerably lower than the nominal values observed during the winter season.

In Figure 5.7, the percentage reduction in transmission is illustrated for different thresholds across all proposed transmission modes. Notably, the reduction percentage sharply increases with higher thresholds, a pattern that aligns with expectations. Additionally, a comparison reveals that Mode 3 exhibits a relatively higher reduction percentage than Mode 1 and Mode 2, consistent with the previously explained reasons. Here, it is worth discussing the impact of a 96% reduction in transmission – it means sending only 4 out of every 100 newly sensed samples instead of sending all of them otherwise. As high-

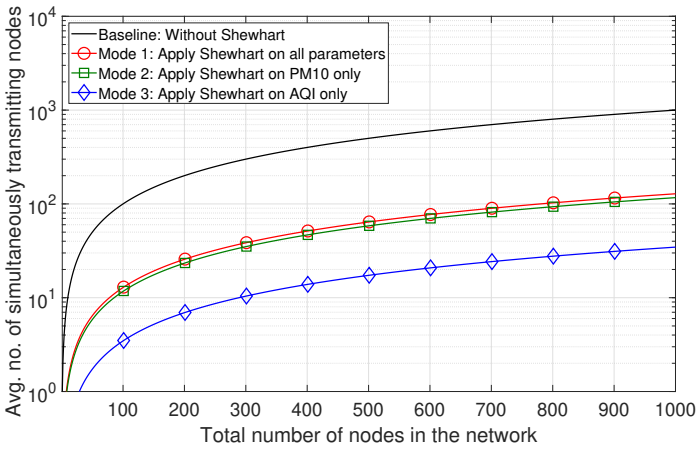

Figure 5.8 Comparison of avg. no. of simultaneously transmitting nodes relative to the total network size for different Shewhart transmission modes. A significant reduction of the order of 10^3 is achieved in Mode 3, while Modes 1 and 2 display a reduction of about ten times.

lighted in later KPIs, this reduction allows efficient use of resources, like bandwidth and limited access time during satellite visibility, for example, scheduling 96 more devices. If the Shewhart is applied to the entire network, scheduling 96 more devices would actually mean adding the capability to accommodate nearly 100 times more devices in the network with the same amount of resources. When viewed in conjunction with the RMSE reported above, this illustrates a significant boost in efficiency and capacity.

5.5.2 *Reduction in number of simultaneously transmitting nodes*

As the network size grows, Figure 5.8 displays the count of devices transmitting simultaneously using Shewhart. The results are extrapolated from the dataset using curve fitting to understand trends for larger networks. Notably, the number of simultaneously transmitting devices increases linearly with network size but significantly fewer in number with Shewhart when compared to the baseline scheme. For Mode 1 and Mode 2, this count is nearly ten times less than the actual devices in the network, equating to 10 out of 100 transmitting simultaneously. Mode 1 and Mode 2 exhibit similar performance, as explained earlier. Additionally, the reduction in simultaneously transmitting nodes follows an order of 10^2, i.e., 10 out of 1000 transmitting simultaneously for Mode 3. The result from this plot is crucial for examining other KPIs in larger networks. It serves as a tool to simulate the effects of the proposed transmission modes.

5.5.3 *Traffic pattern generated by Shewhart*

In the context of random access systems, traditional assumptions consider the arrival rate of new packets to follow a Poisson distribution, where the difference between subsequent arrivals is exponentially distributed. However, as evidenced in Figure 5.9, the actual distribution of the average time to the new transmission, based on the real dataset used (i.e. with Shewhart), deviates significantly from

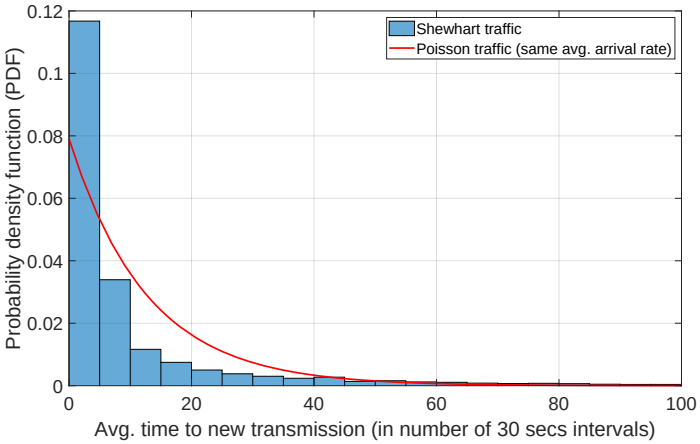

Figure 5.9 Comparison of probability density function between Shewhart-generated traffic and Poisson arrival assumption for the average time difference between successive transmissions. It can be observed that the Poisson assumption is incompatible with the Shewhart scheme, emphasizing the value of utilizing a real dataset.

Poisson traffic generated to match the average arrival rate. This emphasizes the utility of having a real dataset to generate traffic from a Shewhart-based access scheme rather than assuming Poisson arrival for system-level analysis.

The Poisson arrival process assumes that the inter-arrival time is independent of the last arrival. However, the traffic generated by Shewhart is contingent on factors such as the selection of thresholds and other parameters influencing the time series (environmental in this case). Thus, the arrival event and the inter-arrival times depend on the last arrival. Moreover, the Poisson model assumes that the number of sources is infinite, whereas in the Shewhart-based access scheme, the number of simultaneously transmitting sources is reduced drastically.

5.5.4 *Collision probability w.r.t offered traffic load*

In Figure 5.10, the collision probability is plotted against the average offered traffic, measured as simultaneously transmitting nodes during the access phase of NB-IoT for RAO with 160 ms periodicity and BO index of 10. The figure underscores the potential for increased load capacity by implementing the proposed access scheme to achieve a target collision probability. Notably, for a target collision probability of 0.4, while the baseline method supports only 57 devices, Mode 1 and 2 can accommodate nearly 450 devices, and Mode 3 can support close to 1650 devices. This is significant in the context of LEO satellite constellation, which allows handling a large number of users owing to large beam sizes. Moreover, the reduced collisions allow faster connections, which are crucial in the context of limited visibility. This also comes with advantages like reduced power consumption (due to fewer connection re-attempts) and lower congestion in the network.

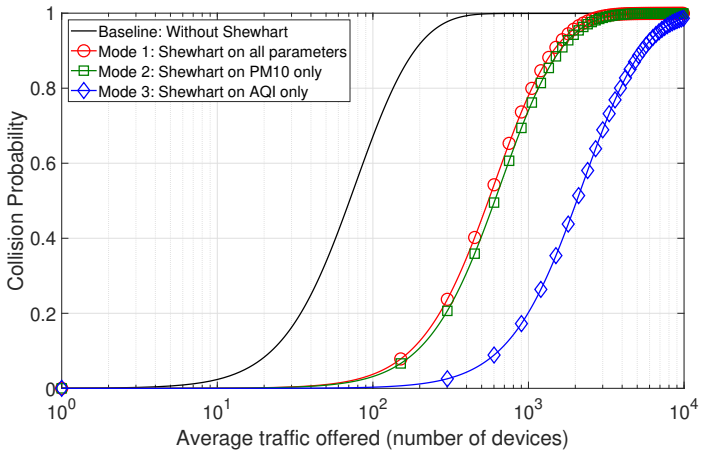

Figure 5.10 Collision probability versus average traffic offered in terms of simultaneously transmitting nodes in the access phase of NB-IoT for RAO with 160 ms periodicity and BO index of 10. The figure illustrates a substantial increase in the achieved load by implementing the proposed access scheme for a target collision probability.

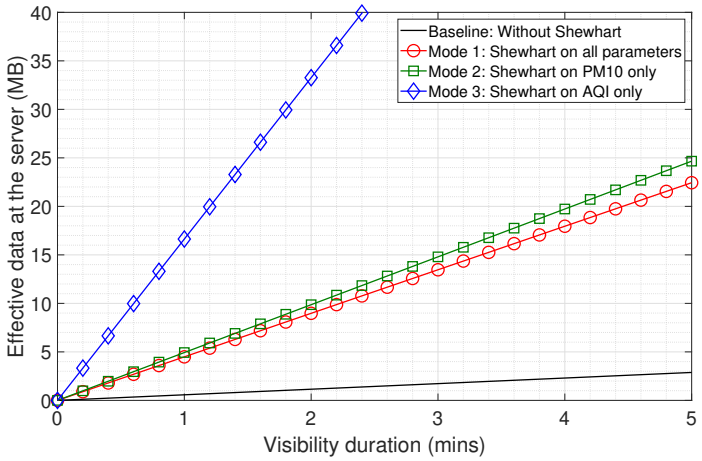

Figure 5.11 Effective data received at the server vs. the visibility duration of LEO satellite (in the data phase) for 180 kHz bandwidth, 3.75 kHz subcarrier, and 1.6 kbps data rate. Effective data encompasses information predicted at the server, including data not transmitted by the nodes due to Shewhart.

5.5.5 *Effective data at the server w.r.t visibility duration*

In Figure 5.11, the effective data received at the server is plotted against the increasing visibility duration of the LEO satellite in the data phase of NB-IoT communication. The plots are generated considering the link budget analysis presented in Section 2.5 of Chapter 2 for a bandwidth of 180 kHz, a subcarrier of 3.75 kHz, and a data rate of 1.6 kbps (representing the worst-case as per Set-4 configuration). The effective data is defined to encompass the data not transmitted by the nodes due to Shewhart but predicted at the server (i.e. considering the last received value to be the sensed value at the current instance). The results showcase that the Shewhart-based access schemes optimise the limited

Table 5.4 Performance of various regression models for predicting PM2.5 using PM10 at the server.

Model	**Configuration**	**RMSE (ppm)**	**R-Squared Validation**
Linear Regression	Ordinary least squares	2.1297	0.9808
Decision Tree Regressor	Max. depth = 10 Min samples split = 5	2.3587	0.9806
Random Forest Regressor	No. of estimators = 100 Max. depth = 10 Min. samples split = 5	2.0563	0.9835

visibility duration of LEO satellites by effectively communicating more information using the same number of transmissions as the baseline scheme. For example, in one minute, while the baseline scheme can communicate only 576 kB of data, Mode 1 and 2 can effectively offload 5 MB, and Mode 3 can offload 16 MB data to the server. Alternatively, the gain can also be viewed in terms of the reduced time required for offloading a target amount of data. For example, what Shewhart-based access modes can transmit in less than a minute would otherwise take 5 minutes in the baseline transmission method. This significant gain is valuable, particularly in LEO satellite-based scenarios with discontinuous coverage, where visibility duration is a crucial and limited resource. Even in scenarios with continuous coverage, such as mega-LEO constellations, Shewhart-based access schemes prove advantageous by reducing the required bandwidth to transmit target effective data.

5.5.6 *Performance of ML algorithms for parameter prediction*

Three machine learning-based algorithms—linear regression, decision tree regression, and RF regression were trained on the dataset to assess their effectiveness in predicting PM2.5 using PM10. Table 5.4 presents the average performance of these three schemes across the entire dataset, measured in terms of RMSE and R-squared validation, with the selected configuration of the algorithms. The training was performed using the standard *Sci-kit* learn implementation of these algorithms in Python. Given the heavy correlation in PM values, the performance of all three schemes is comparable. However, the RF outperforms the others with an RMSE of nearly 2 ppm, a negligible value when considering the nominal PM values in the winter season and the threshold set for Shewart-access schemes. While all three algorithms can be implemented on cloud servers in real-time, as validated in [142], considering computational complexity becomes pivotal in making the final implementation choice. Regarding computational complexity, linear regression is the simplest among the three, involving only two weight parameters to learn. Additionally, the ML schemes have a pivotal role in reducing the size of the payload (volume of data) to be transmitted since the transmission of correlated parameters can be avoided without losing any significant information. The impact of reduced payload due to these ML algorithms on the battery lifetime is analyzed in the subsequent subsection.

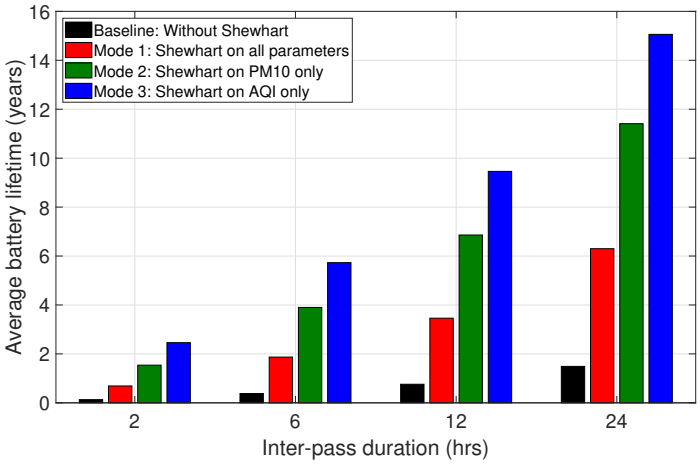

Figure 5.12 Estimated lifetime of a 5000 mWh battery for 164 dB MCL and 5-minute visibility duration per pass for various modes of operation. The inter-pass duration represents the period between two consecutive instances when the satellite becomes visible, and the IoT devices wake up for sensing and transmission. The devices remain in sleep mode when the satellite is not in the visible range.

Table 5.5 Power consumption assumptions for NTN-IoT energy consumption analysis [6].

State	**Operation**	**Duration (ms)**	**Power (mW)**
Reception (DL)	Sync, MIB, RAR Msg2, Msg4, UL grant, HARQ ACK, IP ACK, PDCCH monitoring,	371	90
Transmission (UL)	PRACH, RA Msg3 RAR, IP Report, HARQ ACK	50B UL: 335 200B UL: 1006	543
Idle (not in sleep)	MIB acquisition, waiting IP ACK, PRACH, ready timer, scheduling	22423	2.4
Power save (sleep)	Sleeping state when the satellite is not visible	based-on visibility	0.015
GNSS	GNSS reception	2000	37

5.5.7 *Expected battery life*

Figure 5.12 shows the expected average battery lifetime of a 5000 mWh battery under specific conditions, such as a maximum coupling loss (MCL) of 164 dB (worst-case scenario as per [6]), 5-minute satellite visibility per pass, and varying inter-pass durations within a sparse satellite constellation. Table 5.5 shows the time and power required for various operations in NB-IoT communication used for calculations in this section, as referred from [6]. Following the recommendations made by 3GPP in [6], assumptions made for calculations in this subsection include nodes possessing GNSS capabilities for accurate timing and frequency offset compensation, absence of simultaneous GNSS and NB-IoT opera-

Table 5.6 Average battery lifetime (in years) per device for MCL = 164 dB, 5 min visibility duration per pass and 5000 mWh battery.

Inter-pass duration (hrs)	Baseline	Mode 1	Mode 2		Mode 3	
			200B UL	50B UL	200B UL	50B UL
2	0.13	0.69	0.87	1.54	1.60	2.46
6	0.38	1.87	2.23	3.90	3.67	5.73
12	0.76	3.46	4.04	6.86	6.23	9.46
24	1.49	6.30	7.18	11.41	10.62	15.06

tions, no re-transmissions, and negligible power consumption in reading satellite ephemeris information. The inter-pass duration represents the period between two consecutive instances when the satellite becomes visible in a constellation with discontinuous coverage. The IoT devices wake up for sensing and transmission only when the satellite is visible and remain in sleep mode otherwise.

Figure 5.12 highlights that modes incorporating Shewhart exhibit significantly prolonged battery lifetimes compared to the baseline mode without Shewhart. In this figure, Mode 1 has a payload of 200 bytes while Mode 2 and Mode 3 have a payload of 50 bytes, considering that only a few parameters are transmitted, and the others can be predicted using ML algorithms on the server. The estimated enhancement in battery lifetime, coupled with the capacity to accommodate more devices, underscores the viability of the proposed Shewhart-based access scheme. Additionally, extending the inter-pass duration is observed to increase battery lifetime further, with improvements ranging from nearly two times to three times across different modes as the duration increases from 2 to 6 hours.

Table 5.6 shows the battery lifetime of all transmission modes, distinguishing between a full 200-byte payload and a reduced 50-byte payload. Notably, in Mode 2, reducing the payload leads to a 1.7-fold increase in battery life across all inter-pass durations, emphasizing the effectiveness of the proposed ML algorithms in payload reduction. Similarly, in Mode 3, a 1.5-fold improvement in battery lifetime is observed with a reduced payload.

5.6 Summary

This chapter introduced an efficient access scheme tailored for LEO satellite-based NB-IoT networks, employing a constellation with intermittent coverage and analysing data from a real-world IoT testbed. The analysis reveals distinctive traffic characteristics in the proposed Shewhart-based access scheme, deviating from the commonly assumed Poisson arrivals in random access scenarios. Notably, the Shewhart traffic significantly reduces the number of simultaneously transmitting nodes and associated collision probability compared to the baseline without transmission reduction. This translates to a significant increase in network capacity, accommodating more nodes while meeting collision probability targets. Despite the reduced transmissions, the Shewhart-based scheme delivers a significantly larger

effective data volume at the server. Additionally, integrating machine learning algorithms for payload reduction substantially extends the battery lifetimes of the IoT devices. Consequently, the proposed Shewhart-based access scheme, combined with ML algorithms, emerges as a compelling solution for addressing the challenges of limited visibility, low data rates, and energy constraints in satellite-based IoT networks.

Chapter 6

Conclusion

The IoT has emerged as a transformative technology, reshaping our interactions with the environment. From smart homes to extensive applications in smart cities and e-agriculture, IoT networks are at the forefront of technological advancements. The connectivity requirements of IoT networks differ from the traditional cellular applications. In IoT, the focus is on serving a massive number of users, often deployed at remote locations but with low data rates. Studies show that existing terrestrial networks can cover only 25% of the landmass. Satellites with direct access can extend coverage to unserved areas with minimal additional ground infrastructure. *This thesis extensively explores the roles and use cases of satellites within IoT networks, highlighting the significant potential of mega LEO constellations, direct-access topology and intelligent transmission schemes*.

A star-of-star topology for satellite IoT is proposed, which can facilitate IoT devices to broadcast their sensed data to all the visible satellites without prior coordination and sleep thereafter. The ground station coherently combines signals from multiple satellites, offering spatial diversity. A tractable analytical framework for physical layer performance analysis of the proposed topology was studied. Initially, a simple scenario with a fixed visible number of satellites and no interference from other users was considered. It was demonstrated that a desirable outage probability between 10^{-2} to 10^{-5} can be achieved through a mega-LEO constellation using 3-6 satellites that would be visible at latitudes where the majority of the world's population is located. Two combining schemes, selection combing and MRC, were analysed, both of which achieve a diversity order equal to the number of satellites used for forwarding. However, the MRC is shown to achieve better coverage compared to the selection combining, owing to its coding gain, which is higher than SC by a factor of $\Gamma(S+1)$.

Further, the performance analysis was extended with realistic assumptions to encompass varying satellite locations, interference from multiple users and errors due to imperfect channel knowledge. Stochastic modelling of the satellite locations was done, considering the satellites are distributed to form a BPP around a sphere. For a fixed mask elevation angle, the distribution of the distance between the user and the satellite was derived, which follows a ramp-like function. Meanwhile, the number of visible satellites follows a binomial probability. It is demonstrated that for a practical transmit power between 20-23 dBm and using 5 satellites for relaying, the IoT devices can achieve an OP between 10^{-2} to 10^{-3} while using CM and SIC-based decoding in the presence of interference. Similarly,

the feasibility of the proposed topology has been shown with respect to other system parameters, like number of satellites, number of users, mask angle and constellation size. The analysis also shows that in a multi-user scenario, trading off the throughput and desired OP, the initial few users can be decoded using CM, thus reducing the decoding complexity. However, for applications requiring the decoding of more users, SIC is preferable. Asymptotic analysis on OP has also been carried out under high SNR assumption. The derived expressions were used to optimise system parameters. As an illustration, when considering a constellation of 720 satellites and users with a 20 dB transmit power, around 118 users can be efficiently supported using CM decoding to achieve a target OP of 10^{-3}. This optimal support is achieved by employing 15 satellites at a 10.5-degree elevation angle. However, the number of supported users decreases to 44 if the constellation comprises only 480 satellites. Comparable approximations can be derived for SIC decoding as well. All the theoretical analysis was rigorously validated through simulations.

An efficient transmission scheme tailored for LEO satellite-based IoT networks was also presented. A constellation with intermittent coverage was considered, and data from a real-world IoT testbed was analysed. Transmission reduction using Shewhart, a change detection technique, was utilized to significantly reduce the number of simultaneously transmitting nodes. Various modes of transmission were proposed based on different application scenarios. For example, in Mode 1 and Mode 2, Shewhart is applied to either all sensor data or prominently varying PM10 data. A reduction of nearly 87-88% of transmissions is achieved in Mode 1 and Mode 2. In Mode 3, Shehwart is applied a derived quantity, which led to a reduction of nearly 96% in transmissions. This translates to a significant increase in network capacity, accommodating more nodes while meeting collision probability targets. For example, aiming for a collision probability of 0.4, the baseline method can support only 57 devices. In contrast, Modes 1 and 2 can accommodate nearly 450 devices, and Mode 3 can support close to 1,650 devices. This holds particular importance within the framework of LEO satellite constellations, where the capacity to handle a large number of users is facilitated by substantial beam sizes. Additionally, the reduction in collisions enables faster connections, a crucial aspect in environments with limited visibility. This also brings about advantages such as reduced power consumption (due to fewer connection re-attempts) and reduced congestion in the network. There was also a substantial increase in the effective data offloaded to the server. Additionally, various ML algorithms were proposed to reduce the payload of transmitted data, thereby reducing dependency on multiple parameters. This reduction contributes to a significant decrease in transmissions and energy savings during the transmission of small packets. It is shown that reducing the payload results in a 1.7-fold increase in battery life across all inter-pass durations in Mode 2. Similarly, a 1.5-fold improvement in battery lifetime is observed with a reduced payload in Mode 3.

The key benefit of the proposals made in this thesis lies in their simplicity, as they enable seamless connection of IoT devices and facilitate burst transmissions at specific intervals when the satellites are visible. The proposed topology, coupled with the proposed transmission scheme, emerges as a compelling solution for addressing the challenges of link budget, limited visibility, low data rates, and energy constraints in satellite-based IoT networks. The results presented in this research provide valu-

able insights for establishing baseline requirements necessary to achieve desired performance levels in satellite IoT networks. Notably, this thesis represents a unique contribution as it presents rigorous mathematical analysis and insights from actual field deployment.

In the future, there is a tremendous scope for expanding the analysis conducted in this thesis. A fine-grained analysis can be done on the PHY layer utilizing meta-distributions (MD). The MD of SINR represents the complementary CDF of the conditional coverage probability for given satellite positions. The probability that a specific proportion of links are able to achieve a known threshold SINR can be analyzed using MD. Also, aspects related to Doppler estimation and compensation can also be included in this analysis. Similarly, on the MAC layer, the analysis can be extended to understand the effect of repetitions in case of collisions. Moreover, a mathematical framework can be developed to model the traffic pattern generated by the proposed transmission scheme.

The results in this thesis can be broadened to encompass an integrated network that optimally serves users through a combination of terrestrial and satellite networks, representing an integrated network. A novel addition can be incorporating inter-satellite links into the existing analysis, considering that some commercial constellations have already equipped satellites with laser inter-satellite links.

Looking at the broader picture, given ISRO's recent accomplishments in deep space missions and the growing accessibility of commercial launch vehicles, India is well-positioned to dominate the satellite platform market with hosted payloads. The research in this thesis provides a foundation, demonstrating the feasibility of developing payloads and end devices for satellite IoT.

Bibliography

[1] R. Lorrain, "Inside out - Semtech's corporate blog: LoRa delivering internet of things capabilities worldwide," (Accessed 15 Oct. 2022). [Online]. Available: https://blog.semtech.com/lora-delivering-internet-of-things-capabilities-worldwide (Cited on page 1.)

[2] Z. Qu, G. Zhang, H. Cao, and J. Xie, "LEO satellite constellation for internet of things," *IEEE Access*, vol. 5, pp. 18 391–18 401, 2017. (Cited on pages 1 and 7.)

[3] G. Giambene, S. Kota, and P. Pillai, "Satellite-5G integration: A network perspective," *IEEE Network*, vol. 32, no. 5, pp. 25–31, 2018. (Cited on page 1.)

[4] Y. Guan, F. Geng, and J. H. Saleh, "Review of high throughput satellites: Market disruptions, affordability-throughput map, and the cost per bit/second decision tree," *IEEE Aerospace and Electronic Systems Magazine*, vol. 34, no. 5, pp. 64–80, 2019. (Cited on page 1.)

[5] I. Portillo, B. G. Cameron, and E. F. Crawley, "A technical comparison of three low earth orbit satellite constellation systems to provide global broadband," *Acta Astronautica*, vol. 159, pp. 123 – 135, 2019. (Cited on pages 2 and 49.)

[6] 3rd Generation Partnership Project (3GPP); Technical Specification Group Radio Access Network, "Study on NB-IoT/eMTC support for Non-Terrestrial Networks (NTN) (Rel 17)," *TR 36.763V17.0.0*, 2021. (Cited on pages xv, 2, 16, 26, 28, 32, 50, 51, 74, 75, 89, and 104.)

[7] M. Centenaro, C. E. Costa, F. Granelli, C. Sacchi, and L. Vangelista, "A survey on technologies, standards and open challenges in satellite IoT," *IEEE Communications Surveys Tutorials*, vol. 23, no. 3, pp. 1693–1720, 2021. (Cited on pages 2 and 7.)

[8] M. Vaezi *et al.*, "Cellular, wide-area, and non-terrestrial IoT: A survey on 5G advances and the road toward 6G," *IEEE Communications Surveys Tutorials*, vol. 24, no. 2, pp. 1117–1174, 2022. (Cited on pages 2 and 7.)

[9] S. Kota *et al.*, "Satellite: International network generations roadmap," *IEEE Future Networks World Forum (FNWF)*, pp. 1–182, 2022. (Cited on pages 2 and 32.)

[10] J. M. de Souza Sant'Ana, A. Hoeller, R. D. Souza, H. Alves, and S. Montejo-Sánchez, "LoRa performance analysis with superposed signal decoding," *IEEE Wireless Communications Letters*, vol. 9, no. 11, pp. 1865–1868, 2020. (Cited on pages 3, 51, and 52.)

[11] U. Noreen, L. Clavier, and A. Bounceur, "LoRa-like CSS-based PHY layer, capture effect and serial interference cancellation," in *24th Europian Wireless Conference*, 2018, pp. 1–6. (Cited on pages 3, 51, and 52.)

[12] C. C. Chan, B. Al Homssi, and A. Al-Hourani, "A stochastic geometry approach for analyzing uplink performance for IoT-over-satellite," in *IEEE International Conference Communications*, 2022. (Cited on pages 3, 51, and 52.)

[13] H. Lin, C. Zhang, Y. Huang, R. Zhao, and L. Yang, "Fine-grained analysis on downlink LEO satellite-terrestrial mmwave relay networks," *IEEE Wireless Communications Letters*, vol. 10, no. 9, pp. 1871–1875, 2021. (Cited on pages 3, 51, 52, and 62.)

[14] D.-H. Na, K.-H. Park, Y.-C. Ko, and M.-S. Alouini, "Performance analysis of satellite communication systems with randomly located ground users," *IEEE Transactions on Wireless Communications*, vol. 21, no. 1, pp. 621–634, 2022. (Cited on pages 3 and 52.)

[15] N. Okati, T. Riihonen, D. Korpi, I. Angervuori, and R. Wichman, "Downlink coverage and rate analysis of low earth orbit satellite constellations using stochastic geometry," *IEEE Transactions on Communications*, vol. 68, no. 8, pp. 5120–5134, 2020. (Cited on pages 3, 51, 52, 60, 74, and 75.)

[16] N. Okati and T. Riihonen, "Nonhomogeneous stochastic geometry analysis of massive LEO communication constellations," *IEEE Transactions on Communications*, vol. 70, no. 3, pp. 1848–1860, 2022. (Cited on pages 3, 51, and 52.)

[17] Qusay F. Hassan (Editor), *Internet of Things A to Z: Technologies and Applications*. John Wiley & Sons, 2018. (Cited on page 7.)

[18] M. A. Iqbal, S. Hussain, H. Xing, and M. A. Imran, *Enabling the Internet of Things: Fundamentals, Design and Applications*. John Wiley & Sons, 2021. (Cited on page 7.)

[19] R. Kamal, *Internet of Things*, 2nd ed. McGraw Hill Education, 2022. (Cited on page 7.)

[20] A. K. Maini and V. Agrawal, *Satellite Technology: Principles and applications*, 2nd ed. John Wiley & Sons Ltd, 2011. (Cited on pages 7 and 24.)

[21] T. Pratt and J. E. Allnutt, *Satellite Communications*, 3rd ed. John Wiley & Sons, Dec. 2019. (Cited on pages 7 and 23.)

[22] G. Maral, M. Bousquet, and Z. Sun, *Satellite communications systems: systems, techniques and technology*. John Wiley & Sons, 2020. (Cited on pages 7 and 19.)

[23] Eva Lagunas, Symeon Chatzinotas, Kang An, Bassel F. Beidas (Eds.), *Non-Geostationary Satellite Communications Systems*. The Institution of Engineering and Technology, 2022. (Cited on page 7.)

[24] O. Kodheli *et al.*, "Satellite communications in the new space era: A survey and future challenges," *IEEE Communications Surveys & Tutorials*, vol. 23, no. 1, pp. 70–109, 2021. (Cited on pages xi, 7, 16, 17, and 23.)

[25] Bharat S. Chaudhari and Marco Zennaro (Eds.), *LPWAN Technologies for IoT and M2M Applications*. Academic Press, 2023. (Cited on page 7.)

[26] R. Herrero, *Practical Internet of Things Networking: Understanding IoT Layered Architecture*. Springer, 2023. (Cited on page 7.)

[27] A. Kirimtat, O. Krejcar, A. Kertesz, and M. F. Tasgetiren, "Future trends and current state of smart city concepts: A survey," *IEEE access*, vol. 8, pp. 86 448–86 467, 2020. (Cited on page 8.)

[28] A. S. Syed, D. Sierra-Sosa, A. Kumar, and A. Elmaghraby, "IoT in smart cities: A survey of technologies, practices and challenges," *Smart Cities*, vol. 4, no. 2, pp. 429–475, 2021. (Cited on page 8.)

[29] A. Parmar, S. Sara, A. Dwivedi, R. R. Chinthalapani, I. Patwardhan, S. Bijjam *et al.*, "Development of end-to-end low-cost IoT system for densely deployed PM monitoring network: An indian case study," *arXiv:2211.16497 preprint*, 2022. (Cited on pages 8 and 92.)

[30] R. Bose, S. Gujar, A. K. Dwivedi, K. Vemuri, and S. Chaudhari, "Comparative analysis of construction-related air pollution in indoor and outdoor environment," in *11th International Conference on Environment Pollution and Prevention (ICEPP 2023)*, 2023. (Cited on page 8.)

[31] S. Sara *et al.*, "The application of mobile sensing to detect CO and NO2 emission spikes in polluted cities," *IEEE Access*, vol. 11, pp. 79 624–79 635, 2023. (Cited on page 8.)

[32] ——, "Protocol for hunting PM2.5 emission hot spots in cities," in *Proceedings of the 1st International Workshop on Advances in Environmental Sensing Systems for Smart Cities*, 2023, pp. 37–42. (Cited on page 8.)

[33] S. Deb, A. K. Dwivedi, S. Chaudhari, and K. Rajan, "Spatial factor analysis of mobile IoT data: A case study on PM across india," in *IGARSS 2022 - 2022 IEEE International Geoscience and Remote Sensing Symposium*, 2022, pp. 1272–1275. (Cited on page 8.)

[34] A. K. Lall, A. Khandelwal, N. Nilesh, and S. Chaudhari, "Improving IoT-based smart retrofit model for analog water meters using DL based algorithm," in *2022 9th International Conference on Future Internet of Things and Cloud (FiCloud)*, 2022, pp. 207–212. (Cited on page 8.)

[35] A. K. Lall, A. Khandelwal, R. Bose, N. Bawankar, N. Nilesh, A. Dwivedi, and S. Chaudhari, "Making analog water meter smart using ML and IoT-based low-cost retrofitting," in *2021 8th International Conference on Future Internet of Things and Cloud (FiCloud)*, 2021, pp. 157–162. (Cited on page 8.)

[36] S. Gahlot, S. R. N. Reddy, and D. Kumar, "Review of smart health monitoring approaches with survey analysis and proposed framework," *IEEE Internet of Things Journal*, vol. 6, no. 2, pp. 2116–2127, 2019. (Cited on page 8.)

[37] F. Alshehri and G. Muhammad, "A comprehensive survey of the internet of things (IoT) and AI-based smart healthcare," *IEEE Access*, vol. 9, pp. 3660–3678, 2021. (Cited on page 8.)

[38] K. S. Viswanadh, O. Kathalkar, P. Vinzey, N. Nilesh, S. Chaudhari, and V. Choppella, "CV and IoT-based remote triggered labs: Use case of conservation of mechanical energy," in *2022 9th International Conference on Future Internet of Things and Cloud (FiCloud)*, 2022, pp. 100–106. (Cited on page 8.)

[39] A. Das, K. S. Viswanadh, R. Agrawal, A. Gureja, N. Nilesh, and S. Chaudhari, "Using miniature setups and partial streams for scalable remote labs," in *IEEE 10th International Conference on Future Internet-of-Things and Cloud, 2023 (FiCloud-2023)*, 2023. (Cited on page 8.)

[40] O. Friha, M. A. Ferrag, L. Shu, L. Maglaras, and X. Wang, "Internet of things for the future of smart agriculture: A comprehensive survey of emerging technologies," *IEEE/CAA Journal of Automatica Sinica*, vol. 8, no. 4, pp. 718–752, 2021. (Cited on page 9.)

[41] A. D. Boursianis *et al.*, "Internet of things (IoT) and agricultural unmanned aerial vehicles (UAVs) in smart farming: A comprehensive review," *Internet of Things*, vol. 18, p. 100187, 2022. (Cited on page 9.)

[42] N. Nilesh, I. Patwardhan, J. Narang, and S. Chaudhari, "IoT-based AQI estimation using image processing and learning methods," in *2022 IEEE 8th World Forum on Internet of Things (WF-IoT)*, 2022, pp. 1–5. (Cited on page 13.)

[43] N. Nilesh, J. Narang, A. Parmar, and S. Chaudhari, "IoT and ML-based AQI estimation using real-time traffic data," in *2022 IEEE 8th World Forum on Internet of Things (WF-IoT)*, 2022, pp. 1–6. (Cited on page 13.)

[44] oneM2M, "oneM2M IoT standard," (Accessed 20 Dec. 2023). [Online]. Available: https://www.onem2m.org/ (Cited on page 13.)

[45] G. Ihita, K. Viswanadh, Y. Sudhansh, S. Chaudhari, and S. Gaur, "Security analysis of large scale IoT network for pollution monitoring in urban india," in *2021 IEEE 7th World Forum on Internet of Things (WF-IoT)*, 2021, pp. 283–288. (Cited on page 13.)

[46] G. Ihita, V. Acharya, L. Kanigolla, S. Chaudhari, and T. Monteil, "Security for oneM2M-based smart city network: An OM2M implementation," in *2023 15th International Conference on COMmunication Systems & NETworkS (COMSNETS)*, 2023, pp. 808–813. (Cited on page 13.)

[47] U. Raza, P. Kulkarni, and M. Sooriyabandara, "Low power wide area networks: An overview," *IEEE Communications Surveys & Tutorials*, vol. 19, no. 2, pp. 855–873, 2017. (Cited on page 13.)

[48] Unabiz Technology, "Sigfox," (Accessed 12 Dec. 2023). [Online]. Available: https://www.sigfox.com/ (Cited on page 13.)

[49] Sigfox, "Sigfox Technical Overview," (Accessed 12 Dec. 2023). [Online]. Available: https://www.ismac-nc.net/wp/wp-content/uploads/2017/08/sigfoxtechnicaloverviewjuly2017-170802084218.pdf (Cited on page 13.)

[50] Semtech, "What are LoRa and LoRaWAN ?" (Accessed 12 Dec. 2023). [Online]. Available: https://lora-developers.semtech.com/documentation/tech-papers-and-guides/lora-and-lorawan/ (Cited on page 14.)

[51] LoRa Alliance, "LoRaWAN Specification v1.1," (Accessed 12 Dec. 2023). [Online]. Available: https://resources.lora-alliance.org/technical-specifications/lorawan-specification-v1-1 (Cited on page 14.)

[52] Semtech Coorp., *AN1200.22 LoRa Modulation Basics*. Camarillo, CA, USA, 2015, (Accessed 15 Oct. 2022). [Online]. Available: https://www.frugalprototype.com/wp-content/uploads/2016/08/an1200.22.pdf (Cited on pages 14 and 58.)

[53] K. Mekki, E. Bajic, F. Chaxel, and F. Meyer, "Overview of cellular LPWAN technologies for IoT deployment: Sigfox, LoRaWAN, and NB-IoT," in *2018 IEEE International Conference on Pervasive Computing and Communications Workshops (PerCom Workshops)*, 2018, pp. 197–202. (Cited on pages xv and 15.)

[54] B. S. Chaudhari, M. Zennaro, and S. Borkar, "LPWAN technologies: Emerging application characteristics, requirements, and design considerations," *Future Internet*, vol. 12, no. 3, p. 46, 2020. (Cited on pages xv and 15.)

[55] M. Kanj, V. Savaux, and M. Le Guen, "A tutorial on NB-IoT physical layer design," *IEEE Communications Surveys & Tutorials*, vol. 22, no. 4, pp. 2408–2446, 2020. (Cited on page 14.)

[56] Spaceflight Now, "Spacex falcon 9 rocket launches 23 starlink satellites from cape canaveral," *Spaceflight Now Inc*, Dec 12, 2023. [Online]. Available: https://spaceflightnow.com/2023/11/27/live-coverage-spacex-falcon-9-rocket-to-launch-from-cape-canaveral-on-starlink-mission/ (Cited on page 15.)

[57] M. Giordani and M. Zorzi, "Non-terrestrial networks in the 6G era: Challenges and opportunities," *IEEE Network*, vol. 35, no. 2, pp. 244–251, 2021. (Cited on page 16.)

[58] B. Di, L. Song, Y. Li, and H. V. Poor, "Ultra-dense LEO: Integration of satellite access networks into 5G and beyond," *IEEE Wireless Communications*, vol. 26, no. 2, pp. 62–69, 2019. (Cited on page 16.)

[59] 3rd Generation Partnership Project (3GPP); Technical Specification Group Services and System Aspects, "Study on satellite access Phase 3 (Rel 19)," *TR 22.865V19.1.0*, 2023. (Cited on page 16.)

[60] E. Pasqua and S. Sinha, "Satellite IoT market report 2022-2026," *IoT Analytics GmbH, Germany*, 2022, (Accessed 28 May 2023). [Online]. Available: https://iot-analytics.com/product/satellite-iot-market-report-2022-2026/ (Cited on page 17.)

[61] R. G. Gopal and N. B. Ammar, "Framework for unifying 5G and next generation satellite communications," *IEEE Network*, vol. 32, no. 5, pp. 16–24, 2018. (Cited on page 17.)

[62] International Telecommunication Union (ITU), "Final Acts WRC-19," *World Radiocommunication Conference*, 2019, (Accessed 16 Dec. 2023). [Online]. Available: https://www.itu.int/en/publications/ITU-R/pages/publications.aspx?parent=R-ACT-WRC.14-2019&media=paper (Cited on page 19.)

[63] O. Montenbruck, *Satellite orbits: models, methods, and applications*. New York: Springer, 2000. (Cited on page 19.)

[64] V. A. Chobotov, *Orbital mechanics*, 3rd ed. Education Series: American Institute of Aeronautics and Astronautics, Inc., 2002. (Cited on page 19.)

[65] E. Aboutanios, "Frequency estimation for low earth orbit satellites," Ph.D. dissertation, Faculty of Engineering (TeleCommunications Group), Univ. of Technology, Sydney, 2002. (Cited on pages 20 and 56.)

[66] I. Ali, N. Al-Dhahir, and J. E. Hershey, "Doppler characterization for LEO satellites," *IEEE Transactions on Communications*, vol. 46, no. 3, pp. 309–313, 1998. (Cited on pages xi, 20, 21, and 22.)

[67] Jionghui Li *et al.*, "Fast tracking doppler compensation for OFDM-based LEO satellite data transmission," *IEEE International Conference on Computer and Communications (ICCC)*, pp. 1814–1817, 2016. (Cited on pages 22 and 36.)

[68] O. Kodheli, S. Andrenacci, N. Maturo, S. Chatzinotas, and F. Zimmer, "Resource allocation approach for differential doppler reduction in NB-IoT over LEO satellite," *9th Advanced Satellite Multimedia Systems Conference and the 15th Signal Processing for Space Communications Workshop (ASMS/SPSC)*, pp. 1–8, 2018. (Cited on pages 22 and 36.)

[69] N. A. J. Fraire, S. Céspedes, "Direct-to-satellite IoT - a survey of the state of the art and future research perspectives: Backhauling the IoT through LEO satellites," *ADHOC-NOW: Ad-Hoc, Mobile, and Wireless Networks*, pp. 241–258, 2019. (Cited on pages xi, 24, and 50.)

[70] Lacuna Space, "An ultra-low cost sensor service for small amounts of data," (Accessed 15 Oct. 2022). [Online]. Available: https://lacuna.space/ (Cited on pages 24, 35, 50, and 57.)

[71] Kepler Space, "Kepler's IoT development kit (everywhereIoT™)." [Online]. Available: https://kepler.space/ (Cited on pages 24 and 35.)

[72] Astrocast, "Astronode development kit," (Accessed 15 Oct. 2022). [Online]. Available: https://www.astrocast.com/ (Cited on pages 24, 35, and 50.)

[73] Hiber Hilo, "Well and pipeline monitoring via satellites," (Accessed 29 May. 2023). [Online]. Available: https://hiber.global/ (Cited on pages 24 and 35.)

[74] K. J. R. Liu, A. K. Sadek, W. Su, and A. Kwasinski, *Cooperative Communications and Networking*. Cambridge University Press, 2008, ch. 4 and 5. (Cited on pages 25, 51, and 57.)

[75] 3rd Generation Partnership Project (3GPP); Technical Specification Group Radio Access Network, "Study on NR network-controlled repeaters (Rel 18)," *TR 38.867V18.0.0*, 2022. (Cited on page 26.)

[76] ——, "Study on Integrated Access and Backhaul (Rel 16)," *TR 38.874V16.0.0*, 2018. (Cited on page 26.)

[77] S. Gadhai and R. Budhiraja, "Evolution of network nodes: From IAB to IRS," *3GPP Highlights Newsletter Issue 06*, 2024, (Accessed 21 Jun. 2024). [Online]. Available: https://www.3gpp.org/newsletter-issue-06-may-2023#flipbook-flip7/21/ (Cited on page 26.)

[78] 3rd Generation Partnership Project (3GPP); Technical Specification Group Services and System Aspects, "Study on satellite access phase 3 (release 19)," *TR 22.865V19.1.0*, 2023. (Cited on page 27.)

[79] 3rd Generation Partnership Project (3GPP); Technical Specification Group Radio Access Network, "Study on New Radio (NR) to support non-terrestrial networks (Rel 15)," *TR 38.811V15.4.0*, 2020. (Cited on page 28.)

[80] 3rd Generation Partnership Project (3GPP); Technical Specification Group Radio Access Network, "Solutions for NR to support non-terrestrial networks (NTN) (Rel 16)," *TR 38.821V16.2.0*, 2023. (Cited on page 28.)

[81] T. Ferrer, S. Céspedes, and A. Becerra, "Review and evaluation of MAC protocols for satellite IoT systems using nanosatellites," *Sensors*, 2019. (Cited on pages xi, 29, 30, and 31.)

[82] K. Zidane *et al.*, "Random access in satellite communications: a background on legacy and advanced schemes. in: Sharma, S. K., Chatzinotas, S. and Arapoglou, P.-D. (eds.) Satellite Communications in the 5G Era," *The Institution of Engineering and Technology*, pp. 425–457, 2018. (Cited on page 29.)

[83] R. De Gaudenzi, O. Del Rio Herrero, G. Gallinaro, S. Cioni, and P.-D. Arapoglou, "Random access schemes for satellite networks, from VSAT to M2M: A survey," *International Journal of Satellite Communications and Networking*, vol. 36, no. 1, pp. 66–107, 2018. (Cited on page 31.)

[84] Sateliot Space, "NB-IoT connectivity from space," (Accessed 02 Oct. 2023). [Online]. Available: https://sateliot.space/en/ (Cited on page 35.)

[85] Indian Space Research Organization (ISRO), "LVM3 M2 / OneWeb India-1 Mission," (Accessed 30 Dec. 2023). [Online]. Available: https://www.isro.gov.in/LVM3M2MissionLandingPage.html (Cited on page 36.)

[86] ——, "LVM3-M3 / OneWeb India-2 Mission," (Accessed 30 Dec. 2023). [Online]. Available: https://www.isro.gov.in/LVM3M3MissionLandingPage.html (Cited on page 36.)

[87] Skyroot Aerospace, "Affordable, On-demand and reliable ride to space," (Accessed 02 Oct. 2023). [Online]. Available: https://skyroot.in/ (Cited on page 36.)

[88] XDLinx Labs, "Commoditizing Deep Space Technology," (Accessed 02 Oct. 2023). [Online]. Available: https://xdlinx.space/platform/ (Cited on page 36.)

[89] I. Lysogor *et al.*, "Study of data transfer in a heterogeneous LoRa-satellite network for the internet of remote things," *MDPI Sensors*, 2019. (Cited on page 36.)

[90] J. A. Fraire, S. Henn, F. Dovis, R. Garello, and G. Taricco, "Sparse satellite constellation design for LoRa-based direct-to-satellite internet of things," in *IEEE Global Communications Conference GLOBECOM*, 2020, pp. 1–6. (Cited on pages 36 and 50.)

[91] T. Wu, D. Qu, and G. Zhang, "Research on lora adaptability in the leo satellites internet of things," in *2019 15th International Wireless Communications & Mobile Computing Conference (IWCMC)*, 2019, pp. 131–135. (Cited on pages 36 and 86.)

[92] Y. Qian, L. Ma, and X. Liang, "The performance of chirp signal used in LEO satellite internet of things," *IEEE Communications Letters*, vol. 23, no. 8, pp. 1319–1322, 2019. (Cited on pages 36 and 87.)

[93] M. Afhamisis and M. R. Palattella, "SALSA: A Scheduling Algorithm for LoRa to LEO Satellites," *IEEE Access*, vol. 10, pp. 11 608–11 615, 2022. (Cited on pages 36, 87, and 88.)

[94] G. Sciddurlo *et al.*, "Looking at NB-IoT over LEO satellite systems: Design and evaluation of a service-oriented solution," *IEEE Internet of Things Journal*, vol. 9, no. 16, pp. 14 952–14 964, 2022. (Cited on page 36.)

[95] O. Liberg *et al.*, "Narrowband internet of things for non-terrestrial networks," *IEEE Communications Standards Magazine*, vol. 4, no. 4, pp. 49–55, 2020. (Cited on page 36.)

[96] O. Kodheli, N. Maturo, S. Chatzinotas, S. Andrenacci, and F. Zimmer, "NB-IoT via LEO satellites: An efficient resource allocation strategy for uplink data transmission," *IEEE Internet of Things Journal*, vol. 9, no. 7, pp. 5094–5107, 2022. (Cited on pages 36 and 86.)

[97] H. Chougrani, S. Kisseleff, W. A. Martins, and S. Chatzinotas, "NB-IoT random access for non-terrestrial networks: Preamble detection and uplink synchronization," *IEEE Internet of Things Journal*, vol. 9, no. 16, pp. 14 913–14 927, 2022. (Cited on pages 36 and 86.)

[98] V. Mannoni, V. Berg, S. Cazalens, and P. Raveneau, "NB-IoT for satellite communications: Physical layer analysis and performance," in *2021 IEEE 32nd Annual International Symposium on Personal, Indoor and Mobile Radio Communications (PIMRC)*, 2021, pp. 1595–1600. (Cited on page 36.)

[99] M. Conti, S. Andrenacci, N. Maturo, S. Chatzinotas, and A. Vanelli-Coralli, "Doppler impact analysis for NB-IoT and satellite systems integration," in *ICC 2020 - 2020 IEEE International Conference on Communications (ICC)*, 2020, pp. 1–7. (Cited on page 36.)

[100] S. Cluzel *et al.*, "3GPP NB-IoT coverage extension using LEO satellites," *IEEE 87th Vehicular Technology Conference (VTC Spring)*, pp. 1–5, 2018. (Cited on page 38.)

[101] T. Ferrer and S. Céspedes, "Review and evaluation of MAC protocols for satellite IoT systems using nanosatellites," *MDPI Sensors*, 2019. (Cited on page 38.)

[102] A. Abdi, W. C. Lau, M. Alouini, and M. Kaveh, "A new simple model for land mobile satellite channels: first- and second-order statistics," *IEEE Transactions on Wireless Communications*, vol. 2, no. 3, pp. 519–528, 2003. (Cited on page 39.)

[103] P. K. Upadhyay and P. K. Sharma, "Max-max user-relay selection scheme in multiuser and multirelay hybrid satellite-terrestrial relay systems," *IEEE Communications Letters*, vol. 20, no. 2, pp. 268–271, 2016. (Cited on page 40.)

[104] V. Singh, P. K. Upadhyay, and M. Lin, "On the performance of NOMA-assisted overlay multiuser cognitive satellite-terrestrial networks," *IEEE Wireless Communications Letters*, pp. 1–1, 2020. (Cited on pages 41 and 47.)

[105] I. Gradshteyn and I. Ryzhik, "Tables of integrals, series and products," *New York: Academic Press*, 2000. (Cited on pages 41, 64, 65, 69, and 70.)

[106] C. Zhang, J. Ge, J. Li, Y. Rui, and M. Guizani, "A unified approach for calculating the outage performance of two-way af relaying over fading channels," *IEEE Transactions on Vehicular Technology*, vol. 64, no. 3, pp. 1218–1229, 2015. (Cited on page 42.)

[107] S. Ikki and M. H. Ahmed, "Performance analysis of cooperative diversity wireless networks over Nakagami-m fading channel," *IEEE Communications Letters*, vol. 11, no. 4, pp. 334–336, 2007. (Cited on page 44.)

[108] Y.-C. Ko, M.-S. Alouini, and M. Simon, "Outage probability of diversity systems over generalized fading channels," *IEEE Transactions Communications*, vol. 48, no. 11, pp. 1783–1787, 2000. (Cited on pages 45 and 66.)

[109] W. Xuewen, L. Min *et al.*, "Performance analysis of multiuser dual-hop satellite relaying systems," *EURASIP Journal on Wireless Communications and Networking*, pp. 1687–1499, 2019. (Cited on pages 46, 73, and 74.)

[110] N. I. Miridakis, D. D. Vergados, and A. Michalas, "Dual-hop communication over a satellite relay and shadowed rician channels," *IEEE Transactions Vehicular Technology*, vol. 64, no. 9, pp. 4031–4040, 2015. (Cited on pages 47 and 75.)

[111] O. Kodheli, N. Maturo, S. Andrenacci, S. Chatzinotas, and F. Zimmer, "Link budget analysis for satellite-based narrowband IoT systems," *International Conference AdHoc Networks Wireless*, 2019. (Cited on page 47.)

[112] Technical Specification (TS) 36.101, "Evolved universal terrestrial radio access; user equipment radio transmission and reception (release 14)," *3rd Generation Partnership Project (3GPP)*, 2017. (Cited on page 47.)

[113] ORBCOMM, "OG2 Satellite IoT modems," (Accessed 15 Oct. 2022). [Online]. Available: https://www.orbcomm.com/en/partners/connectivity/satellite/og2 (Cited on page 50.)

[114] X. Lai, W. Zou, D. Xie, X. Li, and L. Fan, "DF relaying networks with randomly distributed interferers," *IEEE Access*, vol. 5, pp. 18 909–18 917, 2017. (Cited on pages 50 and 52.)

[115] M. R. Bhatnagar and M. K. Arti, "Performance analysis of AF based hybrid satellite-terrestrial cooperative network over generalized fading channels," *IEEE Communications Letters*, vol. 17, no. 10, pp. 1912–1915, 2013. (Cited on pages 51 and 52.)

[116] D. B. da Costa and S. Aissa, "Performance of cooperative diversity networks: Analysis of amplify-and-forward relaying under equal-gain and maximal-ratio combining," in *2009 IEEE International Conference on Communications*, 2009, pp. 1–5. (Cited on pages 51 and 52.)

[117] N. H. Vien and H. H. Nguyen, "Performance analysis of fixed-gain amplify-and-forward relaying with MRC," *IEEE Transactions on Vehicular Technology*, vol. 59, no. 3, pp. 1544–1552, 2010. (Cited on pages 51 and 52.)

[118] S. S. Soliman, "MRC and selection combining in dual-hop AF systems with rician fading," in *International Conference on Computer Engineering & Systems (ICCES)*, 2015, pp. 314–320. (Cited on pages 51 and 52.)

[119] A. Iqbal and K. Ahmed, "A hybrid satellite-terrestrial cooperative network over non identically distributed fading channels," *Journal of Communications*, vol. 6, pp. 581–589, 2011. (Cited on pages 51 and 52.)

[120] H. A. Suraweera, H. K. Garg, and A. Nallanathan, "Performance analysis of two hop amplify-and-forward systems with interference at the relay," *IEEE Communications Letters*, vol. 14, no. 8, pp. 692–694, 2010. (Cited on pages 51 and 52.)

[121] H. A. Suraweera, D. S. Michalopoulos, R. Schober, G. K. Karagiannidis, and A. Nallanathan, "Fixed gain amplify-and-forward relaying with co-channel interference," in *International Conference on Communications (ICC)*, 2011, pp. 1–6. (Cited on pages 51 and 52.)

[122] O. Abbasi, A. Ebrahimi, and N. Mokari, "NOMA inspired cooperative relaying system using an AF relay," *IEEE Wireless Communications Letters*, vol. 8, no. 1, pp. 261–264, 2019. (Cited on page 51.)

[123] A. Argyriou, "Multi-source cooperative communication with opportunistic interference cancelling relays," *IEEE Transactions on Communications*, vol. 63, no. 11, pp. 4086–4096, 2015. (Cited on pages 51 and 52.)

[124] Z. Gao, A. Liu, and X. Liang, "The performance analysis of downlink NOMA in LEO satellite communication system," *IEEE Access*, vol. 8, pp. 93 723–93 732, 2020. (Cited on page 51.)

[125] X. Li, J. Li, Y. Liu, Z. Ding, and A. Nallanathan, "Residual transceiver hardware impairments on cooperative NOMA networks," *IEEE Transactions on Wireless Communications*, vol. 19, no. 1, pp. 680–695, 2020. (Cited on page 51.)

[126] A. Talgat, M. A. Kishk, and M.-S. Alouini, "Stochastic geometry-based analysis of LEO satellite communication systems," *IEEE Communications Letters*, vol. 25, no. 8, pp. 2458–2462, 2021. (Cited on pages 51 and 52.)

[127] F. Baccelli and B. Blaszczyszyn, *Stochastic Geometry and Wireless Networks: Volume I Theory*. Now Foundations and Trends, 2010. (Cited on page 52.)

[128] S. Tegos, P. Diamantoulakis, A. Lioumpas, P. Sarigiannidis, and G. Karagiannidis, "Slotted ALOHA with NOMA for the next generation IoT," *IEEE Transactions on Communications*, vol. 68, no. 10, pp. 6289–6301, 2020. (Cited on page 55.)

[129] Y. Akhmetkaziyev, G. Nauryzbayev, S. Arzykulov, A. Eltawil, K. Rabie, and X. Li, "Performance of NOMA-enabled cognitive satellite-terrestrial networks with non-ideal system limitations," *IEEE Access*, vol. PP, pp. 1–1, 02 2021. (Cited on page 56.)

[130] Y. Akhmetkaziyev, G. Nauryzbayev, S. Arzykulov, A. M. Eltawil, and K. M. Rabie, "Cognitive non-ideal NOMA satellite-terrestrial networks with channel and hardware imperfections," in *2021 IEEE Wireless Communications and Networking Conference (WCNC)*, 2021, pp. 1–6. (Cited on pages 56 and 75.)

[131] Y. Akhmetkaziyev, G. Nauryzbayev, S. Arzykulov, K. Rabie, X. Li, and A. Eltawil, "Underlay hybrid satellite-terrestrial relay networks under realistic hardware and channel conditions," in *2021 IEEE 94th Vehicular Technology Conference (VTC2021-Fall)*, 2021, pp. 1–6. (Cited on page 56.)

[132] Y. Akhmetkaziyev, G. Nauryzbayev, S. Arzykulov, K. Rabie, and A. Eltawil, "Ergodic capacity of cognitive satellite-terrestrial relay networks with practical limitations," in *2021 International Conference on Info. and Communications Technology Convergence (ICTC)*, 2021, pp. 555–560. (Cited on page 56.)

[133] M. Aldababsa, M. Toka, S. Gökceli, G. Karabulut Kurt, and O. Kucur, "A tutorial on non-orthogonal multiple access for 5G and beyond," *Wireless Communications Mobile Computing*, vol. 2018, 06 2018. (Cited on page 58.)

[134] H. Stark and J. W. Woods, *Probability and Random Process with Applications to Signal Processing*. Pearson Education International, 2002, ch. 4. (Cited on page 65.)

[135] N. Pachler, I. del Portillo, E. F. Crawley, and B. G. Cameron, "An updated comparison of four low earth orbit satellite constellation systems to provide global broadband," in *2021 IEEE International Conference on Communications Workshops (ICC Workshops)*, 2021, pp. 1–7. (Cited on page 86.)

[136] G. M. Capez, S. Henn, J. A. Fraire, and R. Garello, "Sparse satellite constellation design for global and regional direct-to-satellite IoT services," *IEEE Transactions on Aerospace and Electronic Systems*, vol. 58, no. 5, pp. 3786–3801, 2022. (Cited on page 86.)

[137] T. Ferrer, S. Céspedes, and A. Becerra, "Review and evaluation of MAC protocols for satellite IoT systems using nanosatellites," *Sensors*, vol. 19, no. 8, 2019. (Cited on page 87.)

[138] L. Zhen, Y. Zhang, K. Yu, N. Kumar, A. Barnawi, and Y. Xie, "Early collision detection for massive random access in satellite-based internet of things," *IEEE Transactions on Vehicular Technology*, vol. 70, no. 5, pp. 5184–5189, 2021. (Cited on pages 87 and 88.)

[139] M. Bacco, P. Cassarà, M. Colucci, and A. Gotta, "Modeling reliable M2M/IoT traffic over random access satellite links in non-saturated conditions," *IEEE Journal on Selected Areas in Communications*, vol. 36, no. 5, pp. 1042–1051, 2018. (Cited on pages 87 and 88.)

[140] J. Lundén and S. Werner, "Real-time smart metering with reduced communication and bounded error," in *2014 IEEE International Conference on Smart Grid Communications (SmartGridComm)*, 2014, pp. 326–331. (Cited on pages 87, 88, and 94.)

[141] A. Shastri, V. Jain, S. Chaudhari, S. S. Chouhan, and S. Werner, "Improving accuracy of the shewhart-based data-reduction in IoT nodes using piggybacking," in *2019 IEEE 5th World Forum on Internet of Things (WF-IoT)*, 2019, pp. 943–948. (Cited on pages 87, 88, and 94.)

[142] A. P. Singh, "Understanding the internet of things: What and how?" *Medium*, Jul 09, 2020. [Online]. Available: https://medium.com/@adarshpalsingh1996/understanding-the-internet-of-things-what-and-how-c54ba34666e (Cited on pages 87, 88, 95, and 103.)

[143] 3rd Generation Partnership Project (3GPP); Technical Specification Group GSM/EDGE radio access network, "GERAN improvements for machine-type communications (MTC) (Rel 12)," *TR 43.868V12.1.0*, 2014. (Cited on page 87.)

[144] N. Jiang, Y. Deng, A. Nallanathan, X. Kang, and T. Q. S. Quek, "Analyzing random access collisions in massive IoT networks," *IEEE Transactions on Wireless Communications*, vol. 17, no. 10, pp. 6853–6870, 2018. (Cited on page 87.)

[145] T. Hoßfeld, F. Metzger, and P. E. Heegaard, "Traffic modeling for aggregated periodic IoT data," in *2018 21st Conference on Innovation in Clouds, Internet and Networks and Workshops (ICIN)*, 2018, pp. 1–8. (Cited on page 87.)

[146] M. López-Benítez, C. Majumdar, and S. N. Merchant, "Aggregated traffic models for real-world data in the internet of things," *IEEE Wireless Communications Letters*, vol. 9, no. 7, pp. 1046–1050, 2020. (Cited on page 87.)

[147] C. Majumdar, M. Löpez-Benítez, and S. N. Merchant, "Experimental evaluation of the poissoness of real sensor data traffic in the internet of things," in *2019 16th IEEE Annual Consumer Communications & Networking Conference (CCNC)*, 2019, pp. 1–7. (Cited on page 87.)

[148] R. Brandborg Sørensen *et al.*, "System level performance analysis for 3GPP NB-IoT NTN solutions with small satellites and sparse LEO constellations," in *IAC 2022 Congress proceedings: 73rd International Astronautical Congress (IAC): Paris, France*. International Astronautical Federation, 2022, pp. 1–13. (Cited on page 89.)

[149] R. Barbau, V. Deslandes, G. Jakllari, J. Tronc, and A.-L. Beylot, "An analytical model for assessing the performance of NB-IoT," in *ICC 2021 - IEEE International Conference on Communications*, 2021, pp. 1–6. (Cited on page 90.)

[150] C. Amatetti, M. Conti, A. Guidotti, and A. Vanelli-Coralli, "NB-IoT random access procedure via NTN: system level performances," in *ICC 2022 - IEEE International Conference on Communications*, 2022, pp. 2381–2386. (Cited on page 90.)

[151] C. R. Reddy *et al.*, "Improving spatio-temporal understanding of particulate matter using low-cost IoT sensors," in *2020 IEEE 31st Annual International Symposium on Personal, Indoor and Mobile Radio Communications*, 2020, pp. 1–7. (Cited on page 92.)

[152] W. A. Shewhart, "Economic quality control of manufactured product," *New York: American Society for Quality Control*, 1980. (Cited on page 94.)

[153] C. M. Bishop, *Pattern Recognition and Machine Learning*. Springer, 2006, ch. 3. (Cited on page 95.)

[154] T. M. Mitchell, *Machine Learning*. McGraw-Hill Science, 1997, ch. 3. (Cited on page 95.)

[155] G. James *et al.*, *An introduction to statistical learning*. Springer, 2013, vol. 112, ch. 8. (Cited on page 95.)

[156] National air quality index, *Central Pollution Control Board India*, (Accessed 11 Apr. 2022). [Online]. Available: https://cpcb.nic.in/National-Air-Quality-Index/ (Cited on pages 96 and 97.)

Errata

Publication 1

Equation (14) was incorrectly written. The correct equation is

$$\gamma^{\text{MRC}} = \sum_{s=1}^{S} \frac{G_s \, H_{us}}{G_s + C_m}.$$

The analysis and the results are updated in Chapter 3.

Publication 2

In Section VI, the measurement unit for the transmit power of the IoT device, P_u, was incorrectly mentioned as dB in some places. In [P2], all the values of P_u are in dBm.